CFIRE

Impact of Increasing Freight Loads on Rail Substructure from Fracking Sand Transportation

CFIRE 07-10
March 2014

National Center for Freight & Infrastructure Research & Education
Department of Civil and Environmental Engineering
College of Engineering
University of Wisconsin–Madison

Authors:
Damien Hesse M.S.
University of Wisconsin–Madison

Principal Investigator:
James M. Tinjum, P.E., Ph.D.
Associate Professor
Engineering Professional Development
University of Wisconsin–Madison

Left Blank Intentionally

1. Report No. CFIRE 07-10	2. Government Accession No	3. Recipient's Catalog No. **CFDA 20.701**	
4. Title and Subtitle Impact of Increasing Freight Loads on Rail Substructure from Fracking Sand Transportation		5. Report Date: March 2014 6. Performing Organization Code	
7. Damien Hesse, James M. Tinjum		8. Performing Organization Report No.	
9. Performing Organization Name and Address National Center for Freight and Infrastructure Research and Education (CFIRE) University of Wisconsin-Madison 1415 Engineering Drive, 2205 EH Madison, WI 53706		10. Work Unit No. (TRAIS) 11. Contract or Grant No. **DTRT06-G-0020**	
12. Sponsoring Organization Name and Address Research and Innovative Technology Administration U.S. Department of Transportation 1200 New Jersey Ave, SE Washington, D.C. 20590		13. Type of Report and Period Covered **Final Report 09/01/2012 – 04/30/2014]** 14. Sponsoring Agency Code	
15. Supplementary Notes **Project completed for USDOT's RITA by CFIRE.**			
16. Abstract In this report the effect of surface infiltration of frac sand and heavy axle loads (HALs) were studied for their impact on the ballast layer. Different combinations of ballast and fracking sand were constructed to observe long term trends of deformational behavior. The results of HAL tests show that for all ballast an increased rate of strain accumulation averaging 0.07%/MGT for every 30 kip car load increase occurs. The results of the surface spillage tests show an average increased rate of strain accumulation averaging 0.05%/MGT, 0.13%/MGT, and 0.31%/MGT for AREMA ballast #24, #4A, and #5 respectively, for a 7% increase in gravimetric water content. Modeling conducted by the WiscRail ® program show and increased maintenance interval of 50-100%. The increased shipment of frac sand for hydrocarbon recovery will affect the rail lines on which it is shipped. Increased monitoring and maintenance will need to be conducted for the lines to operate in an efficient manner.			
17. Key Words Rail, Frac Sand, Ballast, Deformation, Large Scale Cyclic Triaxial Test, Maintenance	18. Distribution Statement **No restrictions. This report is available through the Transportation Research Information Services of the National Transportation Library.**		
19. Security Classification (of this report) **Unclassified**	20. Security Classification (of this page) **Unclassified**	21. No. Of Pages 138	22. Price **-0-**

DISCLAIMER

This research was funded by the National Center for Freight and Infrastructure Research and Education. The contents of this report reflect the views of the authors, who are responsible for the facts and the accuracy of the information presented herein. This document is disseminated under the sponsorship of the Department of Transportation, University Transportation Centers Program, in the interest of information exchange. The U.S. Government assumes no liability for the contents or use thereof. The contents do not necessarily reflect the official views of the National Center for Freight and Infrastructure Research and Education, the University of Wisconsin, the Wisconsin Department of Transportation, or the USDOT's RITA at the time of publication.

EXECUTIVE SUMMARY

The increase in hydraulic fracturing for oil and natural gas in the United States has significantly expanded the frac sand market and impacted freight rail corridors. One of the primary modes of transportation of frac sand is by rail, and the Wisconsin DOT estimates that Wisconsin has the potential to provide up to 50% of frac sand used in hydraulic fracturing operations across the United States. The current and potential growth of the freight rail sector is expected to raise the operation and maintenance costs for the railroads due to the increase in heavy axle loads (HAL), traffic in million gross tons per year (MGT), and fouling from surface spillage. Previous research has correlated fine materials from surface spillage to increased deformation of the ballast layer. The ballast, which provides structural support and rapid drainage during precipitation events, is the most critial layer of the substructure. UW-Madison in partnership CFIRE have conducted investigations into the impact of HAL and frac sand infiltration in the ballast layer.

The impact of HAL on the ballast layer have been studied in some detail; however, it is unknown how infiltration of frac sand into the ballast layer affects the deformational response of the track structure. The purpose of this study was to determine the deformation response due to surface spillage of frac sand into the ballast layer and quantify the effect of moisture in the frac sand-ballast matrix compared to clean ballast. Over a period of several months tests were conducted using a large scale triaxial testing (LSCT) apparatus capable of replicating in-situ stresses, where the LSCT method was validated by a one-half scale model.

Three ballast types and three frac sand samples were examined in this study, of which the following properties were characterized: particle size distribution, mineralogy classification, particle shape, bulk density, void ratio, hydraulic conductivity, and soil water characteristic curves. These properties were used to optimize the LSCT test method. Combinations of frac sand, ballast and water contents were used to examine strain accumulation over a 200,000 cycle loading period. Simulations were also run using the WiscRail® model to evaluate maintenance intervals with the different types of ballast and frac sand.

Results of HAL tests on LSCT specimens show an increased rate of strain accumulation averaging 0.07%/MGT for every 30 kip car load increase (13% load increase). With an increase of 7% gravimetric water content, results of the surface spillage tests show an average increased rate of strain accumulation of 0.05%/MGT, 0.13%/MGT and 0.31%/MGT for AREMA ballast #24,

#4A and #5, respectively. The results of the WiscRail® modeling show similar results to the HAL and ballast type LSCT results. As the load increases, the maintenance cycles increased 50% to 100%. The type of ballast was simulated in the model for AREMA #24, #4A and #5, and the maintenance cycles increased from 50% to 300%, respectively. Both the LSCT and WiscRail® model results show that the two primary factors governing ballast and frac sand deformation behavior are the load amount and the ballast type, while moisture content did not significantly affect the results.

Results from the research indicate surface spillage of frac sand will affect the performance of the ballast layer, which is in turn magnified by HAL. Frac sand spillage from rail cars should be minimized for the ballast layer to resist deformation for an extended period.

Table of Contents

Chapter 1: Introduction 1
1.1. Oil Industry, Hydraulic Fracturing, and Frac Sand 1
1.2. Geology and Frac Sand Mines 3
1.3. Rail System Impacts 7
1.4. Methods 9
1.5. Chapter Outlines 9
Chapter 2: Background 11
2.1. Track Structure and Key Concepts 11
2.1.1. Super-Structure and Sub-Structure 11
2.1.1.1. Rails 13
2.1.1.2. Fastening Systems 13
2.1.1.3. Ties 13
2.1.1.4. Ballast 14
2.1.1.5. Subballast 15
2.1.1.6. Subgrade 15
2.1.2. Ballast Basics 17
2.1.2.1. Stress Distribution using Various Methods 17
2.1.2.2. Resisting Track Shifting and Settlement 26
2.1.2.3. Ballast Fouling and Water Retention 28
2.1.2.4. Track Deflection and FRA Standards 30
2.2. Heavy Axle Loads (HAL) 33
2.2.1. Maintenance and Upgrade Costs 34
2.2.2. Short Line Implications for Wisconsin 36
2.2.3. Class I Implications 38
2.3. Ballast Mechanics 40
2.3.1. Factors Affecting Ballast Behavior 40
2.3.2. Key Properties Affecting Resilient Modulus 46
2.3.3. Key Factors Affecting Permanent Strain 50
2.4. Sand Mechanics 52
2.4.1. Sand under Cyclic Load 52
2.4.2. Frac Sand Effects on Ballast Behavior under Cyclic Loading 52
Chapter 3: Materials 54
3.1. Frac Sand 54
3.1.1. Grain-Size Distribution and Phase Relationships 54

3.1.2. Shape Characteristics 57
3.1.3. Hydraulic Conductivity 59
3.1.4. Soil-Water Characteristic Curves 62
3.2. Ballast 65
3.2.1. Particle-Size Distribution 65
3.2.2. AREMA Classification 67
3.2.3. Mineralogy 67
3.2.4. Particle Shape 67
3.2.5. Density and Void Ratio 70
Chapter 4: Large-Scale Cyclic Triaxial (LSCT) 72
Testing Methods and Procedures 73
4.1. LSCT – Overview 73
4.2. Testing Matrix 75
4.2.1. Water Content Considerations 75
4.2.2. Fouling Content Considerations 75
4.2.3. Heavy Axle Considerations 78
4.2.4. Complete Desired Matrix 78
4.3. Load, Pulse Shape, and Frequency 81
4.4. Compaction Method 81
4.5. Membrane Preparation 85
4.6. Sample Preparation 85
4.7. Measurement Equipment 88
4.8. Repeatability Tests 90
Chapter 5: Results 93
5.1. LSCT Results 93
5.1.1. Water Content 93
5.1.2. Ballast Type and Gradation 97
5.1.3. Sand Gradation 100
5.1.4. Fouling Index (FI) 105
5.1.5. HAL tests (σ_d = 250 kPa, 300 kPa, 350 kPa, 400 kPa, & 450 kPa) 109
5.1.6. Fresh s. Recycled Ballast Tests; FI = 0; w = 0; (σ_d = 300 kPa & 450 kPa) 111
5.2. WiscRail™ Modeling and Maintenance Cycles 114
5.2.1. WiscRail™ Model Background and Development 114
5.2.2. WiscRail™ Results 124

5.3. Maintenance Cost Estimates 134
Chapter 6: Summary and Conclusions 135
References 137

LIST OF FIGURES

Figure 1.1 Oil and Gas Production in the US 2
Figure 1.2 Wisconsin Geologic Formations. 4
Figure 1.3 Operational and Proposed Sand Mines in Wisconsin. 6
Figure 1.4 Frac Sand Spillage Near Ottowa, IL. 8
Figure 2.1 Ballast Super-Structure and Sub-Structure. 12
Figure 2.2 Side profile of typical rail stress distribution 17
Figure 2.3 Full Scale Track Model and Large Scale Cyclic Triaxial Model comparison used in Ebrahimi's Thesis 19
Figure 2.4 Stress distribution using Talbot calculations and effective tie area assumptions 22
Figure 2.5 Linear model of wheel load versus max stress from ABAQUS finite element results 25
Figure 2.6 Surface Deviation of Track. 27
Figure 2.7 Diagram of Fouling Content Levels. 29
Figure 2.8 Fouling contribution breakdown (a) (Indraratna et al. 2011) and (b) (Selig and Waters 1994) 29
Figure 2.9 Wisconsin's maximum allowable weight for freight rail cars 33
Figure 2.10 United States Freight Rail Network 35
Figure 2.11 Typical settlement characteristics of ballast, subballast, and subgrade 41
Figure 2.12 Ballast density variations 44
Figure 2.13 Plots of settlement vs. number of loadings in Cartesian (a) and semilogrithmic (b) 47
Figure 2.14 Effect of frequency on ballast deformation and ballast breakage 48
Figure 2.15 Diagram of the total, permanent, and resilient strain as a function of stress 49
Figure 2.16 Diagram showing first cycle plastic strain variation as a function of porosity 51

Figure 3.1 Grain Size Distribution of Frac Sand Samples 55
Figure 3.2 Shape Parameters for Frac Sand Samples..... 58
Figure 3.3 Hydraulic Conductivity of Frac Sand Samples 60
Figure 3.4 Typical ranges of hydraulic conductivity (Casagrande and Fadum 1940) 61
Figure 3.5 Haning Column Setup 63
Figure 3.6 Soil Water Characteristic Curves for Frac Sand Samples 64
Figure 3.7 Particle-Size Distribution for Ballast Samples. 66
Figure 3.8 AREMA #5 thin section analysis images. 68
Figure 3.9 AREMA #24 thin section analysis images. 68
Figure 3.10 Ballast Shape Characteristics 69
Figure 4.1 Large-Scale Cyclic Triaxial (LSCT) Setup Diagram. 74
Figure 4.2 Calculation and diagram of the loading frequency. Train car specifications (American Railcar Leasing) 82
Figure 4.3 Maximum allowable train speeds on Wisconsin Railways 83
Figure 4.4 Diagram of the Band Spacers and Arangement of Cable Transducers. 87
Figure 4.5 Accumulation of plastic strain and rate of plastic strain for repeated tests #42 & #34, under 2 x 10^5 loading cycles. 91
Figure 4.6 Accumulation of plastic strain and rate of plastic strain for repeated tests #43 & #22, under 2 x 10^5 loading cycles. 92
Figure 4.7 Accumulation of plastic strain and rate of plastic strain for repeated tests #37 & #38, under 2 x 10^5 loading cycles. 92
Figure 5.1 Cumulative plastic strain, comparison of water content for the same ballast and frac sand at w = 4, 14 (left to right). 96
Figure 5.2 Rate of plastic strain, comparison of water content for the same ballast and frac sand at w = 4, 14 (left to right). 96
Figure 5.3 Cumulative plastic strain, comparison of ballast type and gradation AREMA #24 to AREMA #5 at w = 4 (top to bottom). 98
Figure 5.4 Rate of plastic strain, comparison of ballast type and gradation AREMA #24 to AREMA #5 at w = 4 (top to bottom). 99
Figure 5.5 95% confidence interval for t-statistics testing. 102

Figure 5.6 Cumulative plastic strain, comparison of sand gradation from 20/40 to 70/140 (top to bottom) in AREMA #24 and AREMA #5 ballast (left to right). 103
Figure 5.7 Rate of plastic strain, comparison of sand gradation from 20/40 to 70/140 (top to bottom) in AREMA #24 and AREMA #5 ballast (left to right). 104
Figure 5.8 Cumulative plastic strain, comparison of Fouling Index, FI = 15, 30 (left to right) for AREMA #24 to AREMA #5 (top to bottom). 107
Figure 5.9 Rate of plastic strain, comparison of Fouling Index, FI = 15, 30 (left to right) for AREMA #24 to AREMA #5 (top to bottom). 108
Figure 5.10 Comparison of HAL for AREMA #24 ballast, FI = 0, 30, and w = 0, 4. 110
Figure 5.11 Comparison of fresh versus recycled for AREMA #24 ballast, FI = 0, w = 0, and σ_d = 300 kPa, 450 kPa 113
Figure 5.12 WiscRail™ program interface with sample data 115
Figure 5.13 Maintenance planning model WiscRail™ using fouling, moisture, loading conditions, and seasonal variations (Ebrahimi 2011) 116
Figure 5.14 WiscRail model parameters ‘a’ and ‘b’ for sample data. These parameters will vary for changing ballast type, fouling type, fouling content, and moisture content. 118
Figure 5.15 WiscRail™ parameters derived from ‘a’ and ‘b’ LSCT deformation parameters as a function of fouling index and water content. 120
Figure 5.16 Wisconsin Rail Densities in MGT, 2007 study from the FRA (Wisconsin DOT 2010) 121
Figure 5.17 WiscRail™ model results for HAL with 225, 280, and 310 kip graphs represented. 127
Figure 5.18 WiscRail™ model results for AREMA #24 with 20/40 frac sand varying the water conditions. 130
Figure 5.19 WiscRail™ model results for AREMA #4A with 20/40 frac sand varying the water conditions. 131
Figure 5.20 WiscRail™ model results for AREMA #4A with 70/140 frac sand varying the water conditions. 132
Figure 5.21 WiscRail™ model results for AREMA #5 with 20/40 frac sand varying the water conditions. 133

LIST OF TABLES

Table 2.1 Parameters used for the ABAQUS maximum ballast stress model. 24
Table 2.2 Comparison of the stress distribution methods..... 25
Table 2.3 Shows the allowances for surface of rail for each class (1-5) and for both cross level and tangent track..... 32
Table 2.4 Cost to upgrade short line and regional railroads to handle 286,000 lb cars (Zarembski 2001). 37
Table 2.5 HAL costs and benefits broken down by track components and gross weight loadings..... 39
Table 3.1 Summary of Frac Sand Properties 55
Table 3.2 van Genuchten (1980) Soil Water Characteristic Curve Fitting Parameters for Frac Sand. 64
Table 3.3 AREMA Ballast Specifications..... 66
Table 3.4 Summary of Ballast Properties..... 71
Table 4.1 Fouling Index Ranges 77
Table 4.2 Testing matrix for clean ballast. 80
Table 4.3 Testing matrix for frac sand fouled (FI = 15) ballast. 80
Table 4.4 Testing matrix for frac sand fouled (FI = 30) ballast. 80
Table 4.5 Testing Matrix for frac sand fouled (FI = 30) ballast at HAL. 80
Table 4.6 LSCT test method and preparations parameters from previous studies. 83
Table 4.7 LSCT test parameters from previous studies. 84
Table 4.8 Average of initial density and range of specimen height for all tests. 84
Table 5.1 Statistics for frac sand gradation variation. 102
Table 5.2 Subgrade Deformation Model Parameters (Li and Selig 1996). 123
Table 5.3 WiscRail™ model parameters used for this study to determine the effect of axel load, moisture, and fouling content on the maintenance cycles of track ballast. 125

Chapter 1: Introduction

1.1. Oil Industry, Hydraulic Fracturing, and Frac Sand

Fossil fuels are vital resources in the American and world economies and are connected to many other industries (Figure 1.1). The main connection between the oil industry and the frac sand industry has to do with the hydraulic fracturing process. The feasibility and development of directional drilling, specifically horizontal drilling methods, has allowed hydraulic fracturing techniques to become cost effective. The horizontal drilling technique has only been used in great quantity for the past five to ten years. A typical hydraulic fracturing treatment costs around $2 million for a 3000-meter horizontal well in the Bakken oil basin in Western North Dakota (EERC 2010) . A well of this size is estimated to require 13 million liters of water and 2 million kilograms of sand to produce in the Bakken basin in 2010 (EERC 2010). This example quantity of sand needed per well has been driving an explosive market in the Midwest frac sand industry since the middle to late 2000's.

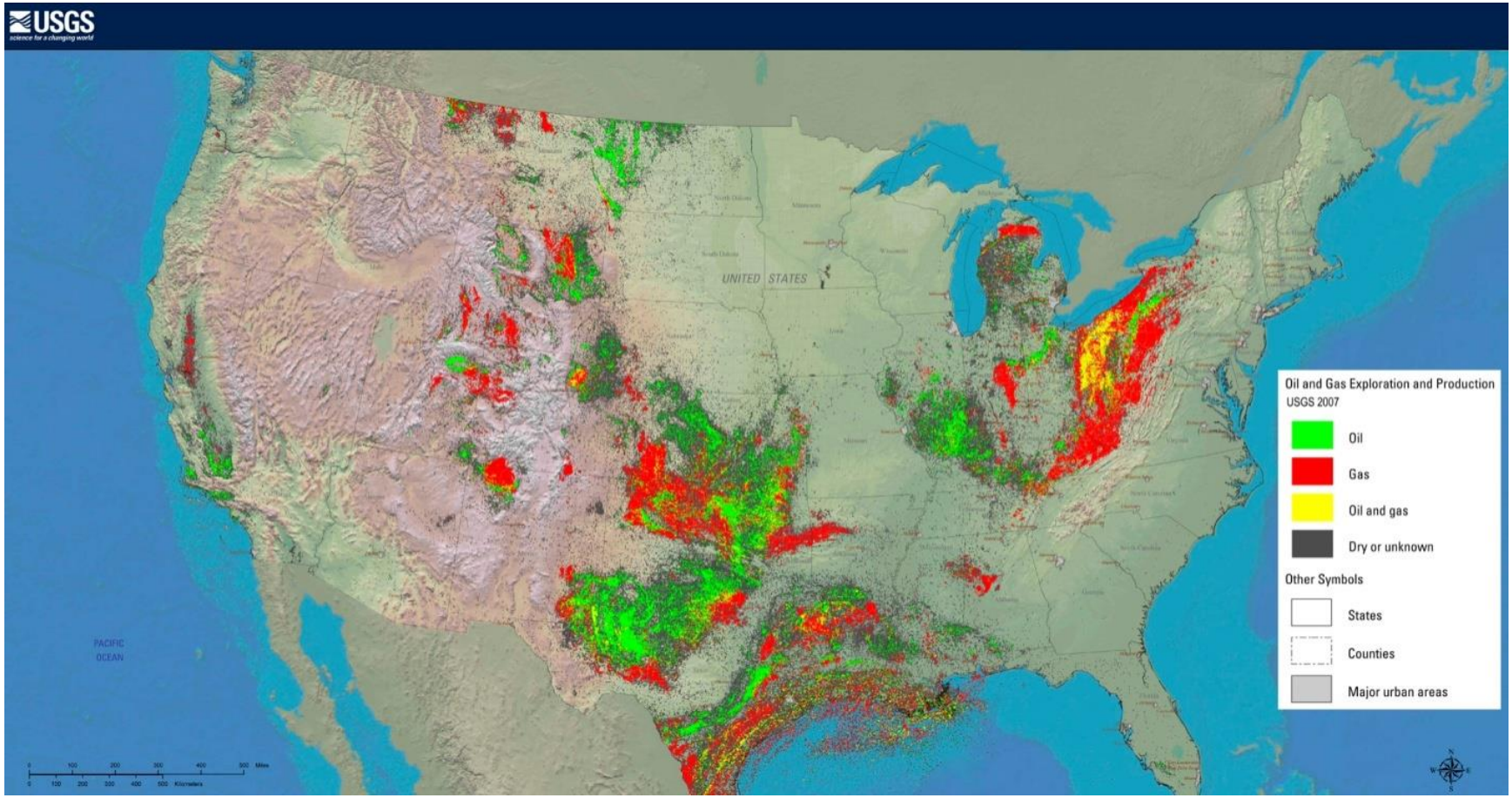

Figure 1.1 Oil and Gas Production in the US (USGS, 2007).

Frac sand, commonly referred to as silica sand or proppant, is almost entirely silicon dioxide (SiO_2). Ideal frac sand is well rounded, poorly graded, and, due to being nearly 100% quartz, is a very strong material. Compressive strength between 41,000 kPa and 96,700 kPa is typical for commercial grade frac sand (Wisconsin DNR 2012).

1.2. Geology and Frac Sand Mines

Frac sand facilities in the Midwest are concentrated in western Wisconsin, northwestern Illinois, southeastern Minnesota, and northeastern Iowa. This area's mining and processing industry produces a majority of frac sand for the U.S. Out of the four states, this study will focus on Wisconsin and Illinois as this is where the frac sand and ballast samples were obtained. The Wisconsin DOT estimates that Wisconsin alone has the potential to provide as much as 50 percent of the entire frac sand market (Pickard 2013).

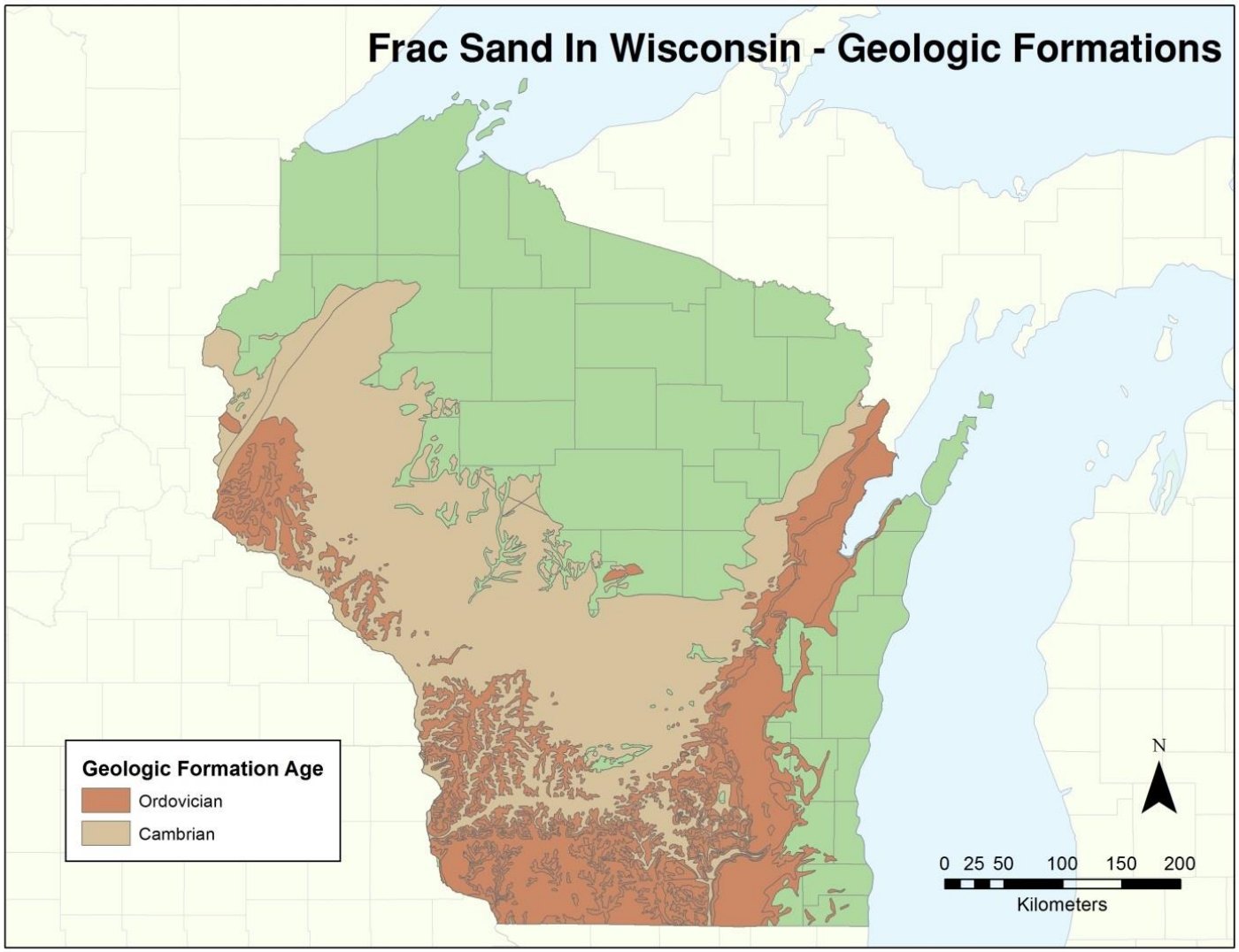

Figure 1.2 Wisconsin Geologic Formations.

The surface geology of western Wisconsin has large areas where sand formations are exposed or near to the surface. The primary geologic formations that meet the required specifications for frac sand production are the Jordan, Wonewoc, and Mt. Simon of the Cambrian-age, and the St. Peter of the Ordovician-age (Wisconsin DNR 2012) (Figure 1.2). Before there was a demand for frac sand, Wisconsin had a 100-year history of small-scale sand mining that supplied the foundries, glass production and abrasive manufacturing industries (Wisconsin DNR 2012). As of 2013, because of the demand for frac sand, The Wisconsin DNR estimates that there are approximately 60 sand mining, processing plants, and rail load facilities currently operating and at least 30 additional establishments proposed as of January 2012 (Wisconsin DNR 2012) (Figure 1.3). This recent boom in large-scale operating mines and proposals has greatly impacted some communities in western Wisconsin. Many of these communities did not have sand mines previously, or did but simply do not have the resources to process the requests for new mines and the oversight and regulation that go along with it. The Wisconsin counties that have operational or proposed locations include: Barron, Buffalo, Chippewa, Dunn, Green Lake, Jackson, Monroe, Pepin, Pierce, St. Croix, and Trempealeau (Wisconsin DNR 2011). The frac sand that originates in Wisconsin is shipped to major oil operations across the United States (Figure 1.1).

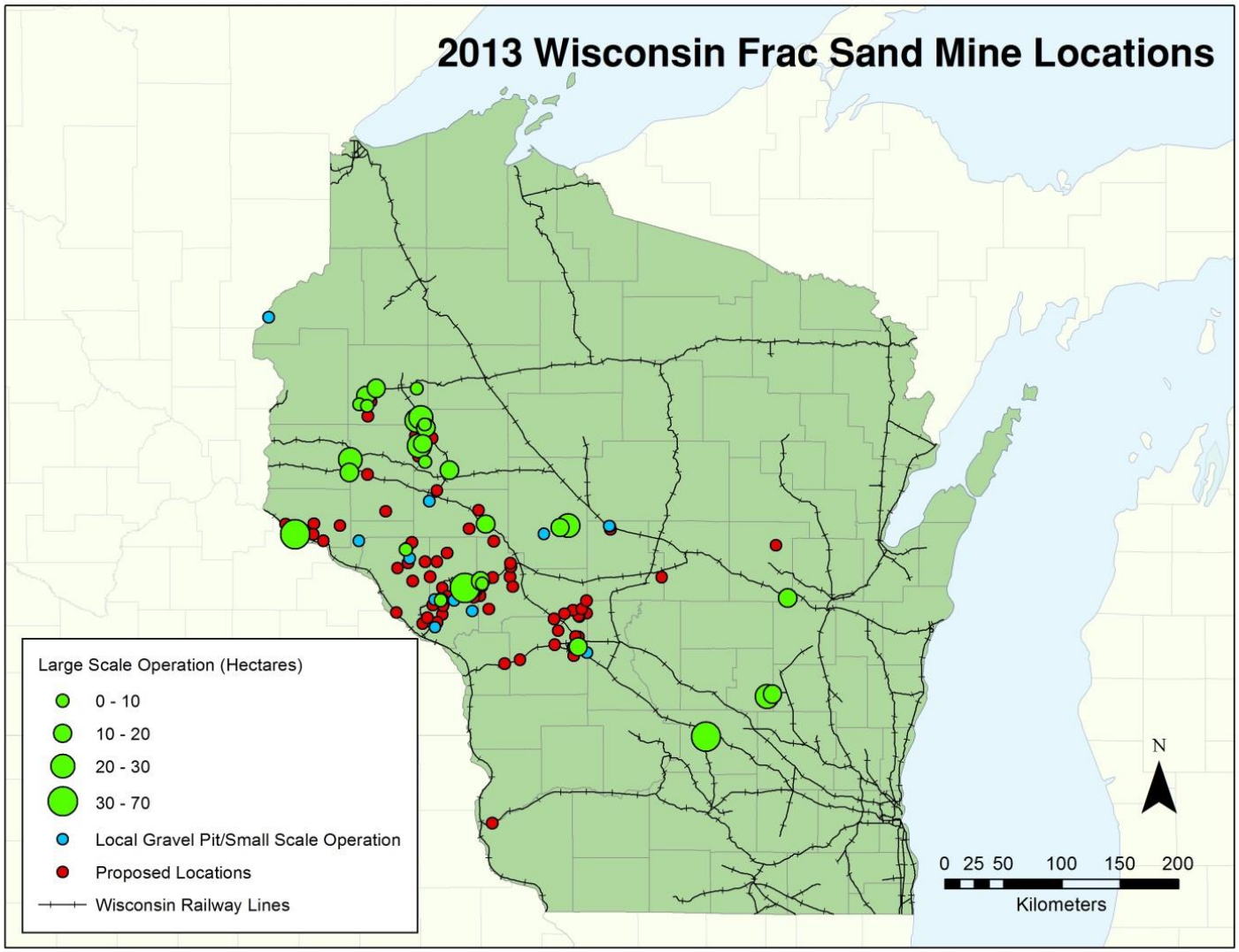

Figure 1.3 Operational and Proposed Sand Mines in Wisconsin.

1.3. Rail System Impacts

The increase in frac sand transportation has the potential to affect the rail systems that support this growing industry in two primary ways. Fracking sand is denser than most other commodities being shipped by rail. This characteristic makes it much easier to meet or exceed rail corridor load capacities. The occurrence of high-quantity, full-capacity trains, which have become more frequent with the frac sand industry growth, introduces potential to increase the rate of degradation to the rail and substructure. The methods for fouling accumulation and the mechanisms that control ballast deformation will be covered further in Section 2.

The transportation of fracking sand also has potential to be separated from the cars in small amounts along the route either from wind out of the top of open gondola cars or from vibration out of the drop bottoms in hopper cars (Figure 1.4). Over time, this buildup of fracking sand in the ballast structure can potentially result in increased deformation, plastic strain, and fouling content. This increased deformation is mainly due to the effects of moisture retention and increased breakage of ballast particle because of the fouling material interaction. The goal of this study is to characterize these effects on the rail ballast and to predict maintenance costs. These results will aid in predicting and planning maintenance issues and costs related to transporting frac sand over Wisconsin railways. Potential life cycle impacts have not been conducted for this sector of the rail transportation industry. A life cycle assessment can be completed by using the results of this research to assess impacts on maintenance cycles and costs.

Figure 1.4 Frac Sand Spillage Near Ottowa, IL.

1.4. Methods

The methods for characterizing frac sand include ASTM International standards for density, void ratio, hydraulic conductivity, particle size distribution, and soil water characteristic curves. The methods that were used to characterize the ballast included thin section analysis, particle shape analysis, particle size analysis, American Railway Engineering and Maintenance-of-Way Association (AREMA) classification, density, and void ratio. The main testing conducted will show the amount of plastic deformation of the ballast material that results adding moisture and frac sand in specific amounts. This deformation will be determined using Large-Scale Cyclic Triaxial (LSCT) testing methods developed in previous thesis work by (Ebrahimi 2011).

1.5. Chapter Outlines

Chapter 2 covers the basic information about the track structure, ballast and sand mechanics, and other considerations for determining an appropriate testing matrix. This section details the ideas and equations from previous research necessary for understanding and conducting this current research. Chapter 3 describes the materials used for the LSCT tests. In addition the preliminary properties and associated tests are also provided. These preliminary tests not only helped to categorize the materials that we received but also to direct the selection of the testing matrices that were described in Chapter 2. Chapter 4 describes the methods and procedures used for developing and running the LSCT tests. The calculation of the load, pulse shape, and frequency are detailed. The membrane preparation, compaction method, and data acquisition equipment specifications are also detailed. Chapter 5 covers the results and discussions of the LSCT tests, which include the standard surface spillage tests at

varying fouling and water contents, the heavy axle loading tests, the fresh vs. recycled ballast comparisons, and the repeatability tests. This section also presents the methods and results of the WiscRail™ model and the maintenance cost estimations.

Chapter 2: Background

2.1. Track Structure and Key Concepts

2.1.1. Super-Structure and Sub-Structure

Track structure has remained nearly the same over the course of American railroad history. Slight modifications and additions have been incorporated, but the main components remain and their function for stress distribution and stability remains. The track structure (Figure 2.1) is broken down into two main components, the super-structure and sub-structure. The super-structure consists of the rails, fastening systems, and ties. The sub-structure consists of the ballast, subballast, and subgrade. These components are described in detailed in the following sections.

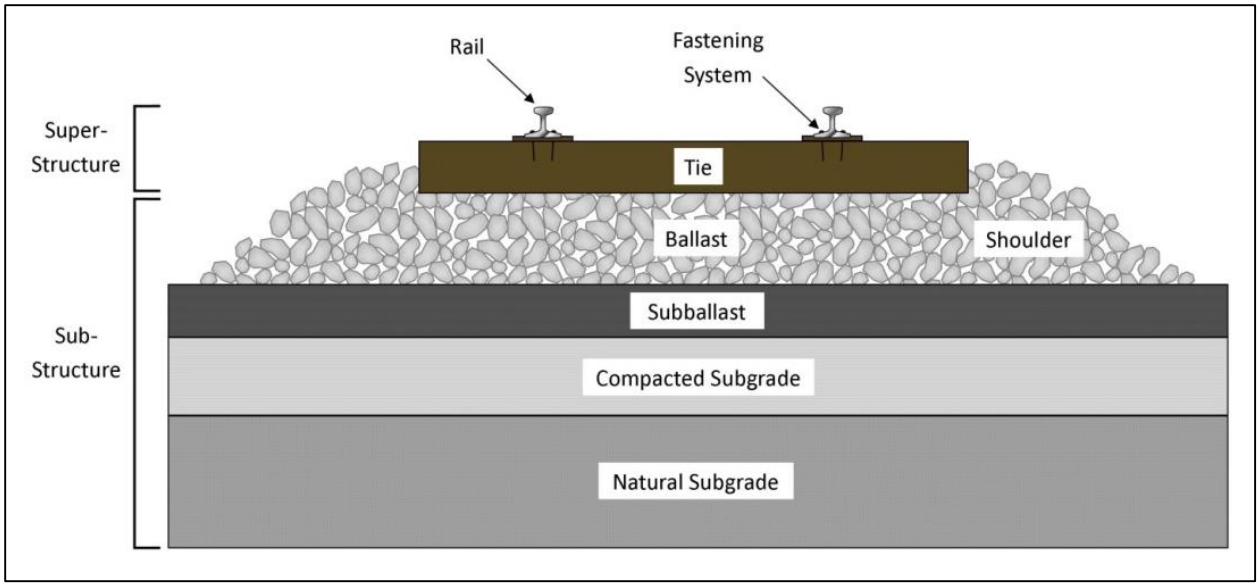

Figure 2.1 Ballast Super-Structure and Sub-Structure.

2.1.1.1. Rails

The rail consists of the web-shaped steel component that is in direct contact with the wheel. The rail is the first component that distributes the load of the rail car. There are many types and weights of rail, but the main job of rail is to adequately support the load of the cars. There are internal and external factors that affect the life of the rail. Some of the internal factors include proper design of the rail cross section, metallurgy, manufacturing process, hardening and curing procedures, and defects. Some of the external factors that affect the life of the rail include subgrade and ballast conditions, tie and fastener conditions, geometry maintenance, super-elevation of curves, train operating speeds, as well as types and magnitudes of rail car loadings. Though this study does not take the rail mechanics into account, rail performance is directly tied to the performance of other track structure components.

2.1.1.2. Fastening Systems

The fastening system consists of the mechanism that holds the rail to the ties. This often consists of tie plates that sit under the rail which increase the bearing area of the rail on the tie and rail spikes to fasten the rail to the tie plate and tie. For some passenger rail lines there are more complex systems of tie plates, rubber padding, and securing devices. The variation in design and function vary greatly, however, this study does not take into account any of the variability as much of the freight system uses the tie plate and rail spike system. Again, much like the rail, for the track structure to work as effectively as possible, all components must be designed to work together.

2.1.1.3. Ties

Ties are the components of the track structure that are placed at the top of the ballast layer, perpendicular to the direction of rail. The function of the tie is to take the load from the bottom of the tie plate (or other fastening system) and distribute that load through the tie to the ballast structure (Indraratna et al. 2011). For this system to work effectively, each component must adequately handle the loads and stresses. Ties come in a variety of types and sizes, though the most common is the wood tie with dimensions of 2.59 m x 0.229 m x 0.178 m (9' x 9" x 7") (L x W x H) (Selig and Waters 1994). Other types of ties include reinforced concrete, steel, recycled plastic, tropical hardwood, and composite ties (Indraratna et al. 2011) . The target properties of an effective tie are long life, load-bearing capacity, and minimal defects. For much of the freight industry and in most US climate regions, standard wood ties meet these requirements and are often most cost effective (Webb et al. 2012).

2.1.1.4. Ballast

Ballast is the component that makes up the main stress distribution component of the track substructure. The ballast layer is the main component of study in this work. The ballast provides a stiff structure to distribute the load from the ties to the subballast and, with its large voids, prevents water retention in the track structure. Ballast of sufficient quality should result in high strength and stiffness, work to drain water from the tie area, and distribute the concentrated load from the ties to the subballast and subgrade. Fouling accumulation in the ballast is one of the main concerns for ballast performance and stability. The accumulation of sand-sized fouling in the ballast reduces the drainage capacity and, when voids are full, tamping and traffic vibration can cause the ballast structure to separate leading to increased deformation (Selig and

Waters 1994). According to Selig and Waters (1994), there are five main categories of ballast fouling: (1) ballast breakdown, (2) infiltration from ballast surface, (3) tie wear, (4) infiltration from underlying granular layers, and (5) subgrade infiltration. Ballast fouling will be detailed further in Section 2.1.2.3.

2.1.1.5. Subballast

Subballast is located underneath the ballast layer and above any subgrade or compacted subgrade layer. The subballast usually consists of a smaller gradation than the ballast. This is to provide a gradation change from the subgrade to the ballast, which seeks to prevent subgrade intrusion (clay pumping), or ballast suspension in the subgrade. There are instances where the subballast has been enhanced with geo-grids and geo-fibers; both to provide strength and stiffness to this layer and prevent movement of soil and ballast as the structure undergoes successive loadings. Although not the focus of this work, the subballast provides a key role in the function of the track structure in minimizing fouling accumulation and further distribution of loads to the subgrade.

2.1.1.6. Subgrade

Subgrade refers to the natural soil of the area and when constructing sections of track the quality of the subgrade must be fully understood and accounted for in to the design calculations. In an area of sufficient subgrade little to no soil stabilization work may need to be done, but areas of soft soil will need to be considered in the design process and managed appropriately. There are a variety of methods that can be used to strengthen soft soil, depending greatly on the soil properties in that area. As was true for ballast and subballast, water drainage is a key factor when designing a track section.

Drainage ditches, culverts, and vegetation management strategies need to be assessed as any unwanted moisture retention can lead to track instability and major damage to track and train components.

2.1.2. Ballast Basics

2.1.2.1. Stress Distribution using Various Methods

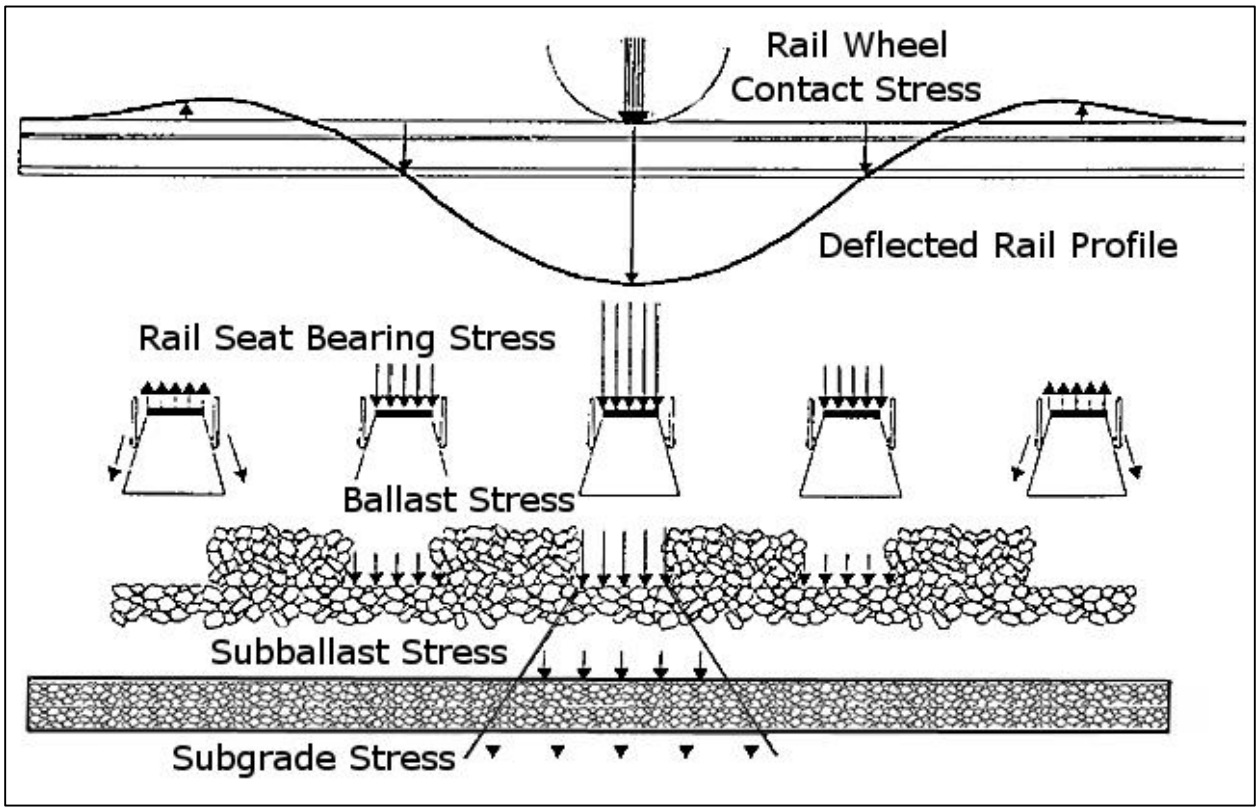

Figure 2.2 Side profile of typical rail stress distribution(Selig and Waters 1994).

Stress distribution in the track structure from the rail to the subgrade is shown in profile view (Figure 2.1) and from the tie to subballast in cross section (Figure 2.2). Three methods were used in this study to confirm that the 300 kPa deviator stress and 90 kPa confining stress (Figure 2.3) used by Ebrahimi (2011) were reasonable and could be replicated for this study. Ebrahimi's (2011) research involved the comparison of large-scale cyclic triaxial results for ballast material against results from a full-scale track model of the same material. The Love equation, Talbot stress reduction, and finite element modeling calculations were utilized for verification of his models and are explained and compared.

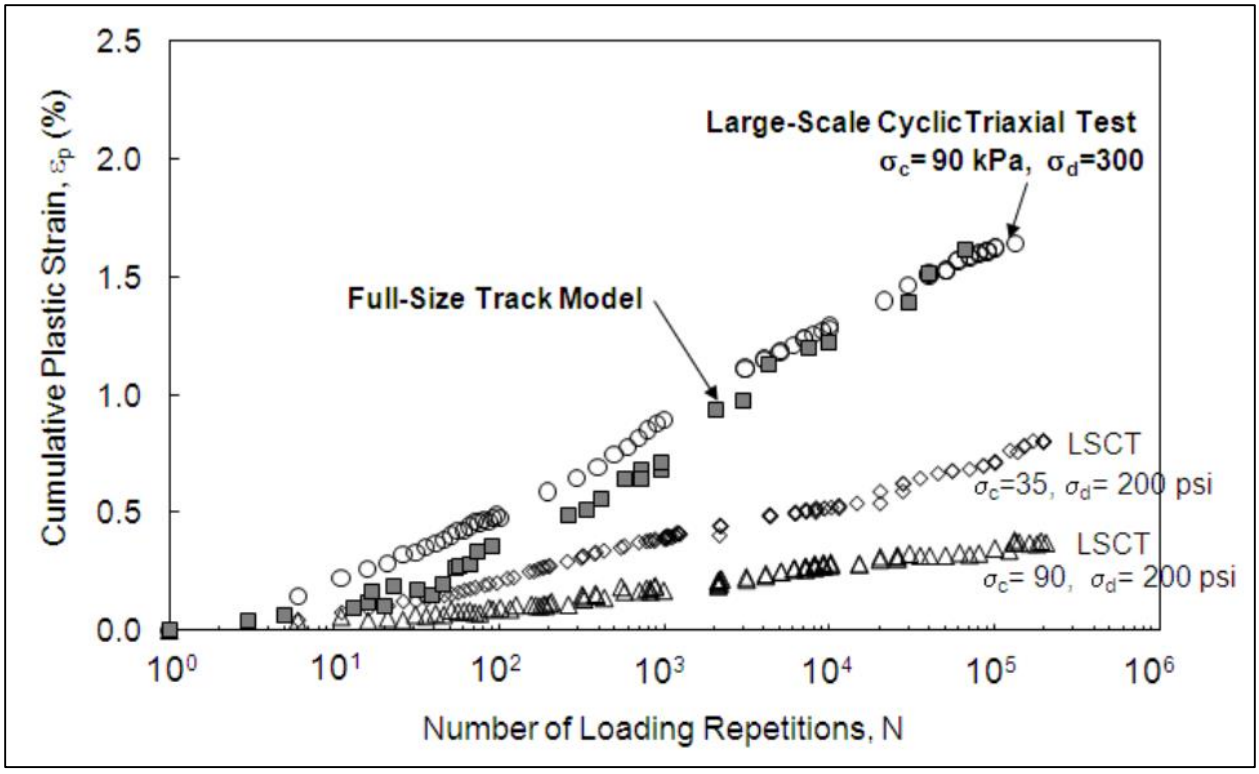

Figure 2.3 Full-Scale Track Model and Large-Scale Cyclic Triaxial Model comparison used by Ebrahimi (2011).

2.1.2.1.1. Love Equation

The Love equation is a simple model for predicting sleeper ballast contact stress (Indraratna et al. 2011). The equation is detailed below and the comparison of the various models is shown in Section 2.1.2.1.4. The main limitations of this method are that the dynamic rail load is not taken into account and the factor of safety chosen greatly influences the output (Table 2.2).

$$\sigma_{max} = \frac{2P_{stat}}{A_{sb}}(FS) \qquad \text{Eq. 2-1.}$$

σ_{max} = Sleeper-ballast contact stress
P_{stat} = Static rail seat load (Assumed to be 50% of the static wheel load (Indraratna et al.2011)
A_{sb} = Effective area of tie under rail seat (assumed to be 1/3 the area under the tie)
FS = Factor of safety

2.1.2.1.2. Gross Carload and Talbot Reductions

The Talbot Reductions method involves taking the gross weight of the car in lb or kN and calculating the static wheel load at the point of contact on the rail in kN. The stress (Figure 2.4) under the tie at the tie-ballast interface is calculated by the following equation:

$$\sigma_{max} = \frac{\text{Wheel Load (kN)}}{\text{Effective Tie Surface Area } (m^2)} * Talbot\ Reduction \qquad \text{Eq. 2-2.}$$

Talbot (1980) assumes that 25% of the wheel load is transferred from the wheel load to the tie due to the reductions of stress through the rail and tie plate. The effective tie surface area was obtained from Ebrahimi (2011) and used to calculate the stress on the ballast from the static wheel load. The limitations of this method are that the dynamic wheel load is not taken into account and that the effective tie area used by Ebrahimi

(2011) is different than other effective tie surface area estimations (Indraratna et al. 2011; Selig and Waters 1994). Effective tie surface area estimations form those other sources reduce the stress values by up to 40%, which drops the resulting stresses below the range of values shown in Table 2.2.

Rail Car Gross Weight/Force		
lb	kg	kN
194,227	88,100	864
223,000	101,151	992
252,000	114,305	1,121
280,000	127,006	1,246
309,000	140,160	1,375

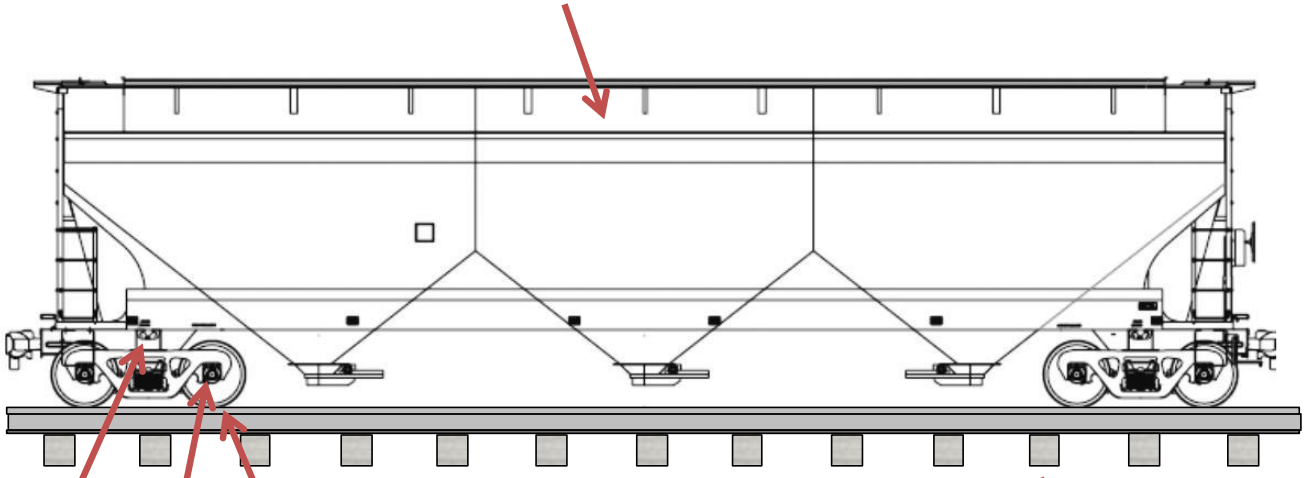

Bogie Force (kN)	Axel Force (kN)	Wheel Force (kN)
432	216	108
496	248	124
560	280	140
623	311	156
687	344	172

Effective Tie Surface Area (m^2)	0.080

0.15 m x 0.53 m, (Ebrahimi, 2011)

25% reduction from wheel to tie due to superstructure, Talbot (1980)

	LSCT Stress Parameters	
Stress Under Tie (kPa)	Deviator Stress (kPa)	Confining Stress (kPa)
340	250	90
390	300	90
441	350	91
490	400	90
540	450	90

Figure 2.4 Stress distribution using Talbot calculations and effective tie area assumptions (Talbot 1980; Ebrahimi 2011).

2.1.2.1.3. Finite Element Modeling

Alsabhan (2013) studied the stress and deformation behavior of rail track using finite element modeling. The ABAQUS finite element modeling software was used to assess the maximum tie sleeper contact pressure as a function of wheel load (Figure 2.5) and was based on properties from a study conducted by Stewart and Selig (1982). The specific properties used in the program are shown in Table 2.1. Though this method accounts for a variety of track properties (e.g. modulus, moment of inertia, and thicknesses of the ballast layers and track components), The Alsabhan (2013) model is a static load model and does not account for dynamic loading effects.

Table 2.1 Parameters used for the ABAQUS maximum ballast stress model.

Reference Study	Stewart and Selig (1982) Representative-Numerical	This Study Base Model-Finite Element
Program	GEOTRACK	ABAQUS
Rail E (MPa)	207,000	207,000
Rail I_z (m^4)	$0.395x10^{-4}$	$0.395x10^{-4}$
Ties E (MPa)	10,300 (wood)	10,300 (wood)
Ties I_z (m^4)	$1.07x10^{-4}$	$1.01x10^{-4}$
Ties s (m)	0.495	0.495
Ballast E (MPa)	310	310
Ballast v	0.3	0.3
Ballast t (m)	0.38	0.38
Subballast E (MPa)	N/A	100
Subballast v	0.4	0.4
Subballast t (m)	0.15	0.15
Subgrade E (MPa)	55	55
Subgrade v	0.4	0.4
Subgrade t (m)	>0.91	6
Wheel Load (kN/# axels)	89-175/ 4-axels	89-175/ 4-axels

Notes: v = Poisson's ratio, E = Young's Modulus, Iz = momentof inertia, s = spacing, t = thickness, w = width, l = length

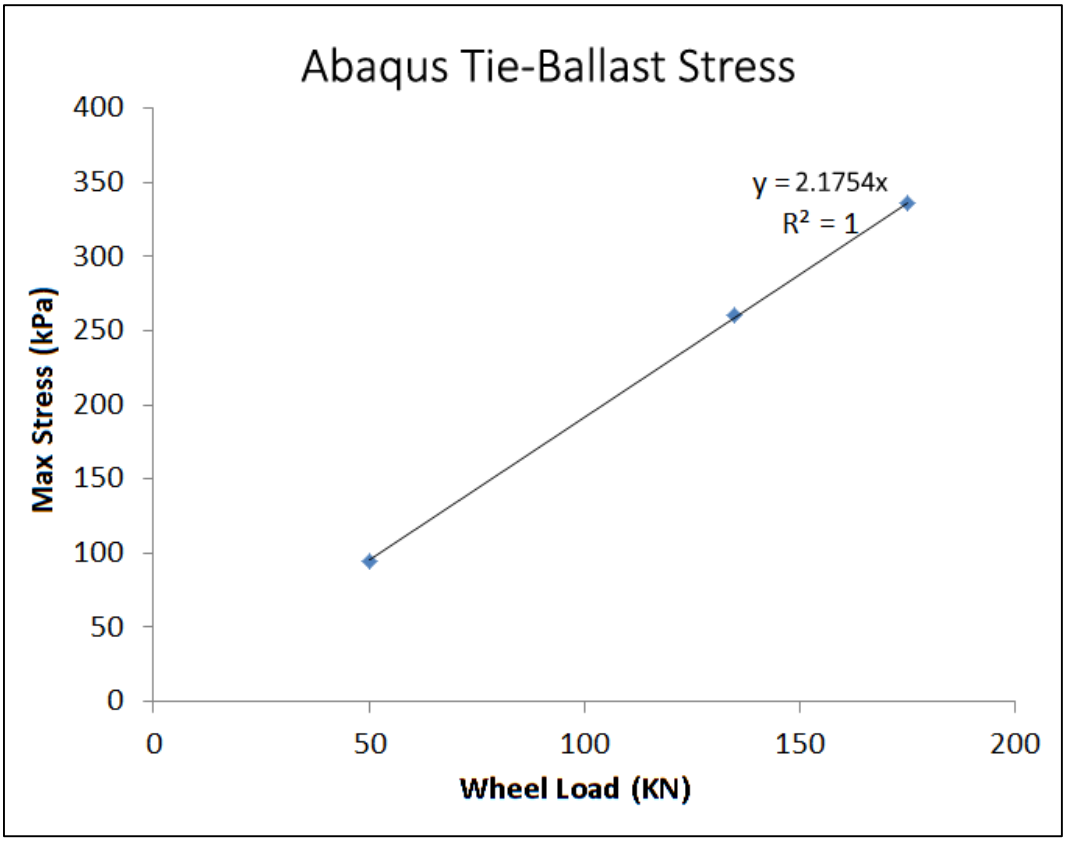

Figure 2.5 Linear model of wheel load versus max stress from ABAQUS finite element results.

Table 2.2 Comparison of the stress distribution methods.

Gross Car Weight (kip)	Wheel Load (kN)	Love (FS=1.1) (kPa)	Love (FS=1.3) (kPa)	Talbot Reductions (kPa)	Finite Element Analysis (kPa)
194	108	284	335	250	235
223	124	326	385	300	270
252	140	368	435	350	305
280	156	409	484	400	339
310	172	453	536	450	374

2.1.2.1.4. Comparison of the Stress Models

The distribution of stress values for the different methods is shown in (Table 2.2). For the Love (FS = 1), Talbot reductions, and finite element analysis, the stress range for lower wheel loads (235 kPa to 284 kPa) is smaller than at high wheel loads (374 kPa to 453 kPa). The Love (FS = 1.3) stress calculations show how the factor of safety greatly varies the stress range over the wheel loads studied. The Talbot reduction calculations were used for this study because they fall within the range of calculated stresses, from both the Love equation and the finite element modeling, as well as, for consistency and comparability with previous studies at UW-Madison (Ebrahimi 2011; Keene 2012).

2.1.2.2. Resisting Track Shifting and Settlement

Surface deviation of track occurs when there is not enough confining pressure around the ties. The ties can therefore shift in the ballast structure when a load is applied or due to track buckling cuased by thermal expansion or contraction of the rail (Figure 2.6). Lack of confining pressure can be caused by lack of ballast on the shoulders or large spacing of the ties and can lead to track settlement (Indraratna et al. 2009). Over time, with loading, the ballast will shift under pressure and deform and deteriorate due to loadings. This causes the structure of interlocked ballast particles to lose stability and confining pressure because the track substructure no longer acts like a rigid structure.

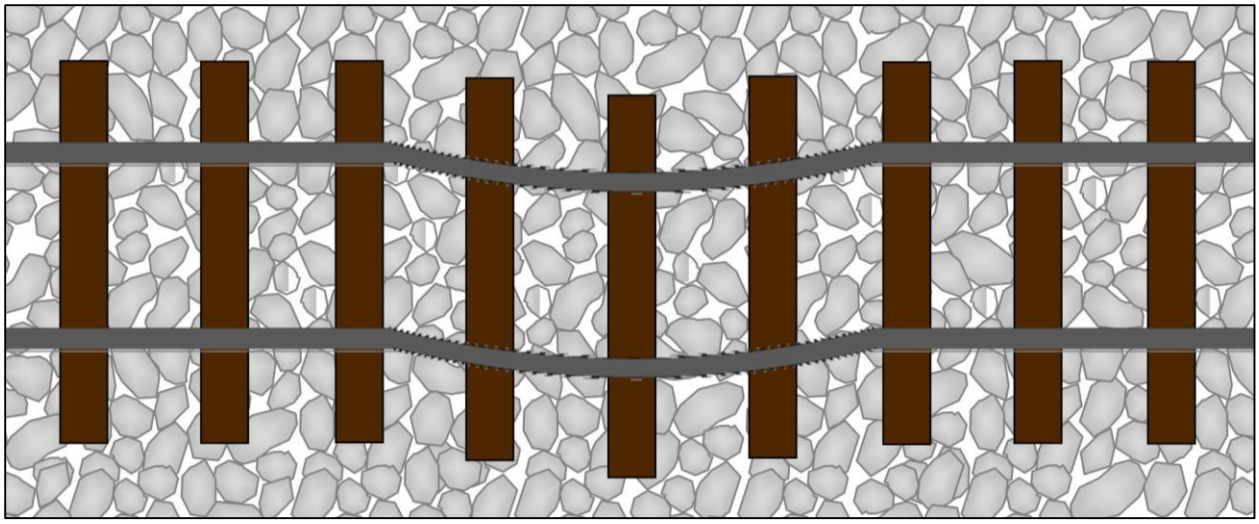

Figure 2.6 Surface Deviation of Track.

2.1.2.3. Ballast Fouling and Water Retention

In fresh ballast, the fouling process for ballast begins with the applied load breaking down the ballast particles (Selig and Waters 1994). This breakage or scuffing of the ballast results in finer-grained material being introduced into the void spaces. Due to the continued loading of trains over time, the fine-grained material can work its way in between the ballast contact points further degrading and breaking the large ballast particles (Tutumluer et al. 2008). A clean ballast structure is designed to have large enough voids to allow for adequate water drainage under most conditions. However, when fine-grained material begins to accumulate in the void spaces, the bulk hydraulic conductivity decreases. This retention of pore water in granular material coupled with high frequency, high pressure loadings could result in areas of excess pore water pressure under the right conditions. The conditions for this study consist of large ballast matrix with fine grained saturated particles where excess pore water pressures would exert pressure on the ballast particles and destabilize the ballast structure. However, Selig and Waters (1994) noted that sand and fine gravel-size particles will increase the shear strength and stiffness of the ballast as long as the original ballast skeleton is intact.

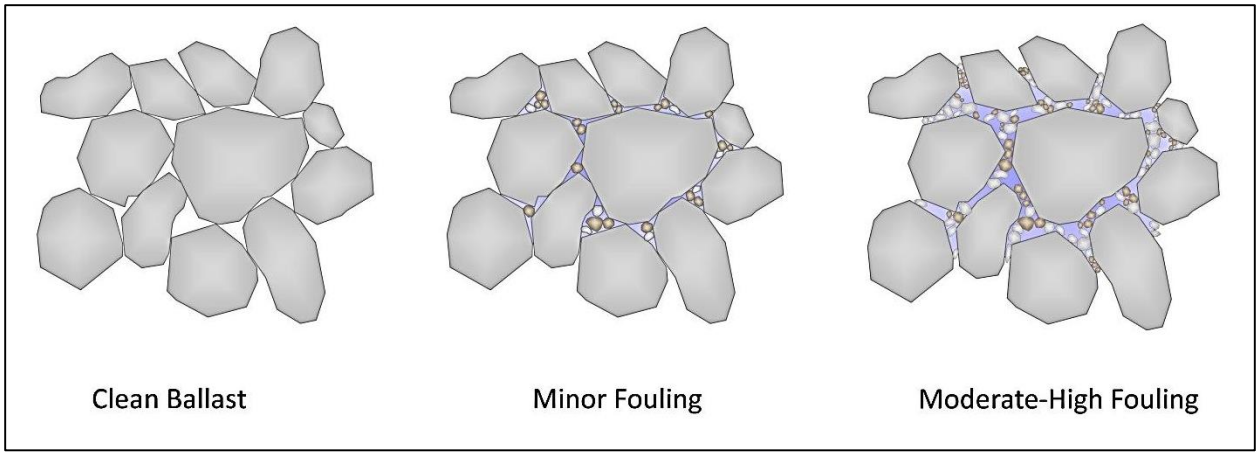

Figure 2.7 Diagram of Fouling Content Levels.

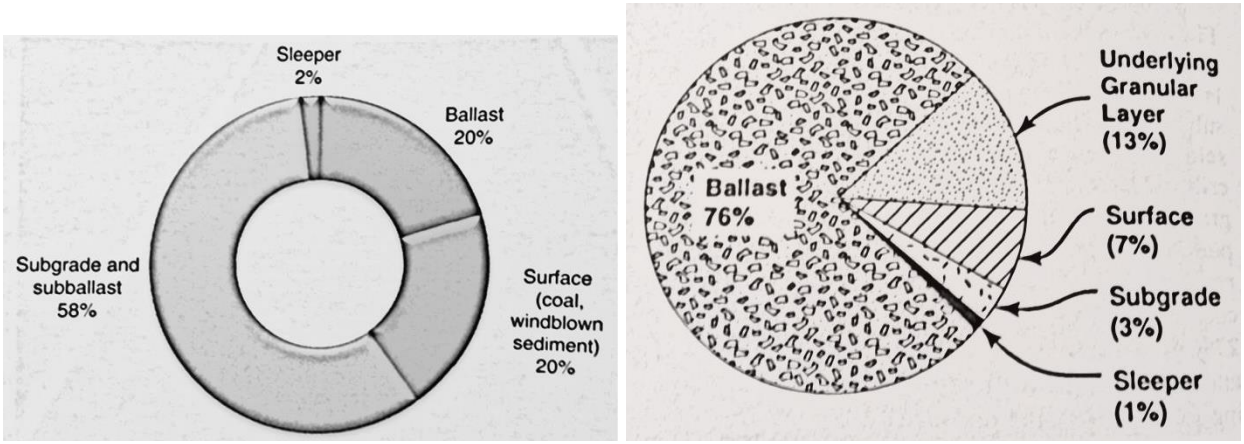

Figure 2.8 Fouling contribution breakdown (a) (Indraratna et al. 2011) and (b) (Selig and Waters 1994)

The accumulation of fine grained material happens in five main ways: (1) ballast breakdown, (2) infiltration from ballast surface, (3) tie wear, (4) infiltration from underlying granular layers, and (5) subgrade infiltration (Selig and Waters 1994) (Figure 2.8). In Indraratna (2011), the main cause of ballast fouling is from subballast or subgrade intrusion while Selig and Waters (1994) found that ballast breakage was the main source of fouling. Between the two, surface fouling accounts for 7% to 20% of the fouling accumulation.

2.1.2.4. Track Deflection and FRA Standards

Track deflection occurs when the track deviates from the initial profile due to deformation in the substructure in the ballast, subballast, or subgrade layer. This deformation in the ballast layer is typically caused by a shifting of ballast particles, a deformation of the ballast particles over successive loadings, or a breakage and deterioration of ballast particles due to weathering, fouling, or loading conditions (Selig and Waters 1994; Indraratna et al. 2011). Other types of fouling material (e.g., coal, mineral fouling, and clay) have been studied and found to effect the rate of plastic deformation in the ballast structure (Ebrahimi 2011; Tutumluer et al. 2008). Therefore, the primary concern for this study is the effect of fracing sand and moisture on plastic deformation of the ballast that can cause this deflection, which ultimately results in reduced speed limits, increased damage to the super-structure, and, under worst-case conditions, even train derailment. Understanding and quantifying this track deflection by using the LSCT method of measuring plastic strain with parameters that mimic field conditions, is therfore, crucial to the freight rail industry.

The Federal Rail Administration (FRA) has specifications for all of the track components (FRA 2011). Though this document has standards for gage width, clearance heights, and everything else related to rail maintenance and safety this study is primarily concerned with the track settlement allowances. Table 2.3 shows the FRA allowances for cross-level and tangent track for each class of track. The class used in this study is class 5 track, and the application of this limit is described further in section 5.1 and 5.2.

Table 2.3 Shows the allowances for surface of rail for each class (1-5) and for both cross-level and tangent track (FRA 2011).

Track surface	Class of track				
	1 (inches)	2 (inches)	3 (inches)	4 (inches)	5 (inches)
The runoff in any 31 feet of rail at the end of a raise may not be more than.	3½	3	2	1½	1
The deviation from uniform profile on either rail at the mid-ordinate of a 62-foot chord may not be more than	3	2¾	2¼	2	1¼
The deviation from zero crosslevel at any point on tangent or reverse crosslevel elevation on curves may not be more than	3	2	1¾	1¼	1
The difference in crosslevel between any two points less than 62 feet apart may not be more than* [1,2]	3	2¼	2	1¾	1½
*Where determined by engineering decision prior to the promulgation of this rule, due to physical restrictions on spiral length and operating practices and experience, the variation in crosslevel on spirals per 31 feet may not be more than	2	1¾	1¼	1	¾

[1] Except as limited by §213.57(a), where the elevation at any point in a curve equals or exceeds 6 inches, the difference in crosslevel within 62 feet between that point and a point with greater elevation may not be more than 1½ inches. (Footnote 1 is applicable September 21, 1999.)

[2] However, to control harmonics on Class 2 through 5 jointed track with staggered joints, the crosslevel differences shall not exceed 1¼ inches in all of six consecutive pairs of joints, as created by 7 low joints. Track with joints staggered less than 10 feet shall not be considered as having staggered joints. Joints within the 7 low joints outside of the regular joint spacing shall not be considered as joints for purposes of this footnote. (Footnote 2 is applicable September 21, 1999.)

2.2. Heavy Axle Loads (HAL)

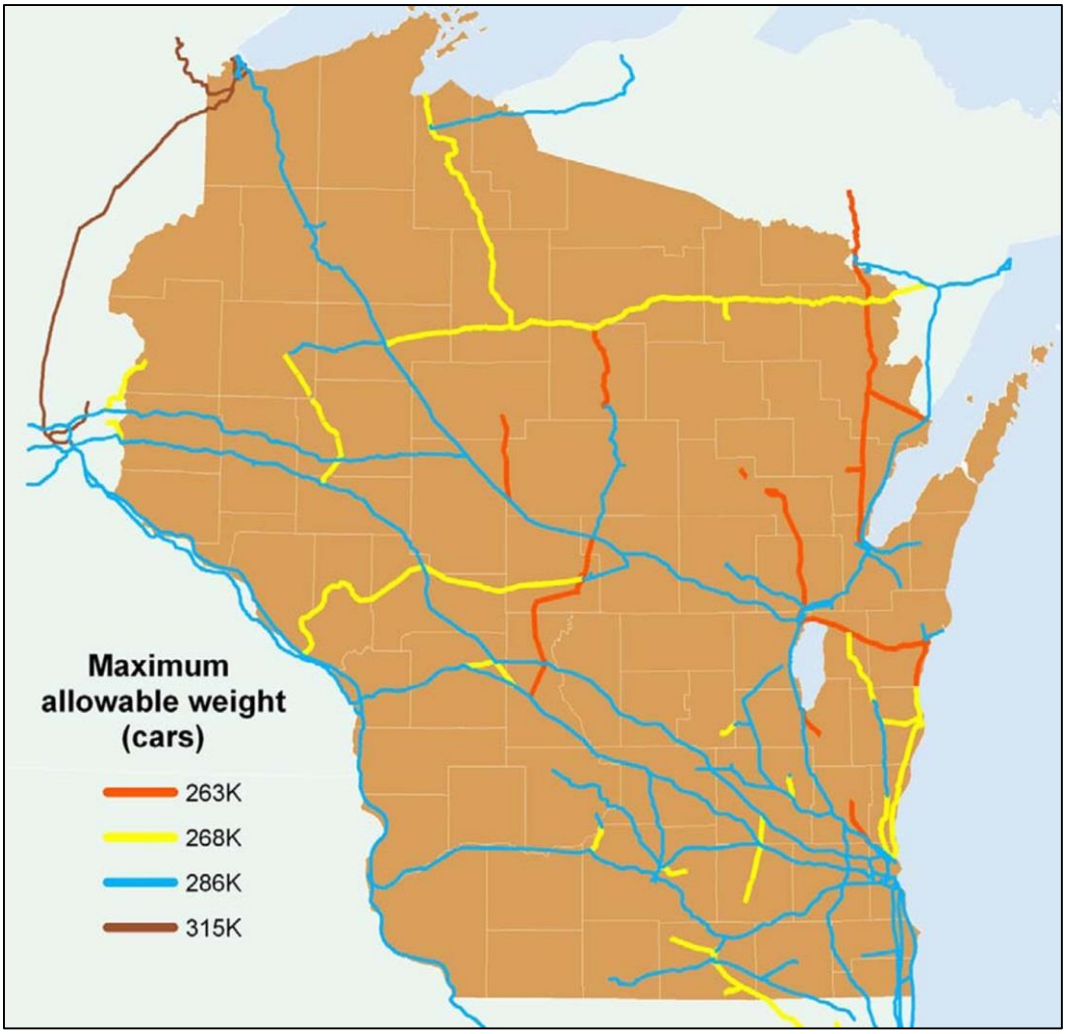

Figure 2.9 Wisconsin's maximum allowable weight (in thousands of pounds) for freight rail cars (Wisconsin DOT 2010).

2.2.1. Maintenance and Upgrade Costs

Limited publicly accessible sources are available for determining the costs of maintenance for railroads. Available sources will be used in this study to attempt to estimate costs associated with the transportation of frac sand across the US freight network (Figure 2.10). There are seven Class I railroads in the US with a total of 222,900 km (138,500 miles) of track (AAR 2013). In 2011, the total cost to maintain this network was estimated at $8.7 billion, which calculates to $39,150 per km ($63,000 per mile) (AAR 2011). BNSF spends around $200 million per year for the top 51-61 cm (20-24 in) of ballast maintenance (BNSF 2013). In 2012, BNSF owned an estimated 52,300 km (32,500 miles) of track which results in $3,800 per km ($6,100 per mile) for ballast maintenance (BNSF 2012). Zarembski (2001) reported that the cost for the short line and regional railroads upgrades to handle 286,000 lb cars would total $6.9 billion (Table 2.4) in 2001, with ballast/surfacing investments of $1,650 per km ($2,657 per mile). In a recent article in the Fedgazette (Davies 2012), from July 2012, railroad companies in the Wisconsin sand mining region have invested $0.62 million to $1.24 million per km ($1 million to $2 million per mile) for restoration and rehabilitation of dormant rail lines.

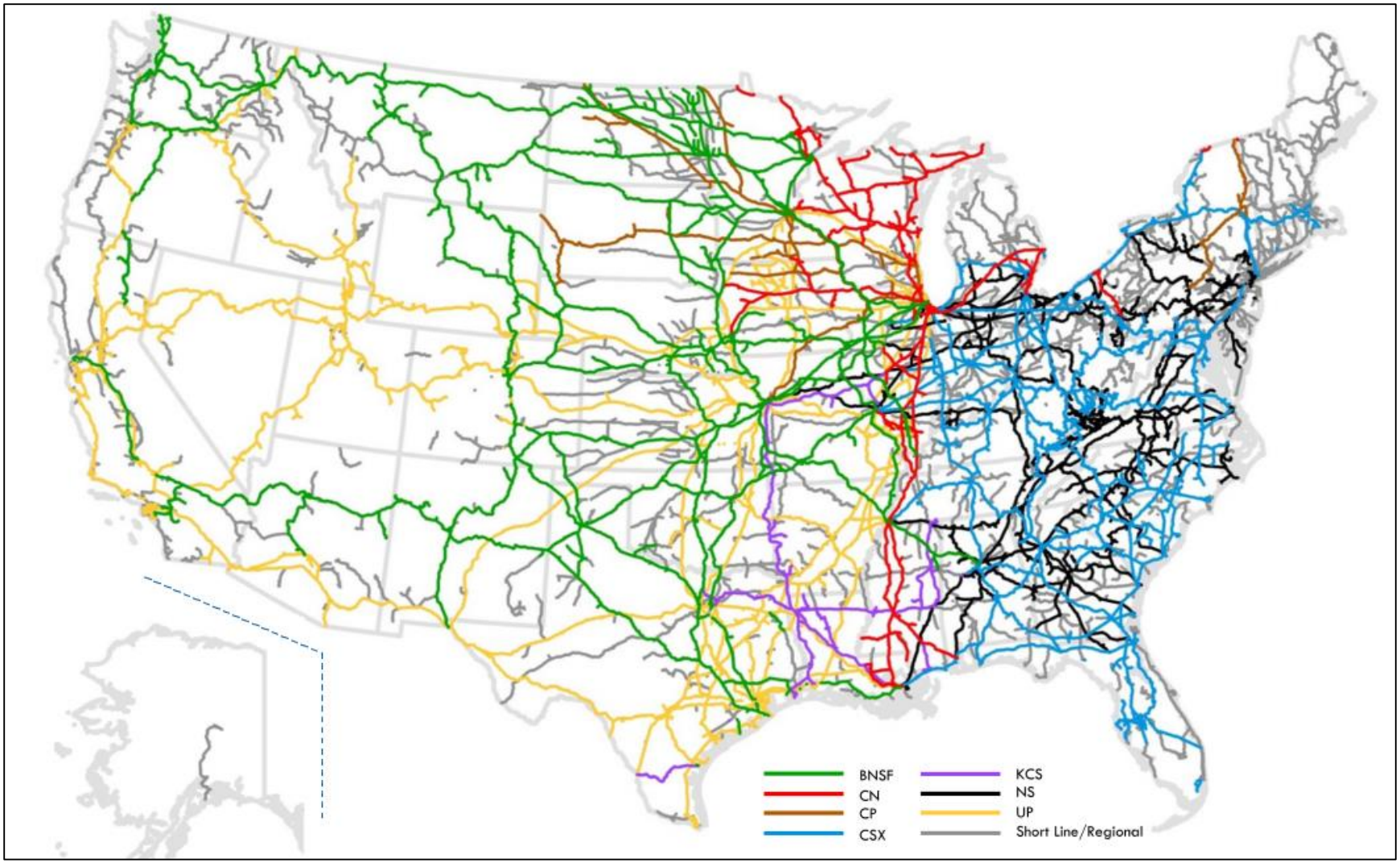

Figure 2.10 United States Freight Rail Network (AAR 2013).

2.2.2. Short Line Implications for Wisconsin

While HAL likely increase the deterioration of track components, including the ballast, there is potential operational savings due to needing fewer cars for the same load and reducing fuel consumption because of reduced overall train weight per ton of material hauled (Zarembski 2000a). However, for the short lines, the net benefit of increasing the axle load may not have a net benefit as they are, typically smaller operations, with limited tonnage as compared to the Class 1's. The maintenance costs for short lines would likely be similar or higher than Class 1's, while the capital costs for upgrades and infrastructure replacement like bridges would be a significant burden to the short lines. As the Class 1 railroads convert to heavier axle loads, the short lines may be compelled to upgrade as well even if it is at a net loss (Zarembski 2000b).

Table 2.4 Cost to upgrade short line and regional railroads to handle 286,000 lb cars (Zarembski 2001).

Calculated cost of upgrading short line and regional railroads to handle 286,000-pound cars

Component	Total cost (industry)	Required investment per mile
Rail	$3,754,182,002	$75,106
Ties	$818,362,236	$16,372
Ballast/surfacing	$132,789,720	$2,657
Turnouts	$393,996,056	$7,882
Bridges	$1,761,253,773	$35,236
Total	$6,860,583,787	$137,253

2.2.3. Class I Implications

Class 1 railroads may have the most benefit and least risk for upgrading to HAL. Studies have shown that there is a net benefit on the order of 5% for increasing the axle loading for Class 1 railroads (Zarembski 2000a). For Class 1's, the benefit comes mostly from the operational side where less cars for the same tonnage is more efficient and saves on overall consumption. A main concern for Class 1's upgrading to heavier axle loads is the potential for increased wear and tear on the track components. Table 2.5 outlines the costs and benefits from a 2000 article on the subject of short line railroads and HAL. As shown, there is significant damage to rail, ties, and ballast, especially if the ballast is in less than acceptable condition.

Table 2.5 HAL costs and benefits broken down by track components and gross weight loadings (Zarembski 2000b).

HAL benefits		
Gross weight on rail	**Net to tare ratio**	
263,000 lb	3.1	
286,000 lb	3.5	
315,000 lb	3.7	
HAL damage factors	**Damage**	**Damage**
	(% per axle)	**(% per MGT)**
Rail wear	+9	0
Rail fatigue (internal)	+29	19
Rail fatigue (surface)	+16	7
Rail joints	+32	21
Ties	+13	4
Good ballast	+9	0
Poor ballast	+60	47
Turnouts	+29	19

2.3. Ballast Mechanics

2.3.1. Factors Affecting Ballast Behavior

Factors that govern the mechanistic properties of individual ballast particles include particle size, particle shape, surface roughness, parent rock strength, and particle crushing strength. Factors that affect the performance of bulk ballast include particle-size distribution, void ratio, degree of saturation, confining pressure, number of cycles, and frequency and amplitude of loading (Indraratna et al. 2011; Selig and Waters 1994). Figure 2.11 shows typical settlement and maintenance cycles for ballast track. The settlement curves vary with the dependence on factors mentioned above, as well as the types of fouling and amount of water present in the ballast structure. The following sections give more detail on these key factors and how they affect ballast deformation and track settlement.

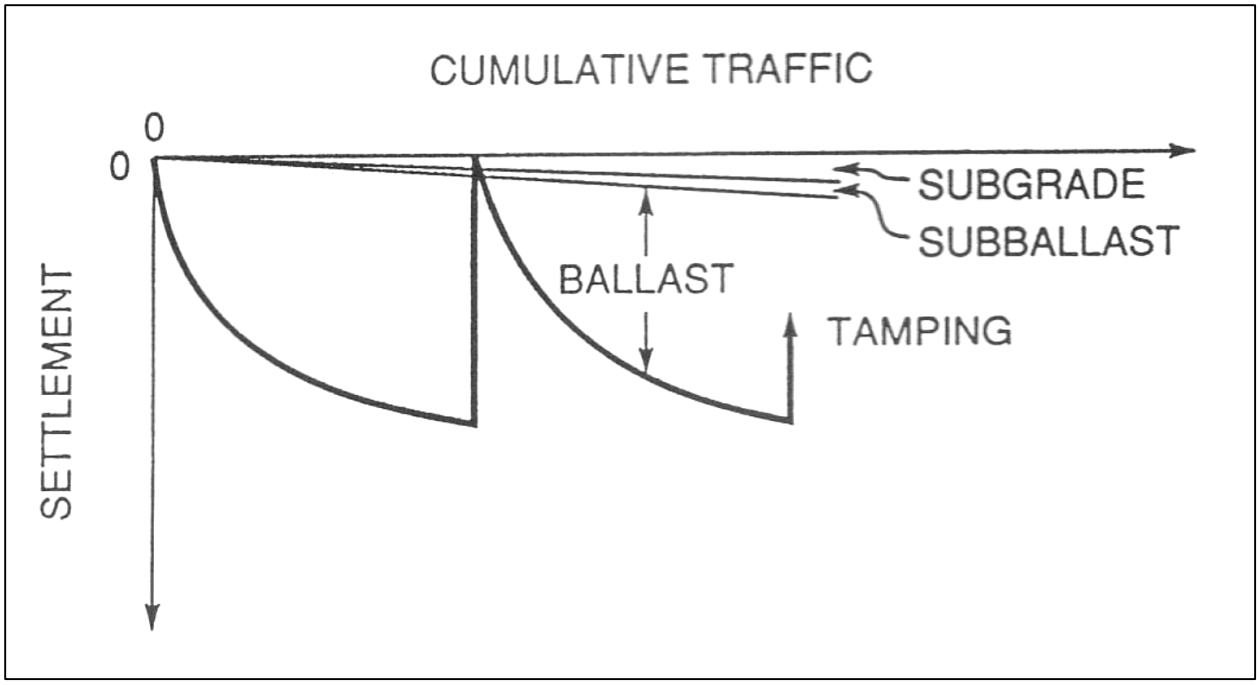

Figure 2.11 Typical settlement characteristics of ballast, subballast, and subgrade (Selig and Waters 1994).

2.3.1.1.Particle Size and Grading

The effect of particle size on ballast behavior has been studied with varying results. Selig and Waters (1994) recommends that ballast should fall between the range of 10 mm to 50 mm with the larger particles contributing the most to stability, and the smaller particles increasing the contact points while reducing the contact forces between the larger particles and minimizing breakage. Indraratna et al. (1998) found that, at low confining pressures, peak friction angle decreased slightly with an increase in grain size. A study by Kolbuszewski and Frederick (1963) showed that the angle of shearing resistance increases with an increase in large particles. Dawson et al. (1996) determined that poorly-graded specimens provided a higher stiffness compared to well-graded specimens. Raymond and Diyaljee (1979) determined that well-graded ballast has lower settlement than poorly graded ballast. Since the gradation of the ballast also affects the drainage capacity and the internal angle of friction, an ideal ballast gradation would be optimized to reduce settlement, increase stiffness, and be free draining.

2.3.1.2.Particle Shape, Angularity and Roughness

Particle shape is important in ballast because angularity increases the interlocking ability and friction between particles, which increases the shear strength (Indraratna et al. 1998). Sphericity, angularity, and roughness affect the behavior of particles as well. Platiness decreases stiffness, while angularity and roughness decrease small-strain stiffness and increase high-strain strength in soil (Santamarina and Cho 2004). The amount of roughness or texture of the ballast determines the frictional forces at the contact points. Thom and Brown (1988) noted that increasing the surface roughness increased the resilient modulus, concluding that increasing surface roughness

increased the resistance to plastic strain accumulation. Thus, particle shape, angularity, and roughness are all important parameters for determining the mechanistic behavior of ballast.

2.3.1.3.Parent Rock Strength

Parent rock strength is a critical factor for ballast deformation, track settlement, and lateral deformation. Parent rock strength is not typically measured, but the Los Angeles Abrasion test is sometimes performed to assess the durability and strength of the parent rock. Understanding the petrology of the parent rock source can also give a reasonable estimate of the strength and durability of the ballast particles.

2.3.1.4.Particle Crushing Strength

Particle crushing strength is dependent on the parent rock, grain geometry, contact points, and loading direction (Indraratna et al. 2011). Particle breakage typically only happens in high stress loadings, while grain abrasion can occur at any stress level. The particle crushing strength is not a standard defined or required by the FRA, but can be found on some ballast specifications.

2.3.1.5.Void Ratio

Void ratio is an important characteristic for understanding the mechanical behavior of particular medium (Indraratna et al. 2011). Low density ballast (high void ratio) results in high plastic strain (Figure 2.12), (Selig and Waters 1994; Knutson 1976). The importance of high-density ballast must be weighed against compaction effort as well, due to the risk of particle breakage with too much compaction effort or not implementing slow train speed initially after maintenance activity.

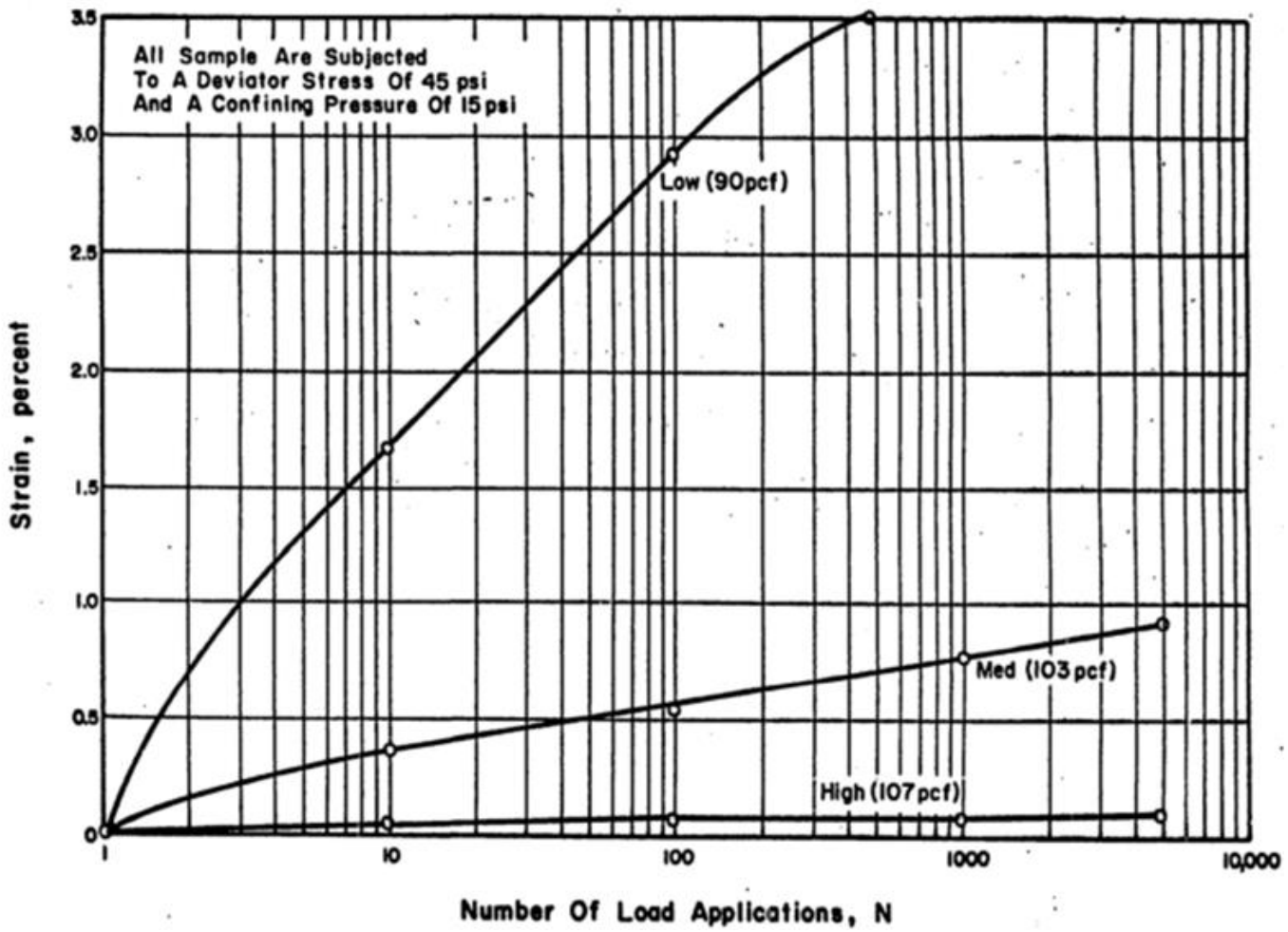

Figure 2.12 Ballast density variations (Knutson 1976).

2.3.1.6.Degree of Saturation

Degree of saturation affects the mechanical behavior primarily by affecting any fine content in the ballast or subballast layers. Clay pumping is a primary ballast fouling mechanism where fine-grained content is introduced to the ballast from the bottom up (Selig and Waters 1994). Degree of saturation will also affect any fouling that is introduced into the ballast structure from the surface as well. For this study, frac sand spillage into the ballast with the effects of moisture is covered in Section 2.4.

2.3.1.7.Confining Pressure

The effect of confining pressure is critical for the deformational behavior of granular medium (Indraratna et al. 1998; Christie et al. 2005; Brown and Hyde 1975). These studies show that confining pressure has some effect on the ballast breakage; however, Christie et al. (2007) recommends that, if axle loads are increased, the confining pressure would need to increase to minimize ballast breakage. Indraratna et al. (1998) found that the shear strength and deformation at low confining pressures deviated significantly from high confining pressure results. Christie et al.(2005) also found that low confining pressures of *in situ* test condition resulted in high vertical deformation, dilation, and increased corner breakage of the ballast.

2.3.1.8.Number of Load Cycles

An increase in the number of load cycles increases the amount of plastic strain on granular material. The rate of plastic strain accumulation is often dependent on other factors (fouling content and moisture retention) and has been studied previously by (Lim 2004; Ebrahimi 2011). Generally, the rate of strain accumulation tends to decrease as

the number of cycles increases and is approximately linear with a semilogrithmic graph of load cycles vs. deformation (Shenton 1975) (Figure 2.13).

2.3.1.9.Frequency and Amplitude of Loading

Shenton (1975) showed that the frequency of loading had no significant effect on the permanent deformation of the ballast. In contrast, recent findings by Indraratna et al.(2010) showed that frequency of loading has a significant impact on deformation and that ballast breakage also increased with increasing frequency (Figure 2.14).

2.3.2. Key Properties Affecting Resilient Modulus

Resilient modulus is defined as the repeated deviator stress divided by the strain (Selig and Waters 1994). During cyclic loading the initial strain is often greatest and recurring loads typically tend toward a constant resilient strain rate after a certain number of loads. The number of loads necessary to reach a constant plastic strain rate is dependent on the conditions and the type of material. As shown in Figure 2.15, the resilient strain is the recoverable strain from every loading cycle, whereas the plastic strain is the non-recoverable portion. This study is concerned primarily with the plastic strain of ballast under loading and the rate of plastic strain accumulation.

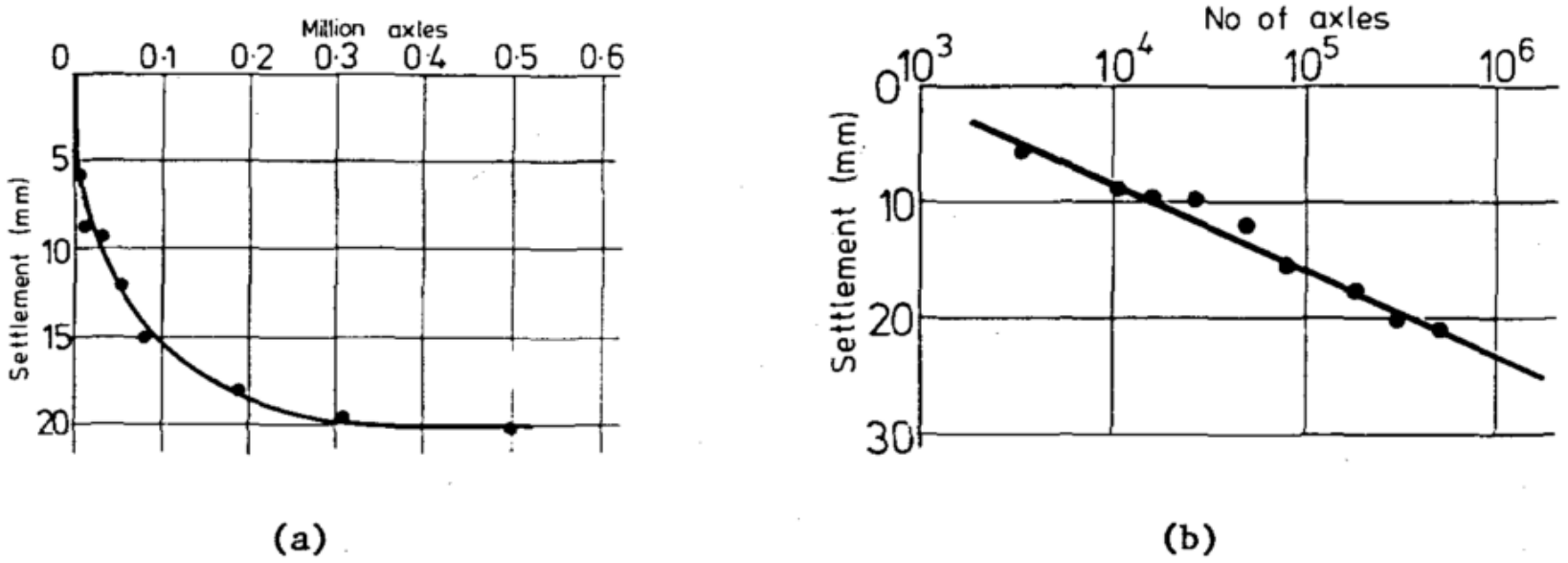

Figure 2.13 Plots of settlement vs. number of loadings in Cartesian (a) and semilogrithmic (b) (Shenton 1975).

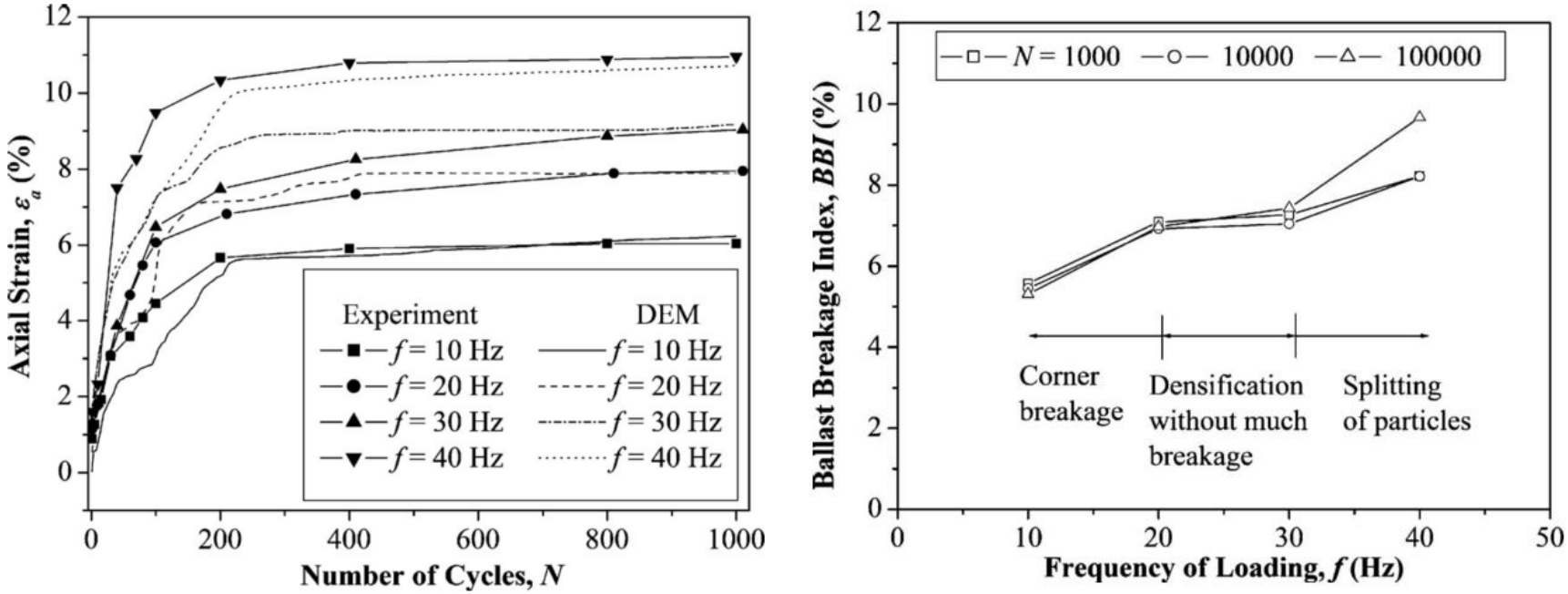

Figure 2.14 Effect of frequency on ballast deformation and ballast breakage (Indraratna et al. 2010).

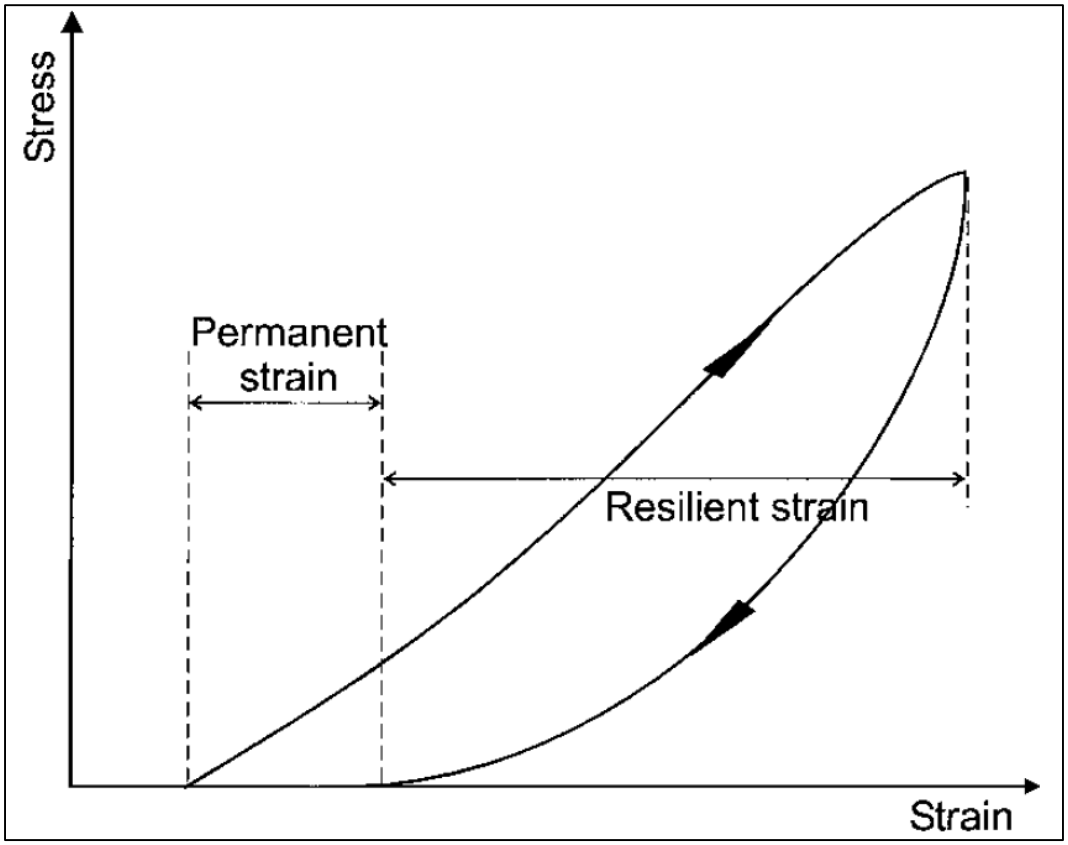

Figure 2.15 Diagram of the total, permanent, and resilient strain as a function of stress (Lekarp et al. 2000).

2.3.3. Key Factors Affecting Permanent Strain

Plastic strain is defined as the portion of the strain that is non-recoverable (Figure 2.15). A number of key factors affect plastic strain accumulation in ballast including initial density and void ratio, stress conditions, particle shape and gradation, fouling content, and moisture content (Knutson 1976; Shenton 1975; Christie et al. 2005; Indraratna et al. 1998; Ebrahimi 2011). Shenton (1975) showed that initial strain varies with initial porosity and that density matters greatly for the first cycle plastic strain (Figure 2.16).

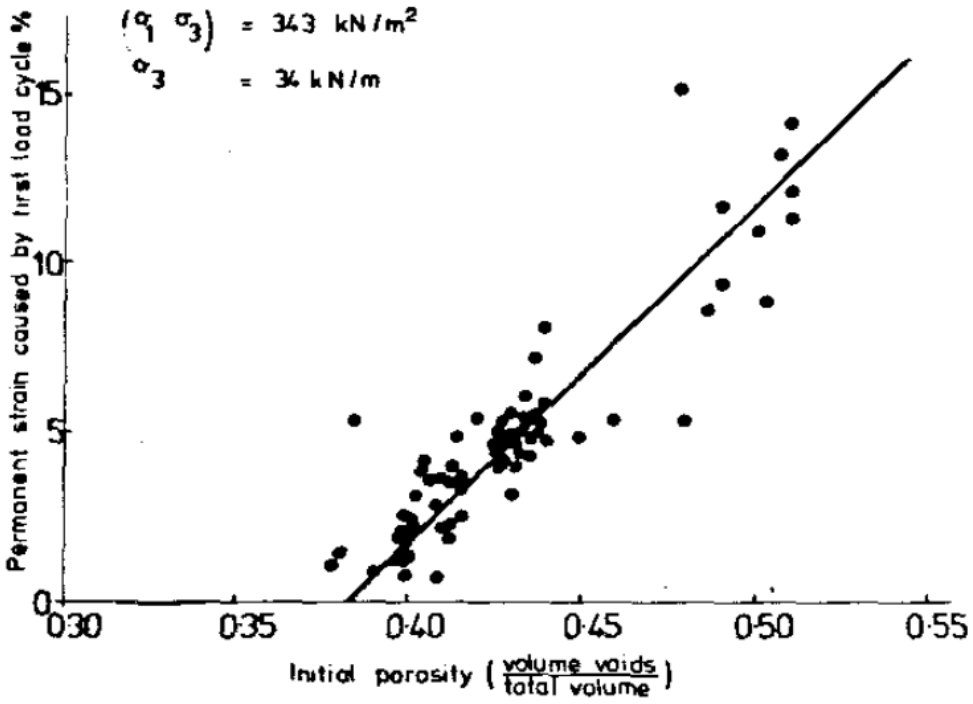

Figure 2.16 Diagram showing first cycle plastic strain variation as a function of porosity (Shenton 1975).

Confining pressure has a significant effect on ballast behavior (Christie et al. 2007). An increase in moisture content increased the rate of plastic strain in granular materials (Li and Selig 1996) and in fouled ballast (Ebrahimi et al. 2010). The types of fouling (plastic vs. nonplastic) changes the ballast response as does the moisture retention and mechanical properties of the fouling material (Ebrahimi 2011).

2.4. Sand Mechanics

2.4.1. Sand under Cyclic Load

Cyclic triaxial testing on sand has been historically conducted to understand liquefaction caused by earthquakes, repeated loadings for highway subgrade design, or wind turbine foundation design (Morgan 1966; Ravichandran et al. 2010; Mohamad and Dobry 1987; Ghionna and Porcino 2006). There are a few key factors expressed in this research that may play a role in understanding the effect the moist frac sand will have on the cyclic response of the structure as a whole. Triaxial tests on soils can be cyclic or monotonic, drained or undrained, consolidated or unconsolidated, and isotropic or anisotropic. Depending on the hydraulic conductivity of the soil and the rate of loading there may be cases where the soil behaves in an undrained condition due to the inability for the excess pore water pressure to dissipate. Also, due to the large size of the ballast particles relative to the size of the specimen, anisotropic conditions may occur as well.

2.4.2. Frac Sand Effects on Ballast Behavior under Cyclic Loading

Previous research on fouling content in ballast has posed reasons for the increase in plastic strain accumulation (Selig and Waters 1994; Tutumluer et al. 2008; Ebrahimi

2011). Fouling through breakage of particles, infiltration from the surface of coal dust or windblown soils, and clay pumping all lead to an increase in the fines content of the ballast structure, which allows for higher moisture retention. Increased coal dust and moisture retention decreases the shear strength of ballast to the point that the friction angle of fully fouled ballast is equal to that of the coal dust (Tutumluer et al. 2008).

Particle breakage both in the ballast and in the frac sand could result due to restricted movement of both materials during cyclic loading. This could lead to stress development that would be greater than the maximum strength of the particles leading to sand or ballast crushing or angular corner breakage. Zhang and Baudet (2013) studied the effect of particle breakage in 1D compression for gap-graded soils and found significant particle breakage for medium to high stresses (12 MPa and 25 MPa). Though this study used high vertical stresses, the number of loading cycles for the current work could result in particle breakage by similar mechanisms (e.g., angular corner breakage or particle crushing).

Chapter 3: Materials

The following sections describe the tests conducted to collect the relevant properties of the frac sand and ballast used in this study. These properties then are used to develop a testing (deformation-type tests) matrix for mixtures of ballast, sand, and moisture for use in the large-scale cyclic triaxial (LSCT) testing described in Section 4

3.1. Frac Sand

Determination of the basic mechanical/physical properties of frac sand requires a number of tests. This section contains detailed information about the standards, test methods, and results of these tests. The tests include grain-size distribution, shape characteristics, hydraulic conductivity, soil water characteristics, density, and void ratio. These properties are used to determine the amount of frac sand and moisture content for use in large-scale cyclic triaxial (LSCT) testing, which is described in Section 4. Three frac sand samples were obtained at different gradations to study the effect of grain-size distribution on moisture retention, which may show variation in ballast deformation. One sample was obtained from US Silica in Ottawa, IL; and two from Wisconsin Industrial Sand Company in Menomonee, WI.

3.1.1. Grain-Size Distribution and Phase Relationships

Three frac sand samples were obtained and used for the LSCT tests. The three gradations are “20/40”, “40/70”, and “70/140” meaning that, for example, the 20/40 sand passes the #20 sieve and is retained on the #40 sieve (in accordance with ASTM D6913). Figure 3.1 shows the grain-size distribution of the three samples.

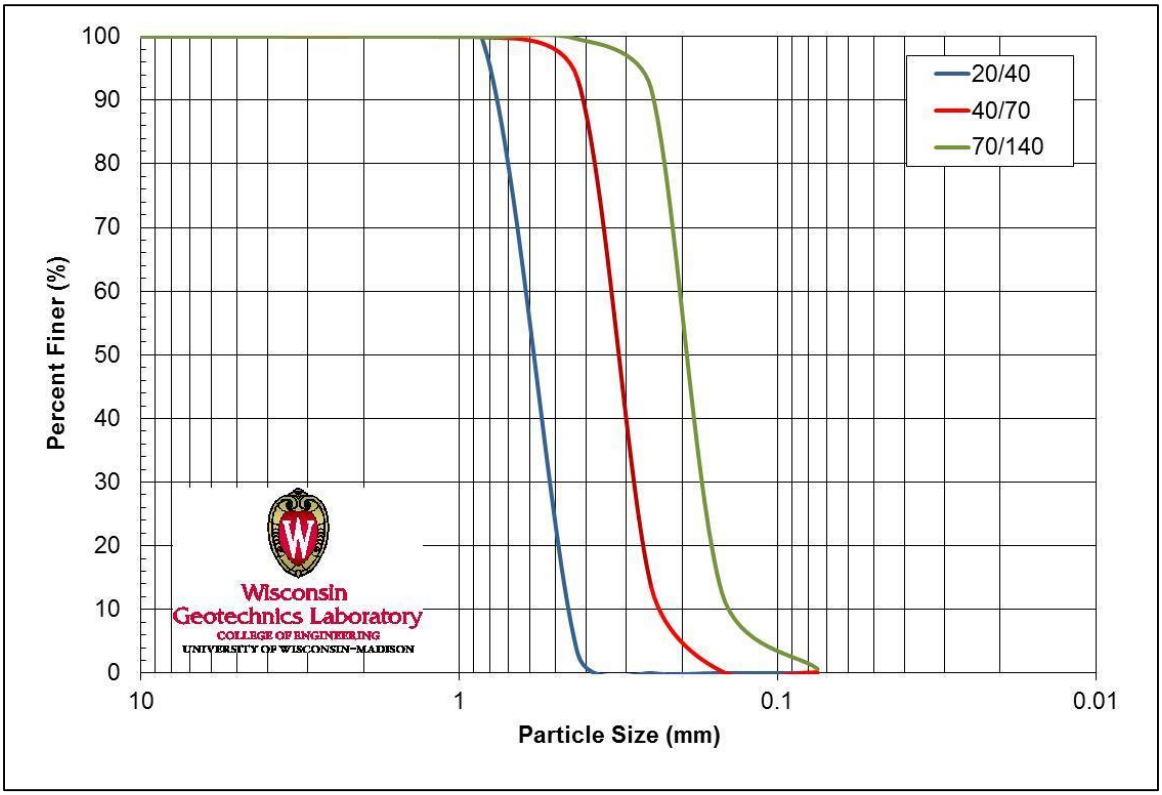

Figure 3.1 Grain Size Distribution of Frac Sand Samples(ASTM D6913).

Table 3.1 Summary of Frac Sand Properties [1]Calculated from ASTM D4253 & D4254 [2]Calculated from the grain size distribution curves, ASTM C136 [3]Cho et al. (2006)

Parameters	70/140 (fine)	40/70 (medium)	20/40 (coarse)
Dry Density Max[1] (g/cm^3)	1.64	1.69	1.69
Dry Density Min[1] (g/cm^3)	1.45	1.55	1.57
Void Ratio Max[1] (e_{sMax})	0.83	0.71	0.69
Void Ratio Min[1] (e_{sMin})	0.62	0.57	0.57
Average Grain Size[2] (mm)	0.19	0.29	0.57
Standard Deviation[2] (mm)	0.05	0.08	0.10
Maximum Size[2] (mm)	0.32	0.49	0.82
Minimum Size[2] (mm)	0.09	0.11	0.28
Coefficient of Uniformity[2] (C_u)	1.4	1.4	1.4
Coefficient of Curvature[2] (C_c)	1.0	1.1	0.94
Particle Regularity[3]	0.77	0.70	0.75

Density and void ratio was calculated using two methods as described in (ASTM D4253 and D4254). This method utilizes a vibratory table to allow for the sand to compact to its maximum density and its minimum void ratio. There are two conditions for running this test, wet or dry–the latter was applied for this research. The dry density method was used for this test on account of the ease of setup and reliability of the testing equipment. Table 3.1 summarizes the dry density, void ratio, particle regularity, and common parameters obtained from grain-size distribution test, minimum and maximum density tests, and particle shape tests.

3.1.2. Shape Characteristics

Particle shape reveals characteristics related to mineral composition, grain formation, transportation, and depositional environments (Cho et al. 2006). The micro-scale shape parameters of sphericity and roundness affect the macro-scale behavior of soil particles. The method outlined in (Cho et al. 2006) was used to characterize the two shape parameters as shown in Figure 3.2.

$$Sphericity = \frac{r_{max-in}}{r_{min-cir}} \qquad Roundness = \frac{\sum r_i / N}{r_{max-in}} \qquad \text{Eqn. 3-1.}$$

Particle shape results show roundness ranging from 0.79 to 0.83 and sphericity ranging from 0.61 to 0.71 for the three frac sand gradations. Cho et al. (2006) indicates that shear deformation is limited in dense soils due to angularity, sphericity, and roughness; all of which limit particle rotation and dilation. However, at low densities, shear deformation causes chain bucking and particle rotation that leads to gradual density increases. Because frac sand has high sphericity and low roughness, low shear resistance is anticipated at all densities.

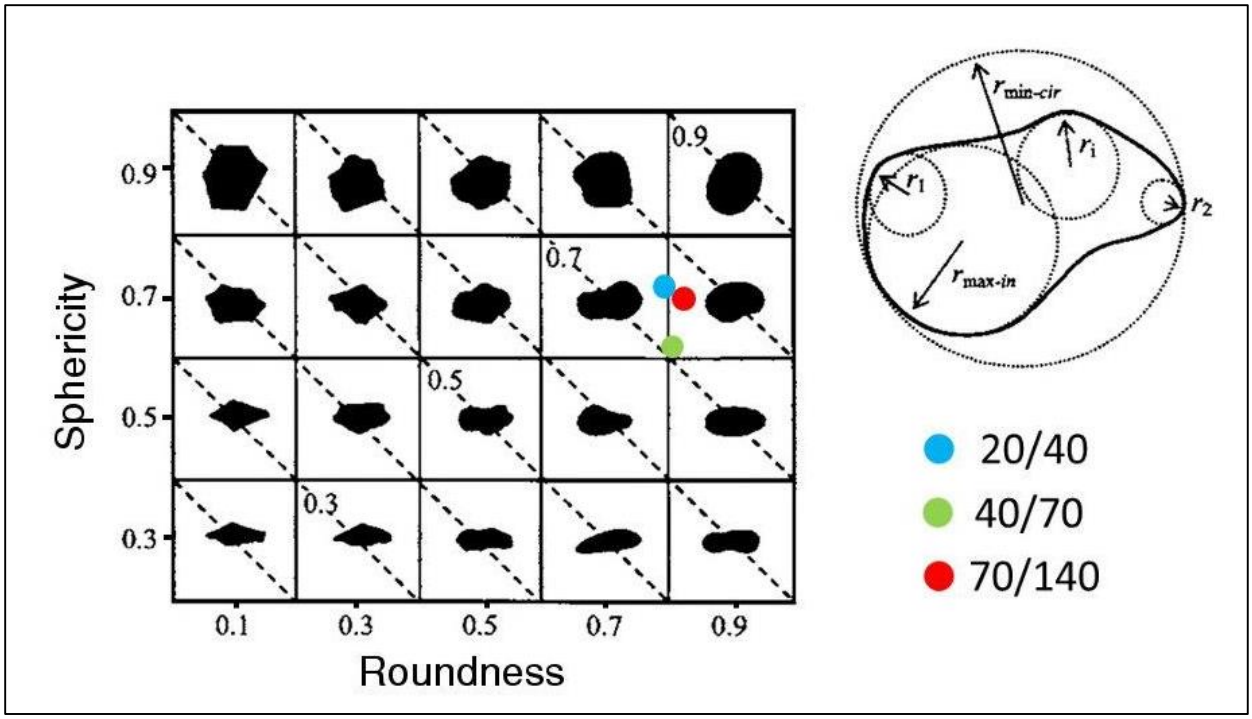

Figure 3.2 Shape Parameters for Frac Sand Samples (Cho et al. 2006).

3.1.3. Hydraulic Conductivity

Hydraulic conductivity of the sand specimens was performed using a constant head permeameter. The test was conducted at three different void ratios for each specimen to show the variation in hydralic conductivity over the range in density. The results are shown in the Figure 3.3. The results of the hydraulic conductivity tests are around the range typically assumed for poorly graded sand (Figure 3.4). The conductivity decreases as the nominal size of the particle decreases as would be expected. The conductivity also decreases as the void ratio increases and, for this study, the high void ratio conductivity results will be most relevant.

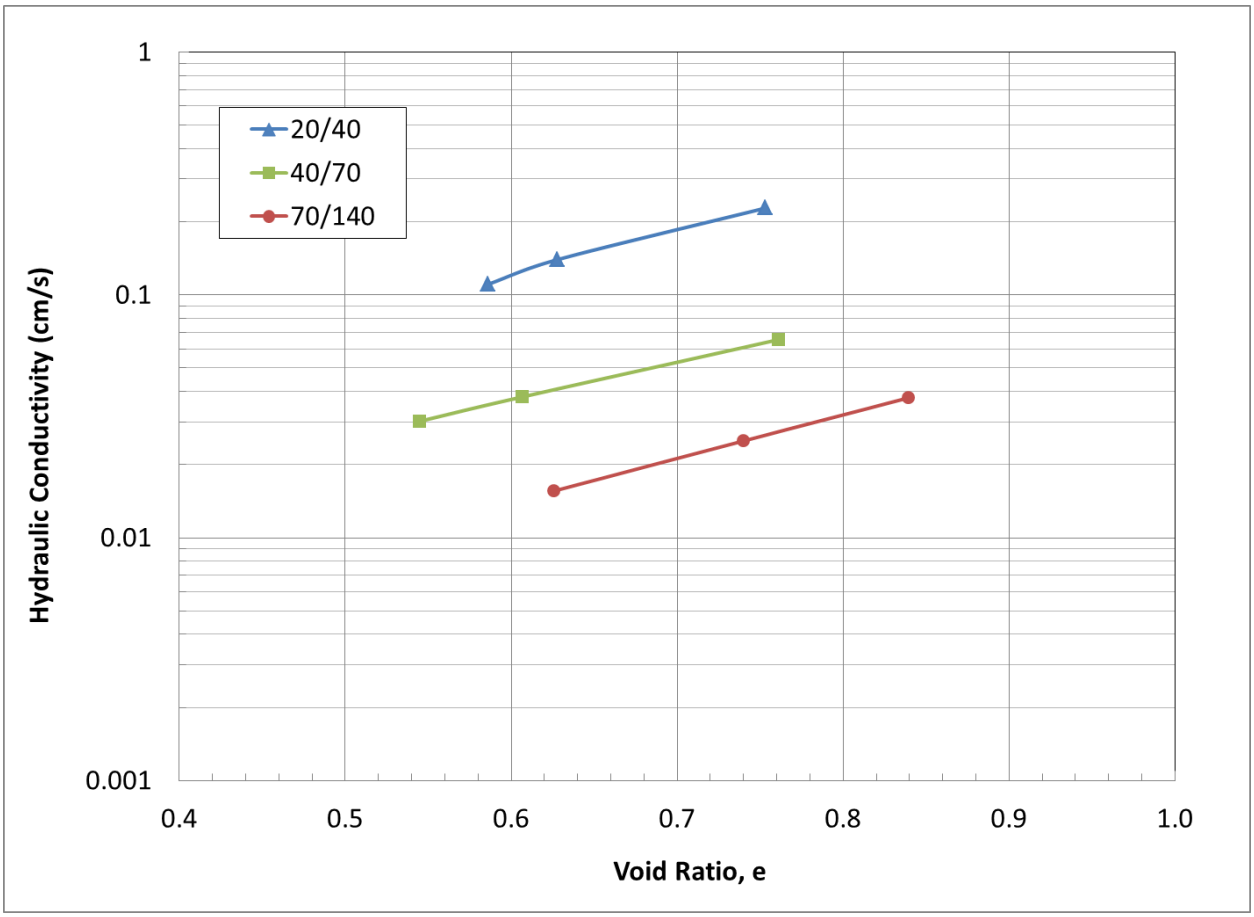

Figure 3.3 Hydraulic Conductivity of Frac Sand Samples(ASTM D2434 2006).

TABLE 1
Permeability and Drainage Characteristics of Soils

	Coefficient of Permeability k in cm per sec (log scale)										
	10^{2}	10^{1}	1.0	10^{-1}	10^{-2}	10^{-3}	10^{-4}	10^{-5}	10^{-6}	10^{-7}	10^{-8}	10^{-9}
Drainage	Good							Poor	Practically Impervious			
Soil types	Clean gravel		Clean sands, clean sand, and gravel mixtures			Very fine sands, organic and inorganic silts, mixtures of sand silt and clay, glacial till, stratified clay deposits, etc.				"Impervious" soils, e.g., homogeneous clays below zone of weathering		
					"Impervious" soils modified by effects of vegetation and weathering							
Direct determination of k	Direct testing of soil in its original position-pumping tests. Reliable if properly conducted. Considerable experience required											
	Constant-head permeameter. Little experience required											
Indirect determination of k			Falling-head permeameter. Reliable. Little experience required			Falling-head permeameter. Unreliable. Much experience required			Falling head permeameter. Fairly reliable Considerable experience necessary			
	Computation from grain-size distribution, i.e., Hazen's formula. Applicable only to clean cohesionless sands and gravels									Computation based on results of consolidation tests. Reliable. Considerable experience required		

SOURCE After Casagrande and Fadum (1940).

Figure 3.4 Typical ranges of hydraulic conductivity (Casagrande and Fadum 1940)

3.1.4. Soil-Water Characteristic Curves

The soil-water characteristic curves for the three sand samples were determined using ASTM D6836 and the hanging column method (Figure 3.5). This method was chosen for the ease of setup as well as the ability to apply precise suction at low values, which were expected from the grain-size distribution curves. The first two tests showed that, at low suctions, the horizontal interface would increase initially (0~12 h) and then subsequently drop shortly after attaining maximum movement. This resulted in data that would be insufficient for predicting any water retention properties or assigning fitting curve parameters. A solution was devised to monitor the pressure, temperature, and relative humidity in the testing room as well as to record the movement of the air water interface in the horizontal tube with a camera. The monitoring of temperature, pressure, and relative humidity over time would help in determining the cause of movement for the interface. The camera took pictures every 60 s to monitor the interface movement overnight. At each increase in suction, the horizontal interface increased, and the camera monitored the movement to predict when it would be most appropriate to increase the suction again. Only a few hours of steady interface was allowed before the next increment of suction was applied to avoid any drop in the interface that was seen in previous tests. Examination of the temperature, pressure, relative humidity, and interface movement for a full test yielded a potential cause. Due to the low relative humidity in the testing room, evaporation likely caused the interface to drop.

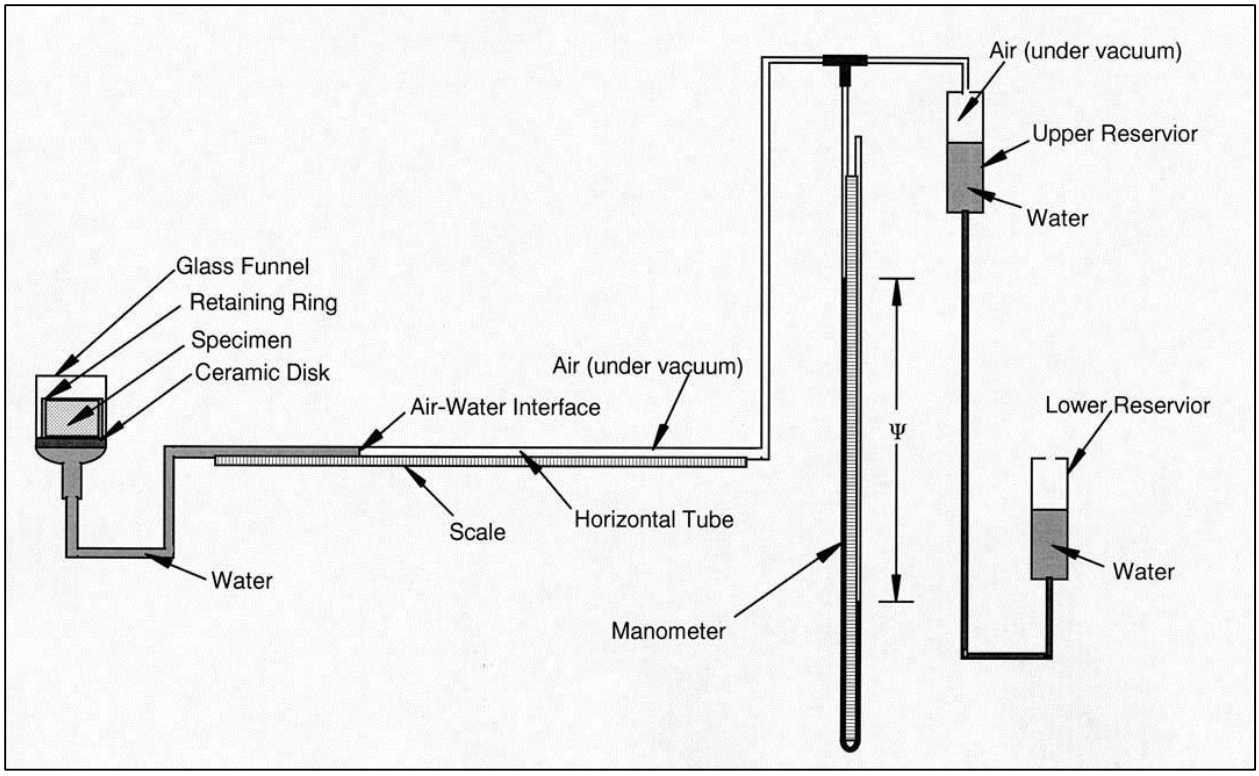

Figure 3.5 Haning Column Setup(ASTM D6836 2008)

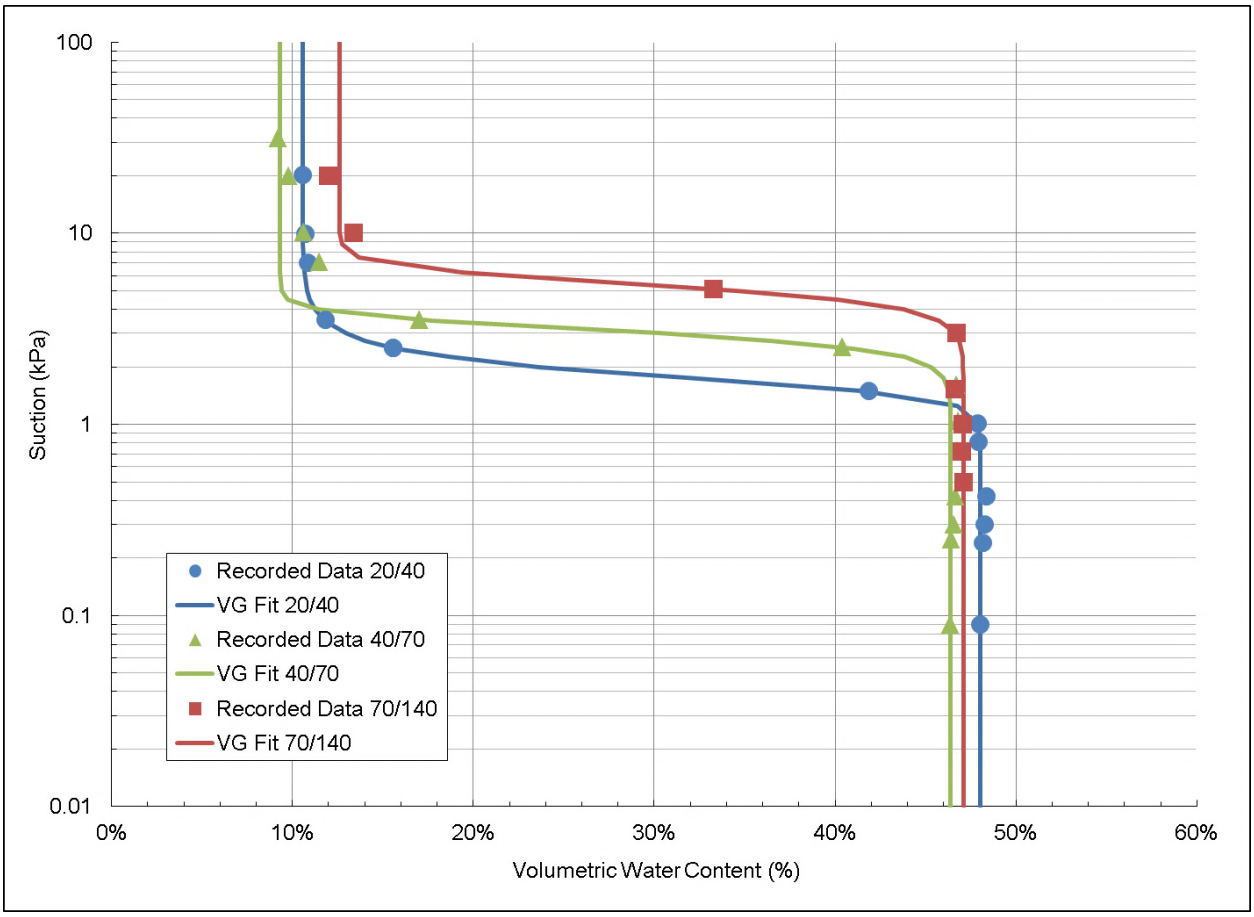

Figure 3.6 Soil Water Characteristic Curves for Frac Sand Samples.

Table 3.2 van Genuchten (1980) Soil Water Characteristic Curve Fitting Parameters for Frac Sand.

Parameters	20/40	40/70	70/140
Residual Water Content (θ_r)	0.11	0.09	0.12
Saturated Water Content (θ_s)	0.48	0.46	0.47
α (kPa^{-1})	0.63	0.29	0.19
n	10.5	7.80	6.7
m	0.41	1.89	0.81

3.2. Ballast

3.2.1. Particle-Size Distribution

Particle-size distribution for the ballast was performed using ASTM D6913. The results are shown below in Figure 3.7. The AREMA classification names were obtained by the method described in Section 2.2.2. Three ballast samples were obtained to study changes in ballast deformation from variation mineralogy and particle-size distribution.

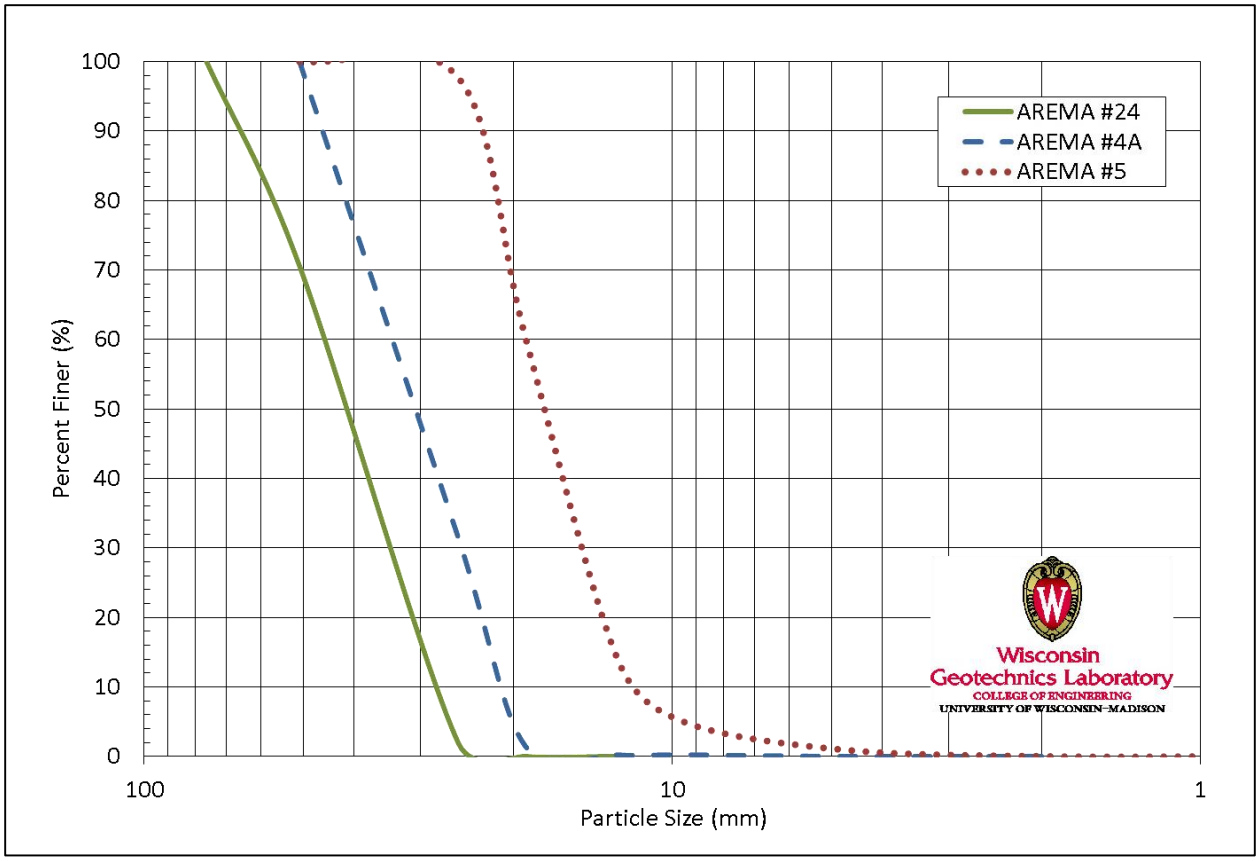

Figure 3.7 Particle-Size Distribution for Ballast Samples.

Table 3.3 AREMA Ballast Specifications (AREMA 2010).

Sieve No.	Sieve Opening	Arema #24	Arema #4A	Arema #5
	(mm)	(%)	(%)	(%)
3"	76.2	100		
2 1/2"	63.5	90-100	100	
2"	50.8		90-100	
1 1/2"	38.1	25-60	60-90	100
1"	25.4		10-35	90-100
3/4"	19.0	0-10	0-10	40-75
1/2"	12.7	0-5		15-35
3/8"	9.52		0-3	0-15
No. 4	4.75			0-5
No. 8	2.36			

3.2.2. AREMA Classification

Classification of railroad ballast in the United States is primarily determined through specifications prepared by AREMA (2010). The gradations for the ballast are listed in Table 3.3.

3.2.3. Mineralogy

The mineralogy of the ballast samples was determined by thin-section analysis. The AREMA #4A and AREMA #5 (Figure 3.8) samples were obtained from Vulcan Materials near Kankakee, IL. These two samples are primarily composed of dolomite, though one AREMA #5 thin section contained some quartz crystals. The AREMA #24 (Figure 3.9) is a metaigneous sample that contains mostly plagioclase and amphibole with small amounts of pyroxene, chlorite, and biotite.

3.2.4. Particle Shape

The ballast shape characteristics are shown in Figure 3.10. Ballast particle shape has been noted to have potential affects before and after tamping of railway ballast Tutumluer et al. (2006) and are included in this study for potential use during the maintenance modeling and life cycle analysis of this study. The ballast used in this study has sphericity in the mid-range and low roundness. As discussed in Section 2.3.1.2 higher sphericity increases stiffness while roughness and angularity increase high-strain strength for soil particles (Santamarina and Cho 2004). The ballast samples obtained for this study have similar sphericity and roundness and thus the likely properties that will determine behavior under cyclic loading are particle-size gradation, density (void ratio), and mineralogy.

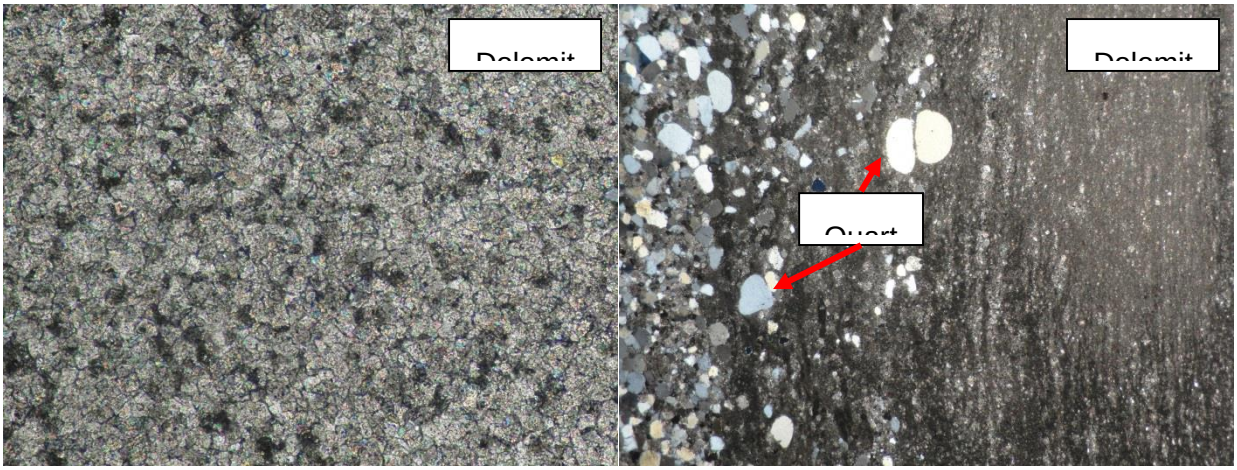

Figure 3.8 AREMA #5 thin-section analysis images.

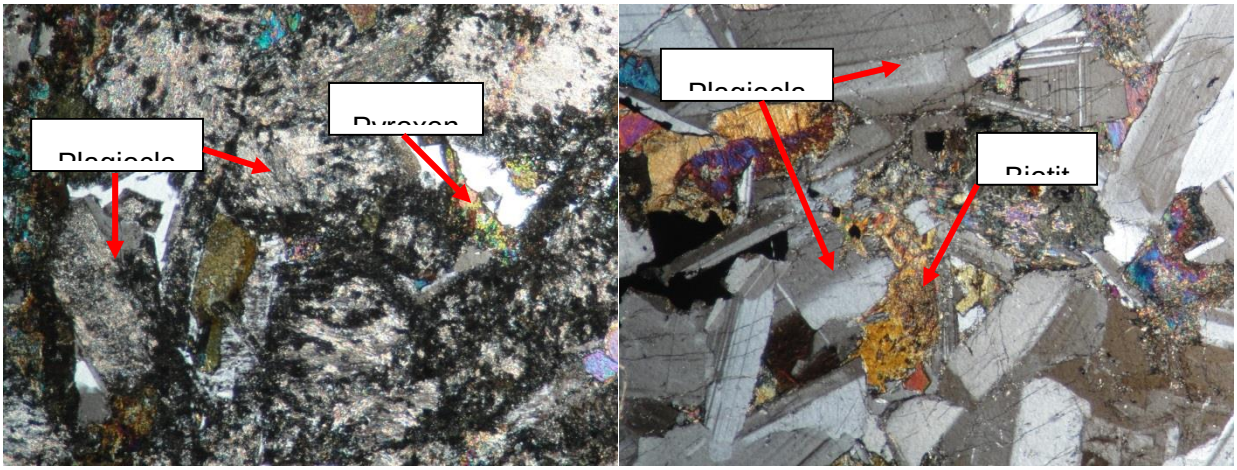

Figure 3.9 AREMA #24 thin-section analysis images.

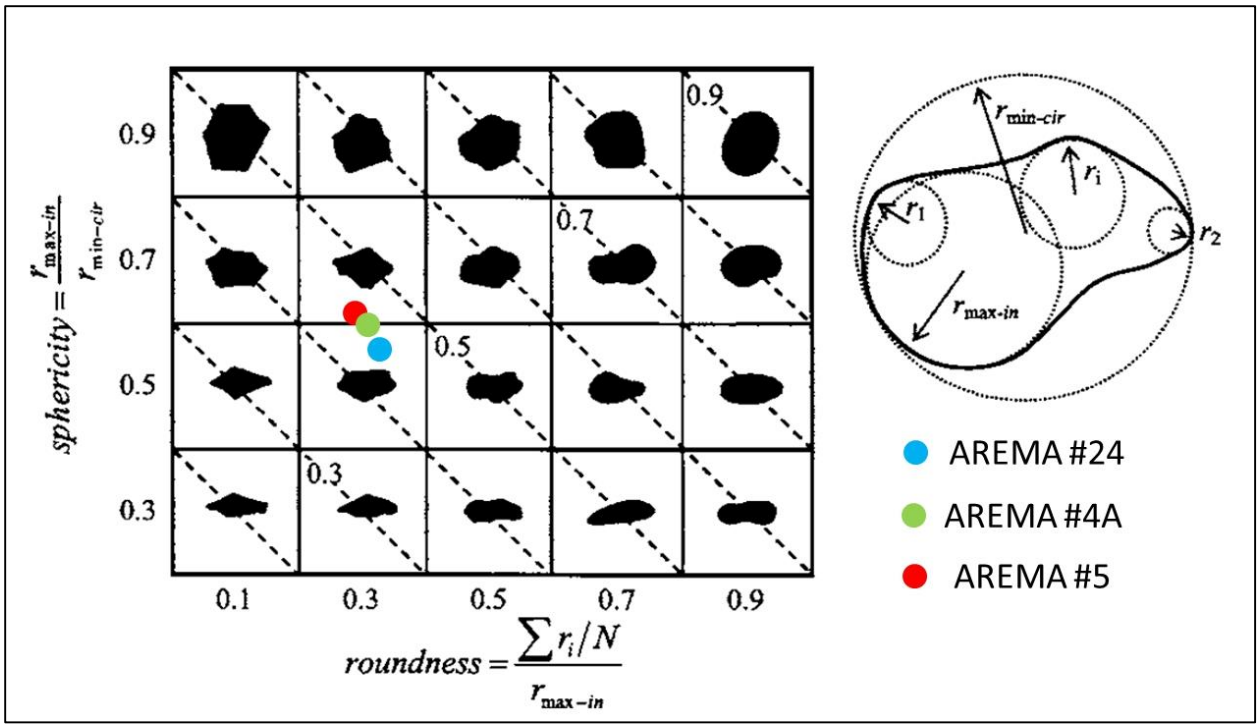

Figure 3.10 Ballast Shape Characteristics(Cho et al. 2006).

3.2.5. Density and Void Ratio

Bulk density and bulk void content were calculated in accordance with (ASTM C29/C29M 2013). Specific gravity of the ballast specimen was calculated in accordance with (ASTM C127 2012). Table 3.4 summarizes the dry density, void ratio, particle regularity, and common parameters obtained from material characterization.

Table 3.4 Summary of Ballast Properties Calculated from ASTM standard C29 [2] Calculated from ASTM standard C127 [3] Calculated from the grain size distribution curves, ASTM D6913.

Parameters	AREAM #24	AREMA #4A	AREMA #5
Bulk Density[1] (kg/m^3)	1623	1487	1537
Bulk Void Content[1] (e_B) (%)	44.2	42.9	38.2
Specific Gravity[2]	2.91	2.61	2.49
Average Grain Size[3] (mm)	40.5	30.5	18.0
Standard Deviation[3] (mm)	8.5	9.0	4.5
Maximum Size[3] (mm)	78.0	51.0	28.0
Minimum Size[3] (mm)	19.0	5.0	2.0
Coefficient of Uniformity[3] (C_u)	1.6	1.5	1.6
Coefficient of Curvature[3] (C_c)	0.9	0.9	1.0
Shape Regularity	0.43	0.44	0.44

Chapter 4: Large-Scale Cyclic Triaxial (LSCT)

Testing Methods and Procedures

4.1. LSCT – Overview

The large-scale cyclic triaxial (LSCT) apparatus is shown in Figure 0.1 and is the method used for assessing the plastic strain for ballast under cyclic loading conditions. This study utilized the test cell developed by Ebrahimi (2011), with a few modifications for additional sensors and data acquisition. Three vertical displacement measurements were taken at one third sample height increments for every test. These measurements were used to calculate the plastic strain at each respective interval. The final strain, as well as the rate of plastic strain throughout the test, is important for comparing ballast and frac sand combinations, and for development of the WiscRail™ model for predicting maintenance cycles. A pressure transducer monitored the confining pressure on the specimen during testing. The actuator that applied the desired load was fitted with a load cell to record the applied deviator stress.

The following sections describe the testing matrix and procedures that were followed during LSCT testing. A number of methods described have been adapted or mirrored from previous work on plastic strain testing of railway ballast (Keene 2012; Ebrahimi 2011; Selig and Waters 1994; Suiker et al. 2005; Lim 2004).

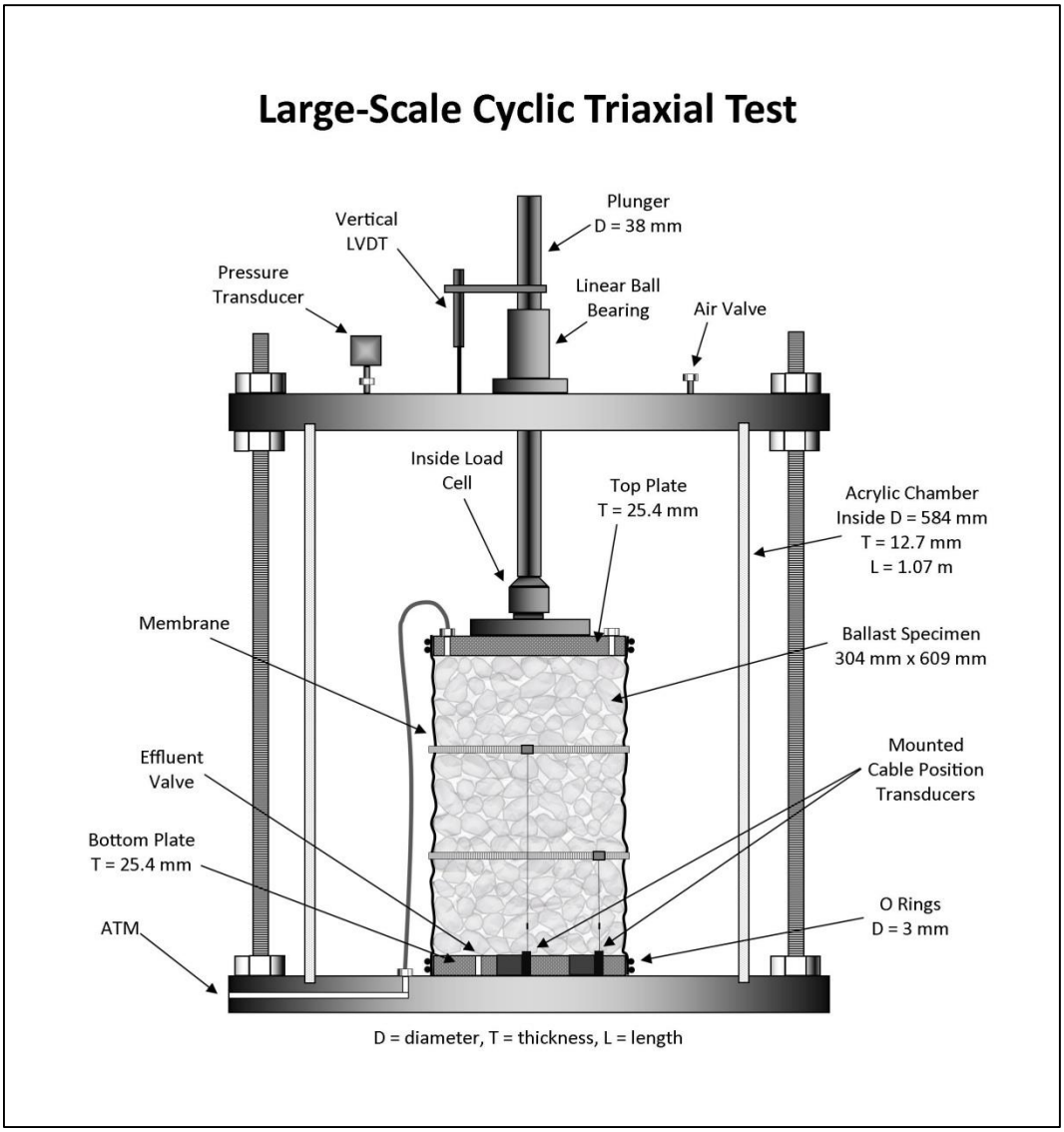

Figure 0.1 Large-Scale Cyclic Triaxial (LSCT) Setup Diagram.

4.2. Testing Matrix

4.2.1. Water Content Considerations

Previous large scale cyclic triaxial testing has been conducted at a number of gravimetric water contents on mineral, clay, and coal fouling material (Ebrahimi 2011). For frac sand, the soil-water characteristic curves show a dramatic decrease in water content over a small change in matric suction. This indicates that the soil is most likely going to be at residual saturation (w = 4) while only fully saturated (w = 17.4) in very limited time intervals. The sharp drop in water content allows for an elimination of water contents that need to be tested. For this reason, residual saturation (w = 4) was selected as well as slightly under full saturation (w = 14). Due to the high hydraulic conductivity of all the frac sand gradations, the frac sand is not likely to be fully saturated for 200,000 cycles; however, fine-grained fouling accumulation in the subballast or lower ballast layer may result in a stratified moisture layer in the frac sand. This likely heterogeneity in the ballast-frac sand moisture was accounted for with extra strain sensors, the details of which are in Section 4.1.5.

4.2.2. Fouling Content Considerations

The three gradations of frac sand are not typically seen in ballast fouling as the main fouling components, due to high amounts of fouling content resulting in ballast breakage and underlying granular layers moving up through the ballast (Zarembski 1993). However, due to the increase in hydraulic fracturing technique, the amount of frac sand being hauled over the rail network is increasing and could become a main fouling source in areas of high frac sand transport.

The key properties of frac sand are presented in Section 3 and include: hydraulic conductivity, soil-water characteristic curves, shape parameters, grain-size distribution, and minimum and maximum density and void ratio. These properties lead to the determination that the shape and durability of the grains could cause excess ballast breakage if it gets in between the ballast contact points or if the ballast voids are full and the confinement of the sand grains causes the ballast matrix to begin to separate during loading, losing strength and stiffness. For these reasons, samples without frac sand, with partial voids filled, and with full voids filled with frac sand were evaluated. Fouling indexes (FI) of 0, 15, and 30, were used in this study.

$$FI = P_4 + P_{200} \qquad \text{Eqn. 4-1.}$$

where P_4 = Percent passing the 4.75 mm (No. 4) sieve and P_{200} = Percent passing the 0.075 mm (No. 200) sieve.

The fouling index, Equation 4-1, from Selig and Waters (1994) is used to assess the percentage passing by weight for Sieve #4 and #200 of the ballast and fouling material after each test. Sieve #200 is counted twice due to the adverse effects of silts and clays. Table 0.1 shows the general ranges for fouling categories (Selig and Waters 1994).

Table 0.1 Fouling Index Ranges (Selig and Waters 1994).

Table 7.2 Fouling Index	
Category	F_I
Clean	< 1
Moderately clean	1 to < 10
Moderately fouled	10 to < 20
Fouled	20 to < 40
Highly fouled	≥ 40

4.2.3. Heavy Axle Considerations

Most Class I railroads have main lines capable of handling 286,000-lb. car loads. Some of the routes owned and operated by Class I's, however, are restricted to running 263,000 lb. or lower. Few lines are currently capable of handling 315,000 lb loads, though many Class I's have plans to increase their capacity (Zarembski 2000a). Frac sand is denser than most products being hauled currently by rail and with the constant demand for increased capacity across all freight rail lines it was important to take the future HAL increases into consideration. Selected loads, as determined in Section 2.1.2.1., for the heavy axle distribution are: 250 kPa, 350 kPa, 400 kPa, and 450 kPa.

4.2.4. Complete Desired Matrix

The final testing matrix is summarized in Table 0.2, Table 0.3, Table 0.4, and Table 0.5. This testing matrix was chosen to have clean ballast (FI = 0, w = 0) as the control specimen for each gradation (Table 0.2). LSCT tests were run at σ_d = 300 kPa and σ_c = 90 kPa. This was the baseline as previous research by Ebrahimi (2011) showed that non-cohesive fouling material and moisture content increases the plastic strain under cyclic loading.

Table 0.3 and Table 0.4 show the desired tests to run with FI = 15 and 30 and w = 4 and 14. These tests were conducted at σ_d = 300 kPa and σ_c = 90 kPa as well. These tests quantify the overall plastic strain and the rate of plastic strain accumulation for frac sand fouled ballast.

The final table (Table 0.5) has been selected from the stress-distribution calculations to quantify the effect of HAL on frac sand fouled ballast, specifically the

AREMA #24 gradation. AREMA #24 is a very common ballast gradation in the rail industry.

Table 0.2 Testing matrix for clean ballast.

FI = 0, Water Content = 0			
	AREMA #24	AREMA #4A	AREMA #5
N/A	1	1	1

Table 0.3 Testing matrix for frac sand fouled (FI = 15) ballast.

FI = 30, Water Content = 4, 14			
	AREMA #24	AREMA #4A	AREMA #5
20/40	2	2	2
40/70	2	2	2
70/140	2	2	2

Table 0.4 Testing matrix for frac sand fouled (FI = 30) ballast.

FI = 15, Water Content = 4, 14			
	AREMA #24	AREMA #4A	AREMA #5
20/40	2	2	2
40/70	2	2	2
70/140	2	2	2

Table 0.5 Testing Matrix for frac sand fouled (FI = 30) ballast at HAL.

AREMA #24			
	FI = 0, w = 0	FI = 30, w = 4	FI = 30, w = 14
250 kPa	1	1	1
350 kPa	1	1	1
400 kPa	1	1	1
450 kPa	1	1	1

4.3. Load, Pulse Shape, and Frequency

The pulse time was calculated based on the average distance between the axles of typical hopper and gondola cars, which are typically used for frac sand transport, and the average train speed. The minimum axle spacing used for the calculation was 1.8 m and the maximum axle spacing was 11.8 m. The maximum allowable train speed for Wisconsin is shown in Figure 0.3. The average frequency was calculated to be 4.6 Hz, 7.3 Hz, and 11 Hz for speeds at 40 km/hr (25 mph), 64 km/hr (40 mph), and 97 km/hr (60 mph), respectively. These speeds were selected due to the proximity of those rail lines to the frac sand mines shown in Figure 1.3. The pulse frequency used in this study was 5 Hz, which falls in the lower end of the calculated range and allows for robust comparison to previous studies on this subject. The pulse shape used was the upper half of a sine curve, applied in 10 increments calculated along one curve, with no resting period between pulses.

4.4. Compaction Method

The compaction methods outlined in the following sources (Table 0.6) show the detail amongst various compaction methods for triaxial testing. The compaction method chosen for this study was 40 blows from a 45 N hammer with a base area of 72 cm^2. This method allowed consistent density results among successive tests with minimal particle breakage and is consistent with the recommendations provided in Ebrahimi (2011). Table 0.8 shows the range of densities and specimen heights for all tests performed.

Speed (MPH)	Speed (m/s)	A (m)	B (m)	C (m)	Axel Freq (Hz)	Between Car Freq (Hz)	Same Car Freq (Hz)	Average Freq (Hz)
10	4.5	1.7	2.5	6.9	2.63	1.79	0.65	1.9
25	11.2				6.57	4.47	1.62	4.8
40	17.9				10.52	7.15	2.59	7.7
60	26.8				15.78	10.73	3.89	11.5

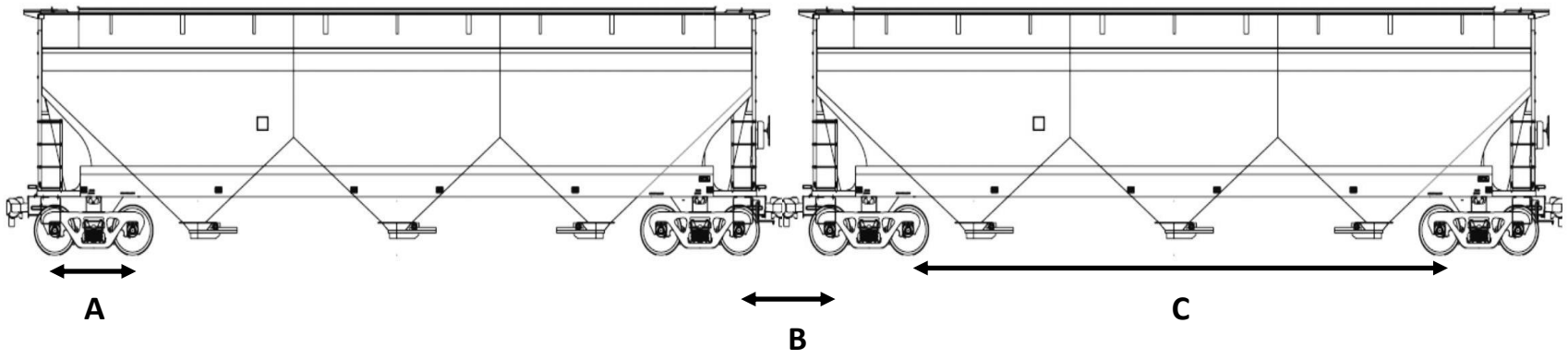

Figure 0.2 Calculation and diagram of the loading frequency. Train car specifications (American Railcar Industries, 2006)

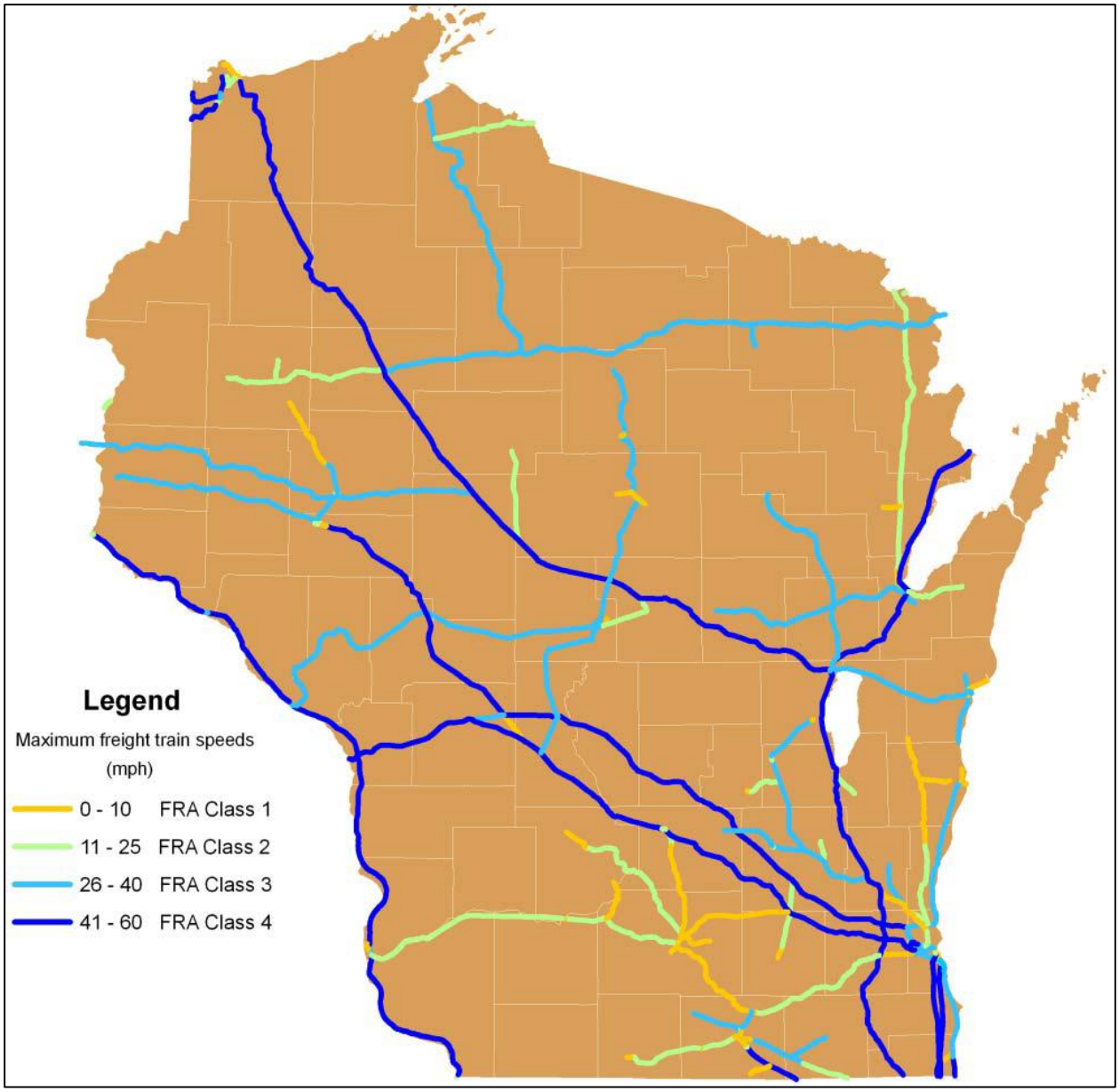

Figure 0.3 Maximum allowable train speeds on Wisconsin Railways (Wisconsin DOT 2010).

Table 0.6 LSCT test method and preparations parameters from previous studies.

Source	Method	Density (kN/m^3)	Void Ratio	Max Particle (mm)	Sample Size (mm)
Anderson and Fair (2008)	Vibratory Table Continuous Pour from 0.75 m	14.2-14.8	N/A	50	455 x 236
Ebrahimi (2011)	Vibratory Hammer and Proctor Strokes	15.8	0.62	53	609 x 309
Indraratna et al. (1998)	50 mm lifts 25 Proctor hammer	15.3	N/A	53	600 x 300
Lim et at. (2004)	Vibratory Hammer	15.9	0.70	50	450 x 700 x 300
Sevi et al. (2009)	Vibratory Table 5 lifts	15.4	N/A	63.5	889 x 419
Suiker et al. (2005)	8 lifts 40 strokes Proctor hammer	16.3-16.7	N/A	38	645 x 254

Table 0.7 LSCT test parameters from previous studies.

Source	Frequency (Hz)	Cycles	# of Membranes	Thickness (mm)
Anderson and Fair (2008)	0.16 – 0.5	100,000	2	1.5
Ebrahimi (2011)	5	200,000	4	3
Indraratna et al. (1998)	N/A	N/A	1	4.0
Lim et al. (2004)	3	1,000,000	N/A	N/A
Sevi et al. (2009)	0.05 – 3	10,000	1	0.635
Suiker et al. (2005)	5	1,000,000	1	0.76

Table 0.8 Average of initial density and range of specimen height for all tests.

	AREMA #5	AREMA #4A	AREMA #24
ASTM D4253 Density (kN/m^3)	15.1	14.6	15.9
Test Density (kN/m^3)	15.2 ± 0.5	14.5 ± 0.3	16.1 ± 0.3
Specimen Height (mm)	585-615	587-630	585-625

4.5. Membrane Preparation

For membrane preparation, a rubber material was selected with similar properties to those used in previous studies (Ebrahimi 2011; Keene 2012). The membranes were designed to have a diameter 10% less than the desired sample diameter. This is to fulfill the 10% axial stretching recommended by (Kuerbis and Vaid 1990). Membranes were then cut from a continuous sheet of rubber to roughly 914 mm wide by 670 mm tall. The excess width was folded over the other to create enough room for the seam to be glued. Use of Super glue was quick for membrane manufacturing, and resulting in a strong bond (Ebrahimi 2011). Three continuous beads of glue were used along the full length of the seam with a minimum drying time of 15 min. The last bead of glue was placed at the edge of one of the overlapping pieces. This provides a tight seal at the top and bottom plates of the specimen.

4.6. Sample Preparation

A manufactured rubber membrane was placed around the base platen, followed by a split steel mold with a diameter of 305 mm being secured around the rubber membrane and the base platen. A 610 mm x 274 mm factory-made continuous membrane was then placed inside the manufactured rubber membrane. Both membranes were secured to the top of the split steel mold with tape. The ballast was placed and compacted in approximately 5 equal lifts, according to the compaction method described above. A top platen was then placed and secured with the manufactured membrane, which was already in place. The split-steel mold was then removed and a latex manufactured membrane was placed over the entire specimen. The final rubber manufactured membrane was placed around the entire sample. That

final outer membrane was glued to the top and bottom platen with rubber cement to ensure an air tight sample. Rubber cement was used because it is non-permanent but applies correct sealing for later application of confining pressure.

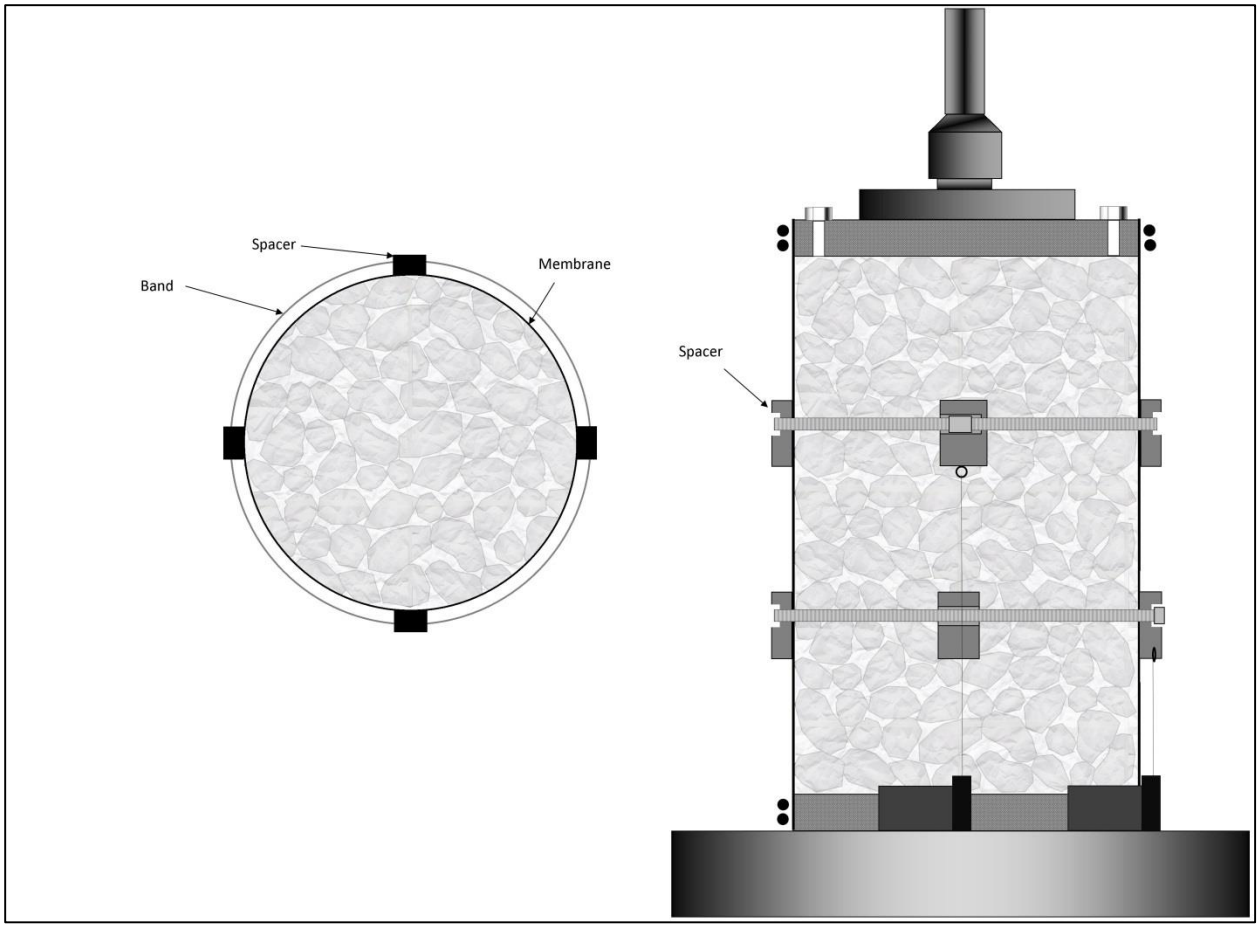

Figure 0.4 Diagram of the Band Spacers and Arangement of Cable Transducers.

Cable transducers (Unimeasure HX-PA-2-L.10, linearity = ± 0.051 mm), which measure at roughly one-third increments from the top and bottom of the sample (Figure 0.4) were connected to the sample by a 220-N-capacity wire. This wire is connected to spacers made out of solid oak blocks that have double-sided-foam tape on the membrane side to provide added adhesion to the membrane during testing. These spacers are meant to provide minimal interaction with the membrane and ballast sample while a rubber O-ring provides a snug fit. The O-ring ensures that the wood blocks are secure and will not move under the 10 N tension force of the cable transducers. This assures that the blocks, and subsequently the cable transducers, only measure the sample movement during testing and not the movement or rotation of the blocks.

4.7. Measurement Equipment

The components used to conduct these LSCT tests can be referenced in Figure 0.1. The actuator applies the desired load through the load cell to the 38-mm plunger. The load cell measures the precise load and was calibrated to within 1% of full range, which is 89 kN (20,000 pounds). The load is then transferred to the sample via the top platen that has a thickness of 25.4 mm and a diameter of 305 mm. The actuator also has an internal system for measuring displacement. However, the noise in the signal prompted the use of an external linear variable differential transformer (LVDT) for total strain measurement. The vertical LVDT was mounted to the plunger outside the acrylic chamber and is an Omega LD621-20 (linearity = ± 0.04 mm). The pressure chamber in which the ballast sample sits is made of an acrylic cylinder with metal top and bottom plates. This chamber is secured with six steel rods around its outer circumference. The top plate has four connection points for the following equipment: pressure transducer for

measuring the applied confining air pressure, a 310-kPa safety release valve, wire connectors for the internal cable position transducers, and a gauge for comparing the measured pressure from the transducer. The bottom plate has a connection for the air pressure regulator that allows for adjustment of air into the acrylic cylinder. There is also a port that is connected to the top platen of the sample and is vented to the atmosphere. This is to monitor the air tightness of the outer membrane of the specimen. The two internal cable position transducers each monitor the sample at different places in order to account for differences in plastic strain throughout. Cable transducer #1 measures roughly at the top third of the sample and cable transducer #2 measures roughly at the bottom third of the sample.

A LabVIEW program was developed to both control the actuator and record the necessary data in real time for the desired number of cycles and stress parameters. The actuator is controlled by calculating the upper half of a sine curve at the desired stresses. This sine curve is then repeated at a frequency of 5 Hz. At both resting stress and peak deviator stress the program records and writes to a file the following data: cycle number, peak or trough indication, actuator displacement, applied load, applied confining pressure, LVDT position, cable transducer #1 & #2 position. The plastic strain is calculated by knowing the initial specimen height, the resting readings of the LVDT and both cable transducers compared to the starting position of each of these three measurement devices at the beginning of the test. The following two equations outline how to calculate the strains from the peak and resting load readings.

Elastic Strain, ε_e = (LVDT, CT #1, or CT #2 reading at current maximum peak load) / (LVDT, CT #1, or CT #2 reading at first cycle maximum peak load)

Plastic Strain, ε_p = (LVDT, CT #1, or CT #2 reading at current resting load)/(LVDT, CT #1, or CT #2 reading at first cycle resting load

4.8. Repeatability Tests

For any test method, repeatability is a key issue; to strengthen the results of this study a selection of three test points were conducted in duplicate. These repeated tests are in (Figure 0.5, Figure 0.6, and Figure 0.7) and were conducted according to the same methods used for all samples as described in Section 4.2. The results show that, for the same sample parameters, there are similar rates of plastic strain in the ICP and FIP with some variation. The variation of plastic strain could be due to variations in density of the ballast after compaction, which is detailed in Section 2.3.1.5, or distribution of moisture in the sample, which is detailed in Section 2.3.3. The ballast density variation for each ballast type is shown in Table 0.8. Though the mean for each type matches the initial density tests ASTM D4253 (2006), the standard deviation from test to test may explain the ICP variation in rate of plastic strain. The two samples in Figure 0.5 show this initial difference in rate of plastic strain during the ICP and a convergence of strain rate during the FIP. However, the samples in Figure 0.6 and Figure 0.7 show a similar rate of plastic strain during ICP and a divergence in the FIP.

The results of these repeat tests showed that there is some variation in the rate of plastic strain for both the ICP and the FIP for each sample. This change in rate of plastic strain could be explained by variations in sample densities or moisture content. The result of these repeated tests does show that there is repeatability for this preparation and test method though more repeat tests will need to be performed to reduce the uncertainty and variability in these tests.

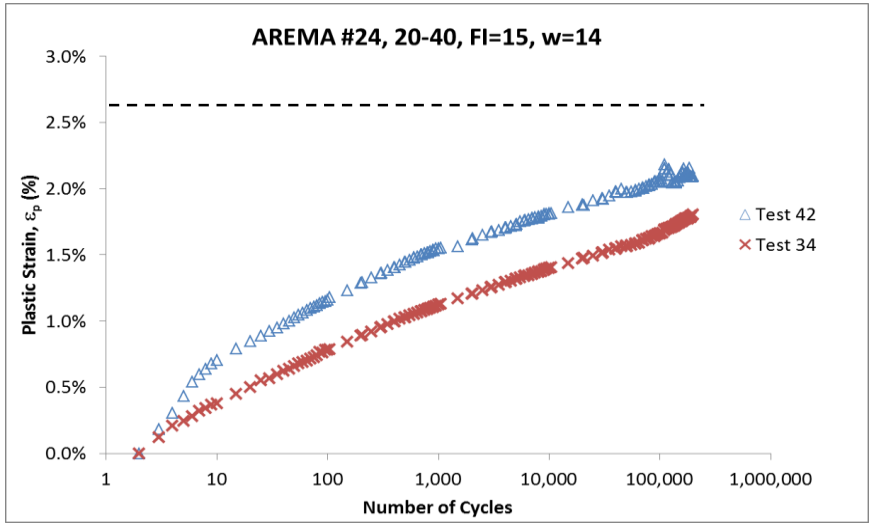

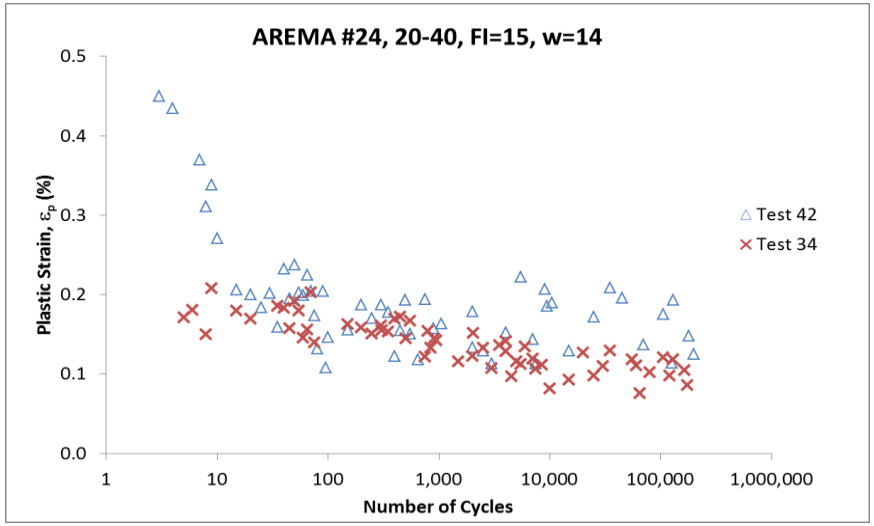

Figure 0.5 Accumulation of plastic strain and rate of plastic strain for repeated tests #42 & #34, under 2 x 10^5 loading cycles.

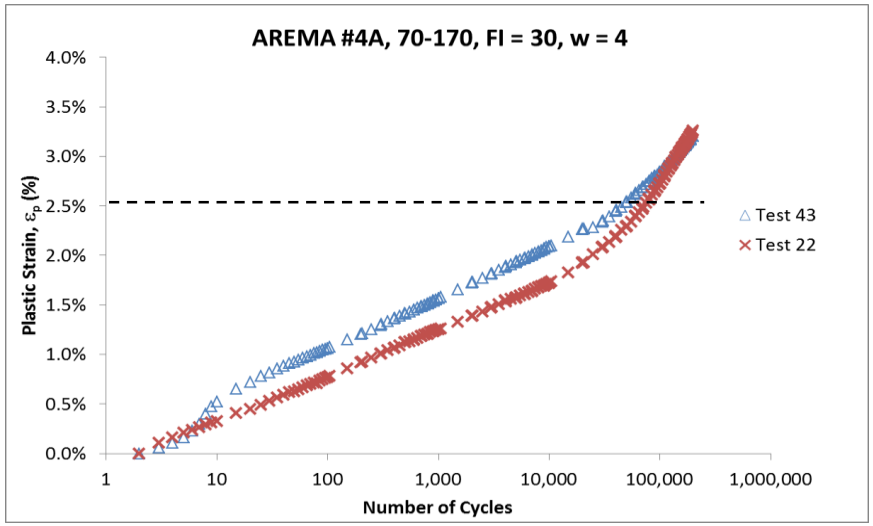

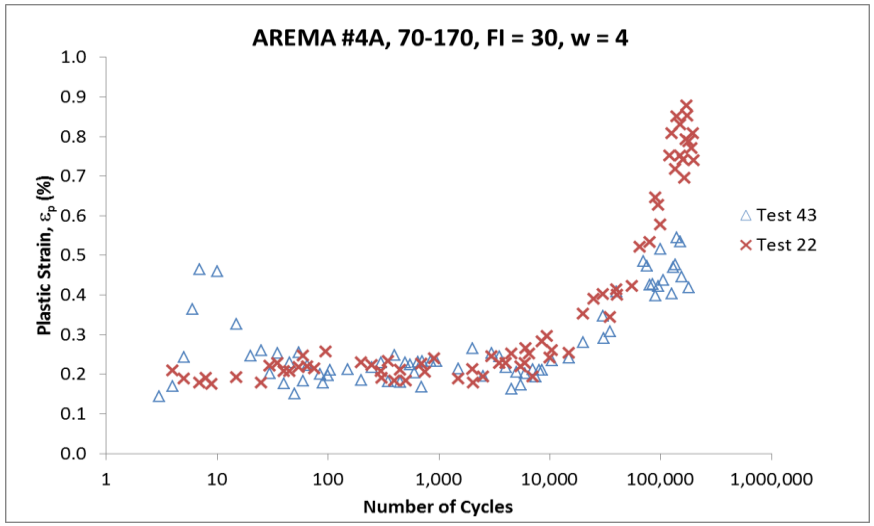

Figure 0.6 Accumulation of plastic strain and rate of plastic strain for repeated tests #43 & #22, under 2 x 10^5 loading cycles.

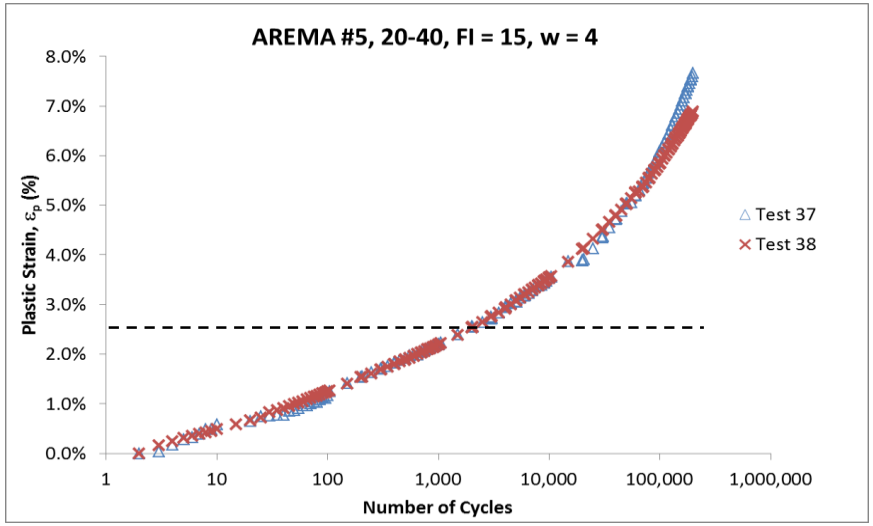

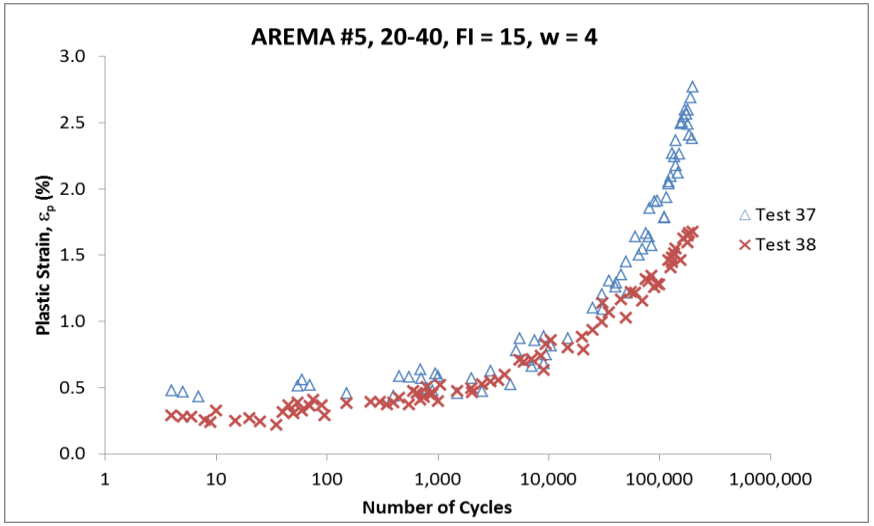

Figure 0.7 Accumulation of plastic strain and rate of plastic strain for repeated tests #37 & #38, under 2 x 10^5 loading cycles.

Chapter 5: Results

5.1. LSCT Results

Large-scale cyclic triaxial (LSCT) tests were performed according to the methods described in Section 4. This section presents the results of this study. Later in this thesis, deformation data will be used as input to the WiscRail™ model for predictive maintenance. The dashed black horizontal line in the following graphs is the plastic strain limit allowed by the FRA (2011) for class 5 track before maintenance is recommended. The ballast is assumed to contribute 40% of the deformation for the total 25-mm track deformation limit. Accompanying the total plastic strain is the rate of plastic strain graphs, which were calculated using Eq. 5-1.

$$r_p = \frac{d\varepsilon_p}{lnN}. \qquad \text{Eqn. 5-1}$$

The specimens show an initial compaction phase (ICP) up to 10^3 to 10^4 load cycles (N), and an fouling impact phase (FIP) afterward (Figure 5.1.14) (Ebrahimi 2011). During the ICP, the plastic strain is linear on a semilogrithmic graph with a constant rate of plastic strain (r_p). During the FIP, some of the specimens exhibit a non-linear plastic strain behavior and an increasing rate of plastic strain (r_p).

5.1.1. Water Content

Water content comparisons are shown in Figure 5.1.1 and Figure 5.1.2, for all three ballast gradations, at w = 4, 14. The AREMA #24 ballast at the two moisture contents shows less that 0.5% total plastic strain difference through 200,000 cycles. The AREMA #24 ballast also shows a constant rate of plastic strain in both the ICP and FIP (Figure 5.1.2). The AREMA #4A ballast at the two moisture contents shows more than

1% total plastic strain difference through 200,000 cycles. The AREMA #4A ballast also shows a constant rate of plastic strain in the ICP and an increasing rate of plastic strain in the FIP for both water contents. The AREMA #5 ballast at the two moisture contents shows more than 3% total plastic strain difference through 200,000 cycles. The AREMA #5 ballast also shows a constant rate of plastic strain in the ICP and an increasing rate of plastic strain in the FIP for w = 14 only (Figure 5.1.2).

These results show that the water content has a small effect for the AREMA #24 ballast and a greater effect on the AREMA #4A and AREMA #5. The means that, while moisture content is a factor in ballast deformation, there are other parameters that may be causing the difference in response in these tests. Therefore, for the same moisture content with the same fouling material, a different rate of plastic strain may be produced depending on either the type of ballast or the gradation of the ballast.

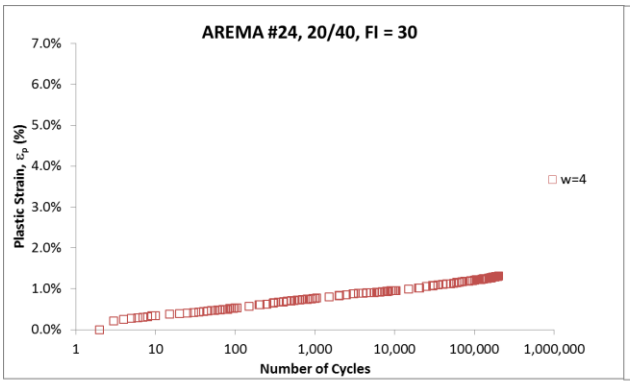
AREMA #24, 20/40, FI = 30
Plastic Strain, ε_p (%)
7.0%
6.0%
5.0%
4.0%
3.0%
2.0%
1.0%
0.0%
1
10
100
1,000
10,000
100,000
1,000,000
Number of Cycles
w=4

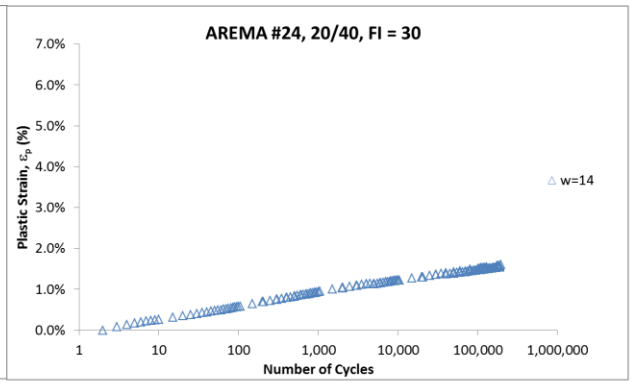
AREMA #24, 20/40, FI = 30
Plastic Strain, ε_p (%)
7.0%
6.0%
5.0%
4.0%
3.0%
2.0%
1.0%
0.0%
1
10
100
1,000
10,000
100,000
1,000,000
Number of Cycles
w=14

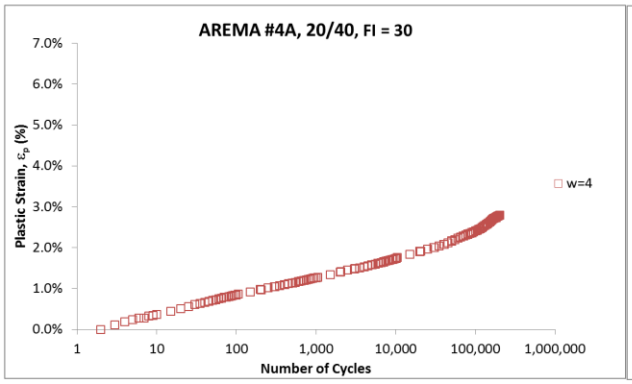
AREMA #4A, 20/40, FI = 30
Plastic Strain, ε_p (%)
7.0%
6.0%
5.0%
4.0%
3.0%
2.0%
1.0%
0.0%
1
10
100
1,000
10,000
100,000
1,000,000
Number of Cycles
w=4

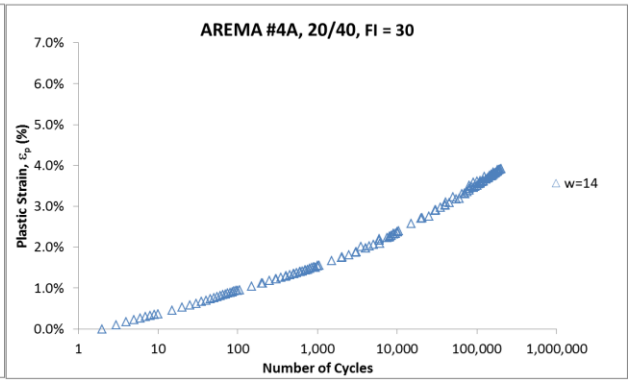
AREMA #4A, 20/40, FI = 30
Plastic Strain, ε_p (%)
7.0%
6.0%
5.0%
4.0%
3.0%
2.0%
1.0%
0.0%
1
10
100
1,000
10,000
100,000
1,000,000
Number of Cycles
w=14

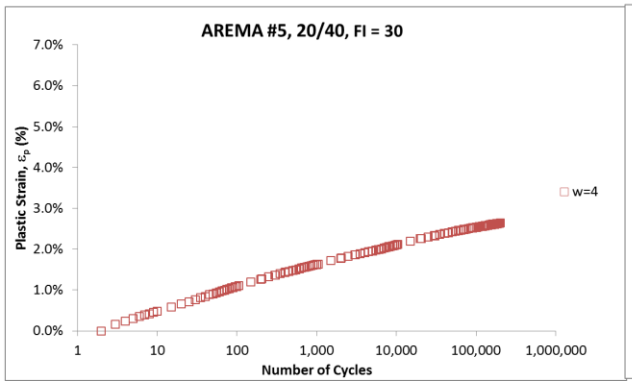
AREMA #5, 20/40, FI = 30
Plastic Strain, ε_p (%)
7.0%
6.0%
5.0%
4.0%
3.0%
2.0%
1.0%
0.0%
1
10
100
1,000
10,000
100,000
1,000,000
Number of Cycles
w=4

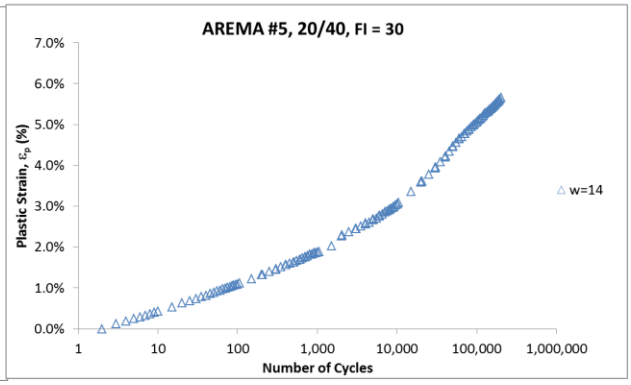
AREMA #5, 20/40, FI = 30
Plastic Strain, ε_p (%)
7.0%
6.0%
5.0%
4.0%
3.0%
2.0%
1.0%
0.0%
1
10
100
1,000
10,000
100,000
1,000,000
Number of Cycles
w=14

Figure 5.1.1 Cumulative plastic strain, comparison of water content for the same ballast and frac sand at w = 4, 14 (left to right).

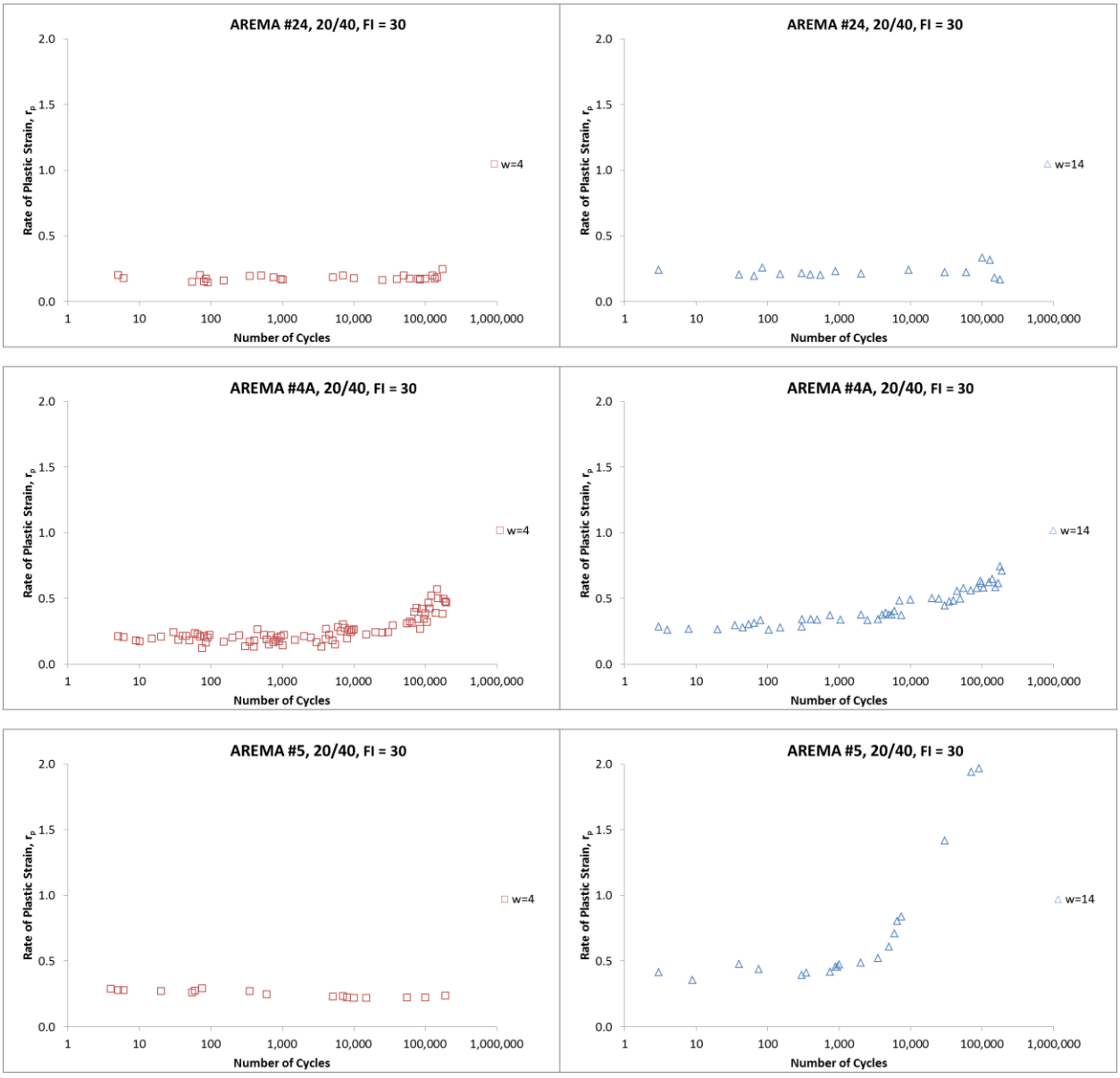

Figure 5.1.2 Rate of plastic strain, comparison of water content for the same ballast and frac sand at w = 4, 14 (left to right).

5.1.2. Ballast Type and Gradation

Ballast type and gradation comparisons are shown in Figure 5.1.3 and Figure 5.1.4, for all three ballast gradations, at w = 4, and sand gradation 40/70 and 70/140. The AREMA #24 ballast for both sand gradations shows a constant rate of plastic strain in both the ICP and FIP (Figure 5.1.4), with a relatively low total plastic strain through 200,000 cycles. The AREMA #4A ballast, for both sand gradations, shows a constant rate of plastic strain in the ICP, and an increasing rate of plastic strain in the FIP. The AREMA #5 ballast for both sand gradations also shows a constant rate of plastic strain in the ICP and an increasing rate of plastic strain in the FIP (Figure 5.1.4).

These test results show a small difference in the rate of plastic strain for AREMA #24 versus the AREMA #4A or the AREMA #5. There is also a similarity between the same ballast type, but different sand gradation (left to right) (Figure 5.1.3). This indicates that the difference in response is due to the ballast differences in gradation or mineralogy. However, when comparing AREMA #4A and AREMA #5, which have different gradations but similar mineralogy, the variation in plastic strain is small. This suggests that mineralogy of the ballast has a greater effect on the deformation behavior than the gradation. As dolomite particles would most likely have less particle strength than ingenious particles under cyclic loading, the difference in mineralogy is the most plausible explanation.

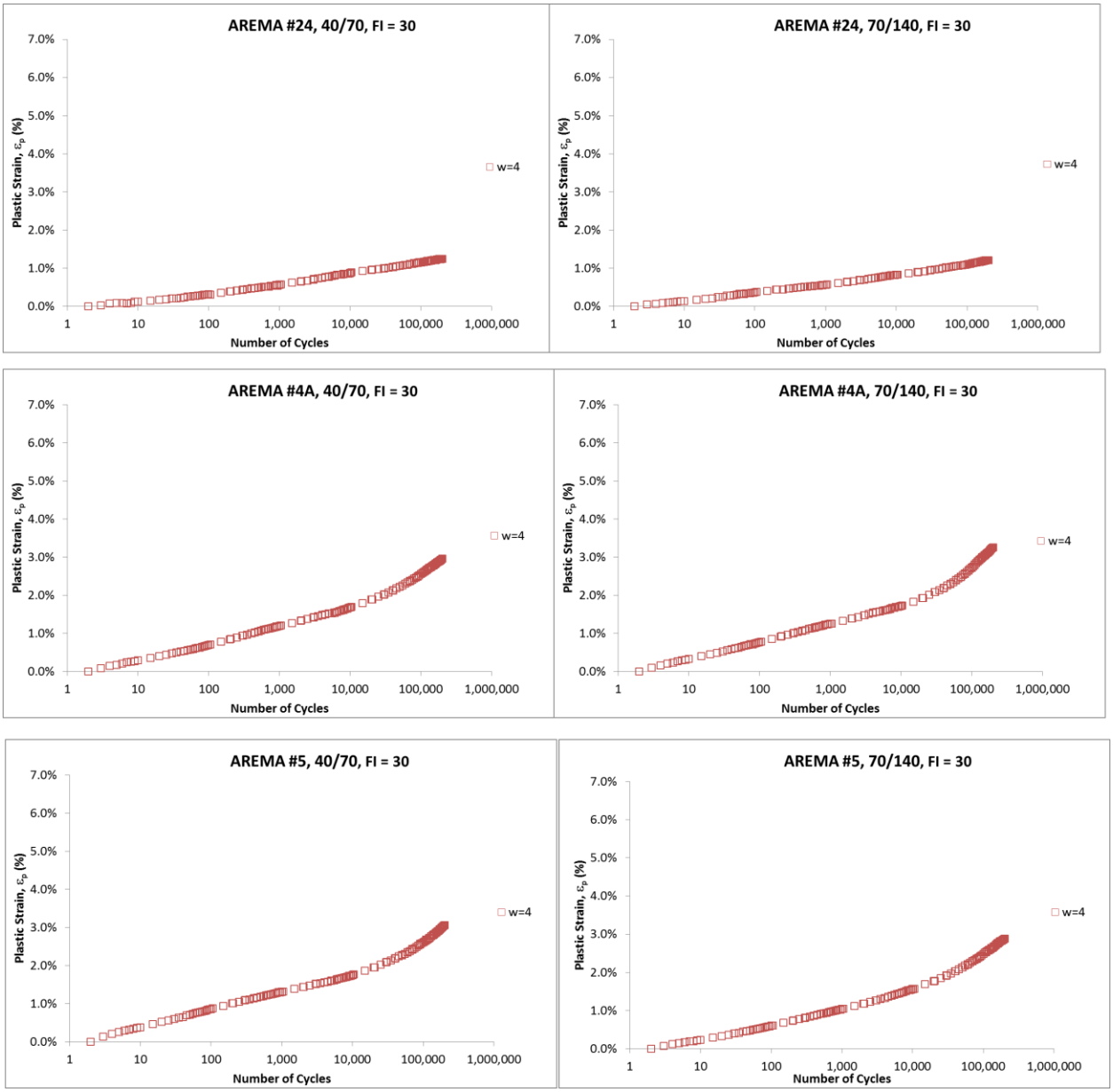

Figure 5.1.3 Cumulative plastic strain, comparison of ballast type and gradation AREMA #24 to AREMA #5 at w = 4 (top to bottom).

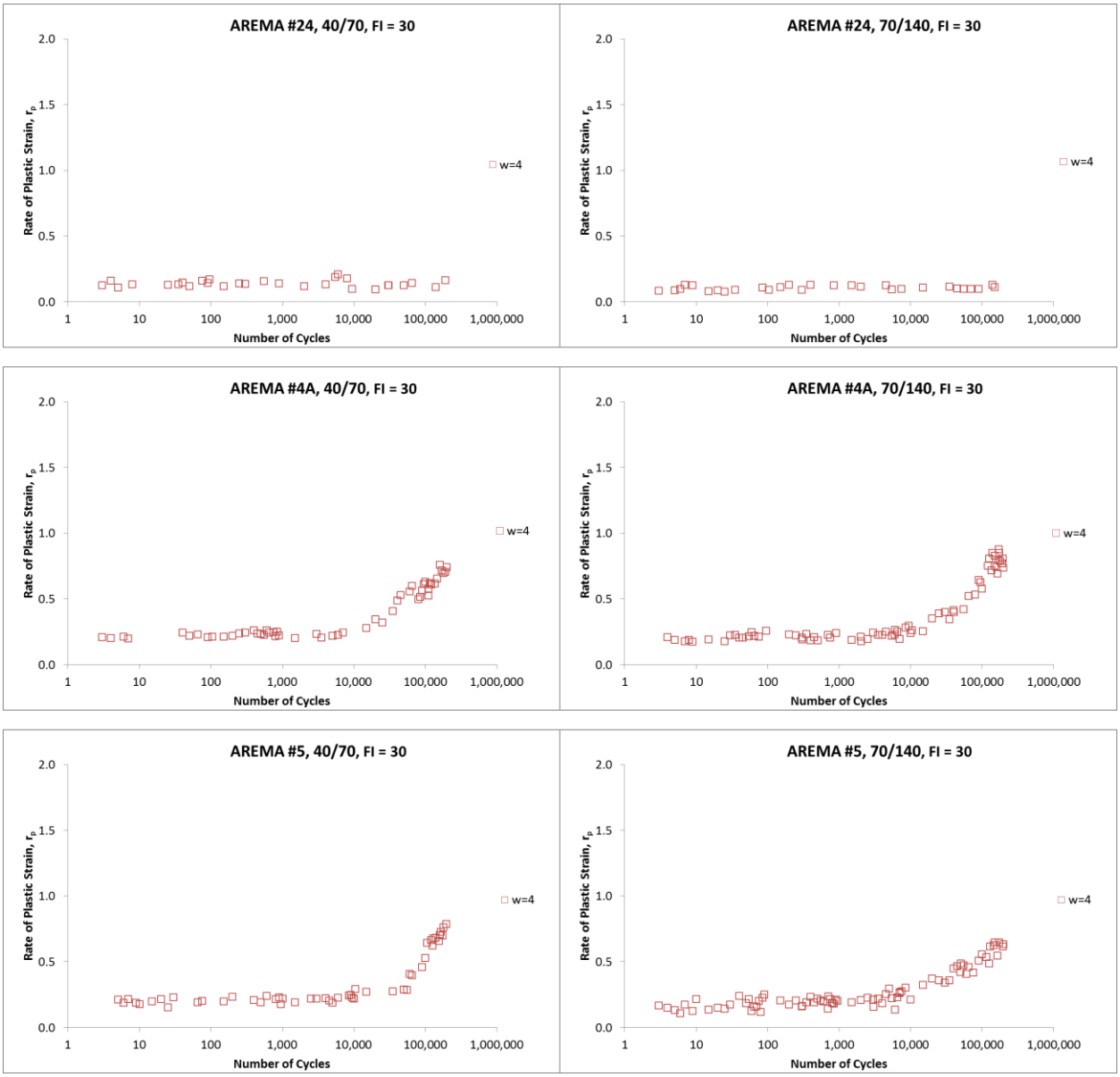

Figure 5.1.4 Rate of plastic strain, comparison of ballast type and gradation AREMA #24 to AREMA #5 at w = 4 (top to bottom).

5.1.3. Sand Gradation

Sand gradation comparisons are shown in Figure 5.1.6 and Figure 5.1.7 for AREMA #24 and AREMA #5 with all three frac sand gradations and w = 0. The variation in frac sand gradations with AREMA #24 ballast are small (1.39% to 1.58%) and shows a constant rate of plastic strain in both the ICP and FIP (Figure 5.1.7). The variation in frac sand gradations with AREMA #5 ballast are larger than AREMA #24, with a range of 4.26% to 5.67%. The frac sand gradations with AREMA #5 ballast show a constant rate of plastic strain in both the ICP with an increasing rate of plastic strain in the FIP (Figure 5.1.7).

Sand gradation had a small effect on the deformational behavior of the ballast for AREMA #24, while there was a larger variation in rate of plastic strain for AREMA #5. The variation in rate of plastic strain for AREMA #5 could be the results of similar trend between rate of plastic strain for 40/70, 70/140, and 20/40 (low to high) (Figure 5.1.7), and saturated water content for 40/70, 70/140, and 20/40 (low to high) (Figure 3.6). This means that a lower saturated water content capacity corresponds with a lower the rate of plastic strain in the FIP.

Small sample statistical methods from Dean and Dixon (1951), and ANOVA tests were conducted to determine if the gradations of frac sand showed statistically significant differences in ballast behavior. The mean and confidence interval (Figure 5.1.5) were calculated for all three sand gradations, at each water content and ballast combination (Table 5.1.1). The ANOVA tests gave the parameters F-Crit, F, and P. The low probability (P) from the ANOVA tests, as well as the large confidence intervals,

indicate that, for the number of tests conducted, there is not a significant behavioral difference between the sand gradations.

Table 5.1.1 Statistics for frac sand gradation variation.

ANOVA and Small Sample Statistics (Dean and Dixon, 1951)						
	AREMA #24, w=4	AREMA #24, w=14	AREMA #4a, w=4	AREMA #4a, w=14	AREMA #5, w=4	AREMA #5, w=14
Mean	1.61%	1.94%	3.46%	4.31%	3.31%	6.18%
95% Conf.	±1.79%	±2.05%	±3.37%	±4.23%	±3.39%	±5.22%
F-Crit	3.01	3.01	3.01	3.01	3.01	3.01
F	26.53	57.75	18.74	16.90	11.31	14.84
P	9.9 E-12	1.6 E-23	1.3 E-8	7.5 E-8	1.5 E-5	5.3 E-7

$$\bar{X} \pm t_{n-1,\propto/2} \frac{s}{\sqrt{n}}$$ Eqn. 5-2.

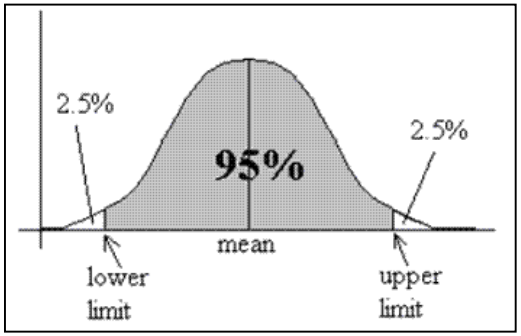

Figure 5.1.5 95% confidence interval for t-statistics testing.

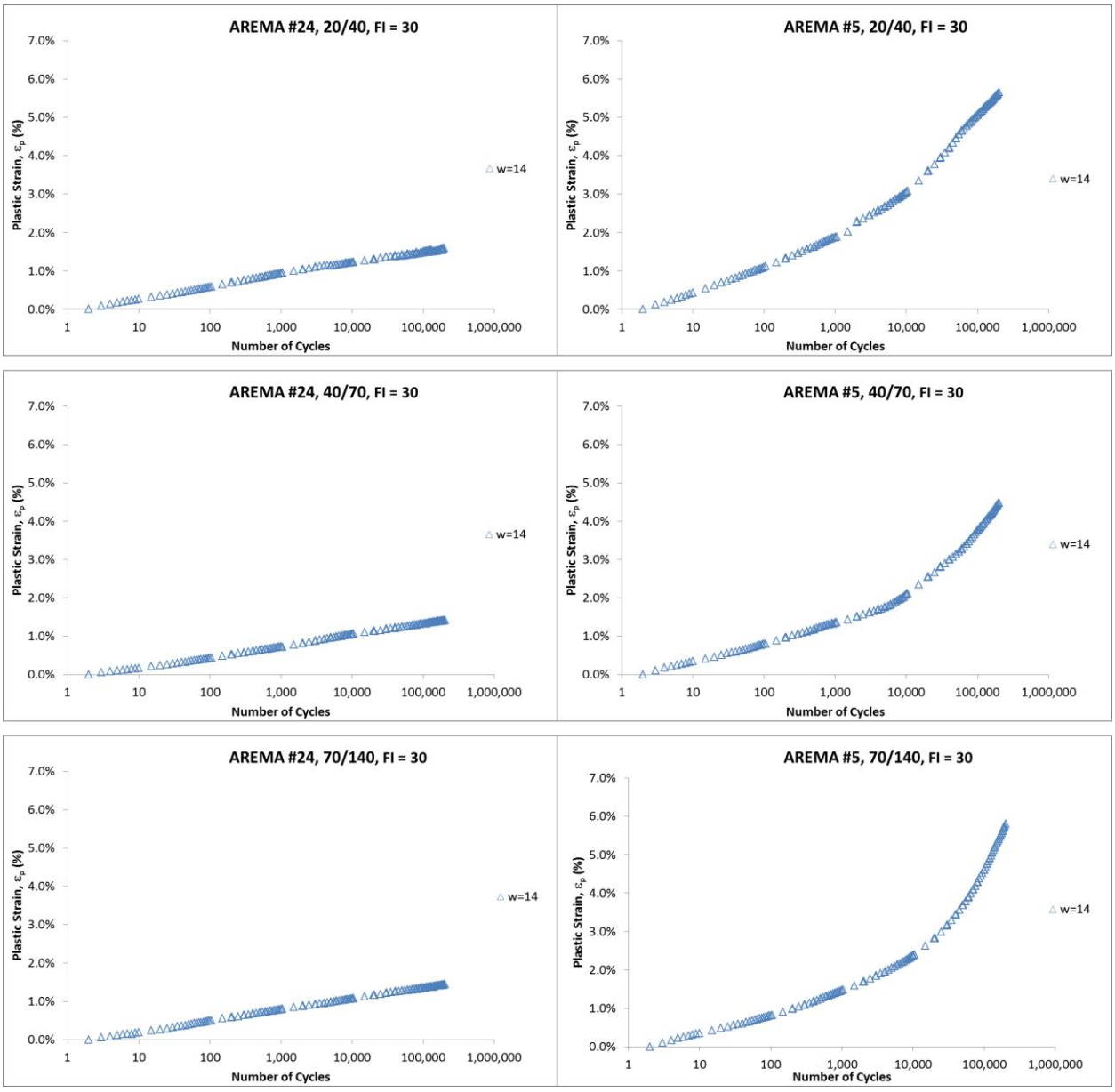

Figure 5.1.6 Cumulative plastic strain, comparison of sand gradation from 20/40 to 70/140 (top to bottom) in AREMA #24 and AREMA #5 ballast (left to right).

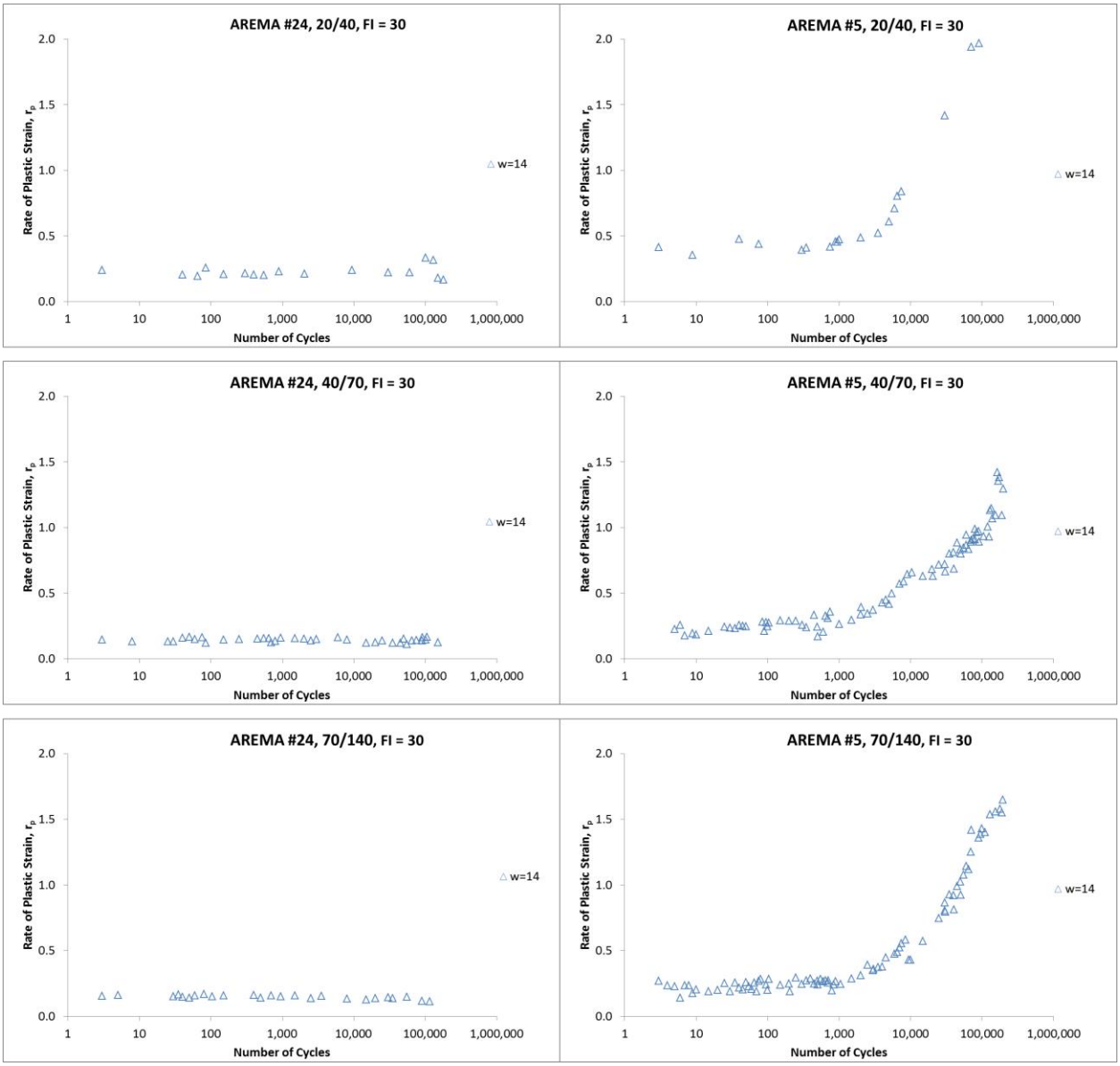

Figure 5.1.7 Rate of plastic strain, comparison of sand gradation from 20/40 to 70/140 (top to bottom) in AREMA #24 and AREMA #5 ballast (left to right).

5.1.4. Fouling Index (FI)

Fouling index comparisons are shown in Figure 5.1.8 and Figure 5.1.9, for all three ballast gradations, at the same frac sand gradation (20/40), and water content (w = 4). The AREMA #24 ballast at the two fouling contents (FI = 15, 30), shows a small variation during the FIP. The FI = 15 test shows an increase in rate of plastic strain during FIP, where the FI = 30 test shows a constant rate of plastic strain for both the ICP and FIP (Figure 5.1.9). The AREMA #4A ballast at the two fouling contents (FI = 15, 30) shows a small variation during the FIP. The FI = 30 test shows an increase in rate of plastic strain during FIP, where the FI = 15 test shows a constant rate of plastic strain for both the ICP and FIP (Figure 5.1.9). The AREMA #5 ballast at the two fouling contents (FI = 15, 30), shows a large variation during the both the ICP and FIP. The FI = 15 test shows a large increase in rate of plastic strain throughout the 200,000 cycles, where the FI = 30 test shows a constant rate of plastic strain for both the ICP and FIP (Figure 5.1.9).

The AREMA #5 behavior could be explained by the frac sand contaminating the contact points and reducing the interlocking of the ballast. This mechanism would be limited for FI = 30, because the ballast voids would be full of sand, limiting the movement of the ballast particles; whereas, for FI = 15, the sand in the voids would not restrict ballast movement, which would explain the increase in deformational behavior. However, this is contradicted by the results for AREMA #24 and AREMA #4A at FI = 15. More tests should be run for FI = 15 to verify that the behavior matches the mechanisms suspected to control the deformation. If further tests indicate that there is no significant difference between FI = 15 and FI = 30, then the restriction of ballast movement based

on the amount of fouling content present is not a valid explanation and the AREMA #5 test may be an outlier.

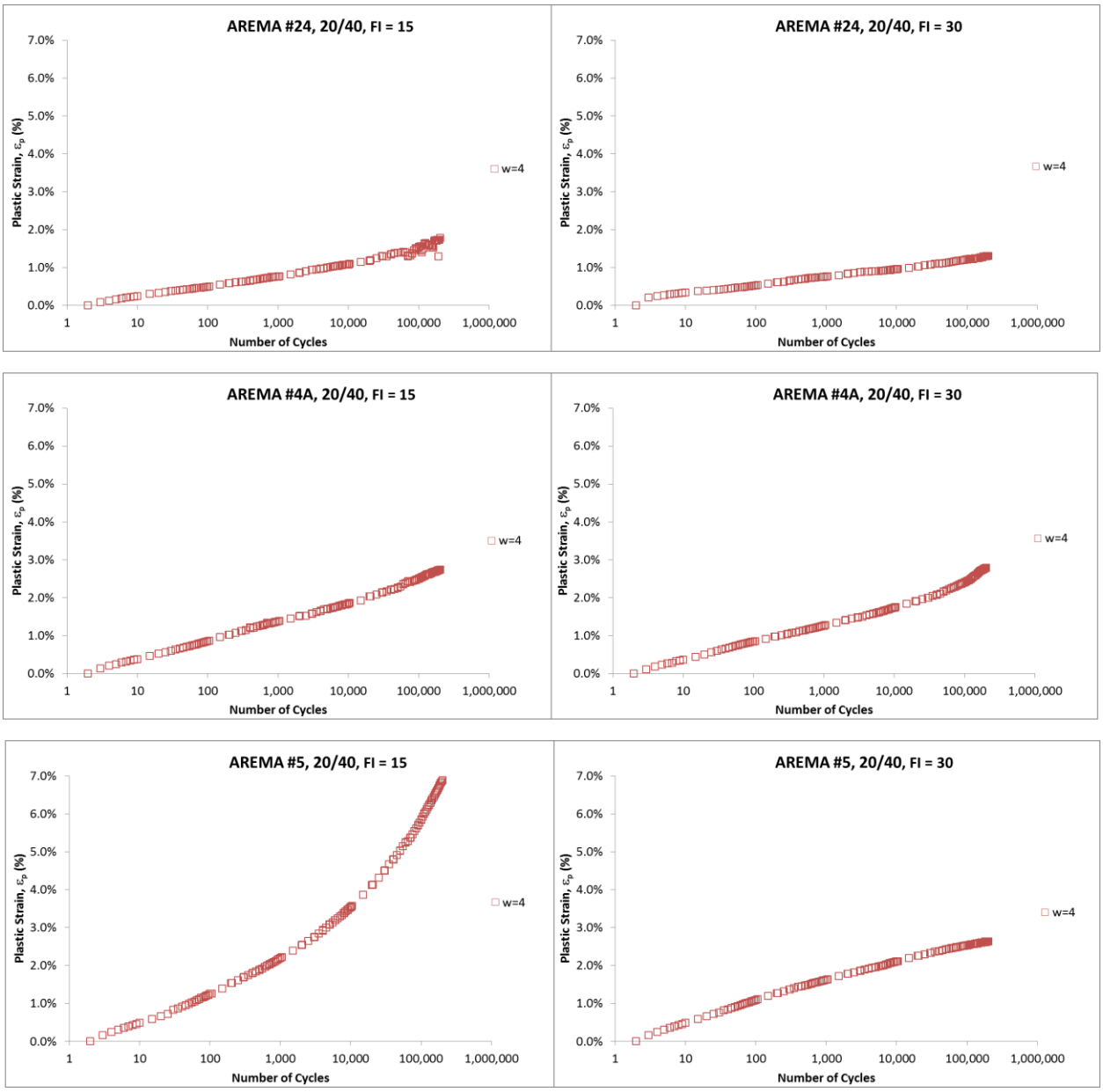

Figure 5.1.8 Cumulative plastic strain, comparison of Fouling Index, FI = 15, 30 (left to right) for AREMA #24 to AREMA #5 (top to bottom).

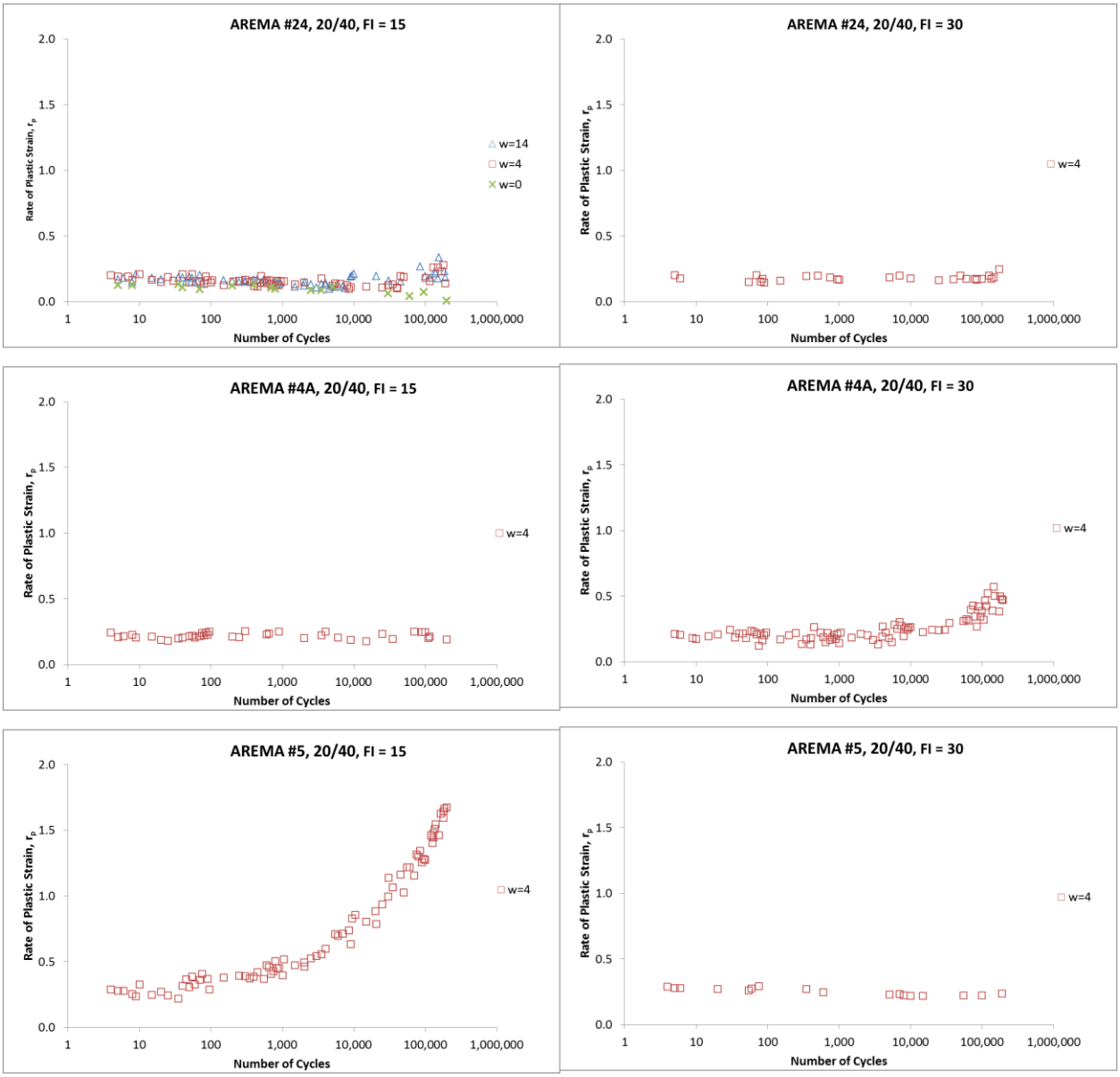

Figure 5.1.9 Rate of plastic strain, comparison of Fouling Index, FI = 15, 30 (left to right) for AREMA #24 to AREMA #5 (top to bottom).

5.1.5. HAL tests (σ_d = 250 kPa, 300 kPa, 350 kPa, 400 kPa, & 450 kPa)

HAL tests were conducted for AREMA #24 ballast at five deviatoric stress levels (Figure 5.1.10). The confining pressure (90 kPa) was kept constant for each of the tests. The loadings used are outlined in Section 2.1.2.1 and were applied to the samples prepared under the same conditions and using the same apparatus as the tests run at 300 kPa deviator stress. For clean ballast the behavior is similar across all deviator stress levels with the ICP being linear and the FIP being linear, but with a lower rate of plastic strain. For the w = 4, FI = 30, tests the rate of plastic strain appears to be relatively constant throughout the test with no indication of a transition from ICP to FIP across all the stress levels. When comparing the same deviator stress, the difference in final plastic strain is on average 0.6 % more for the FI = 30, w = 4 compared to clean ballast. At w = 14 and FI = 30, the test show results similar to the others with higher deviator stresses causing increased deformation. Though the average difference of final plastic strain for fresh versus fouled ballast is small (0.6%), the behavior characteristics are significantly different for clean versus frac sand and moisture fouled ballast, particularly the rate of plastic strain increase in the FIP.

The HAL tests indicate that increasing the load results in an increase in total plastic strain as well as, an increase in the rate of plastic strain. The increase in total plastic strain for a 50 kPa deviator stress increase is similar to the increase in total plastic strain for adding fouling (FI = 30) and moisture (w = 4), an average of 0.5% for both cases. These results show that increasing the allowable car loads will have a substantial effect on the track structure deformation, especially when the fouling content and moisture increase.

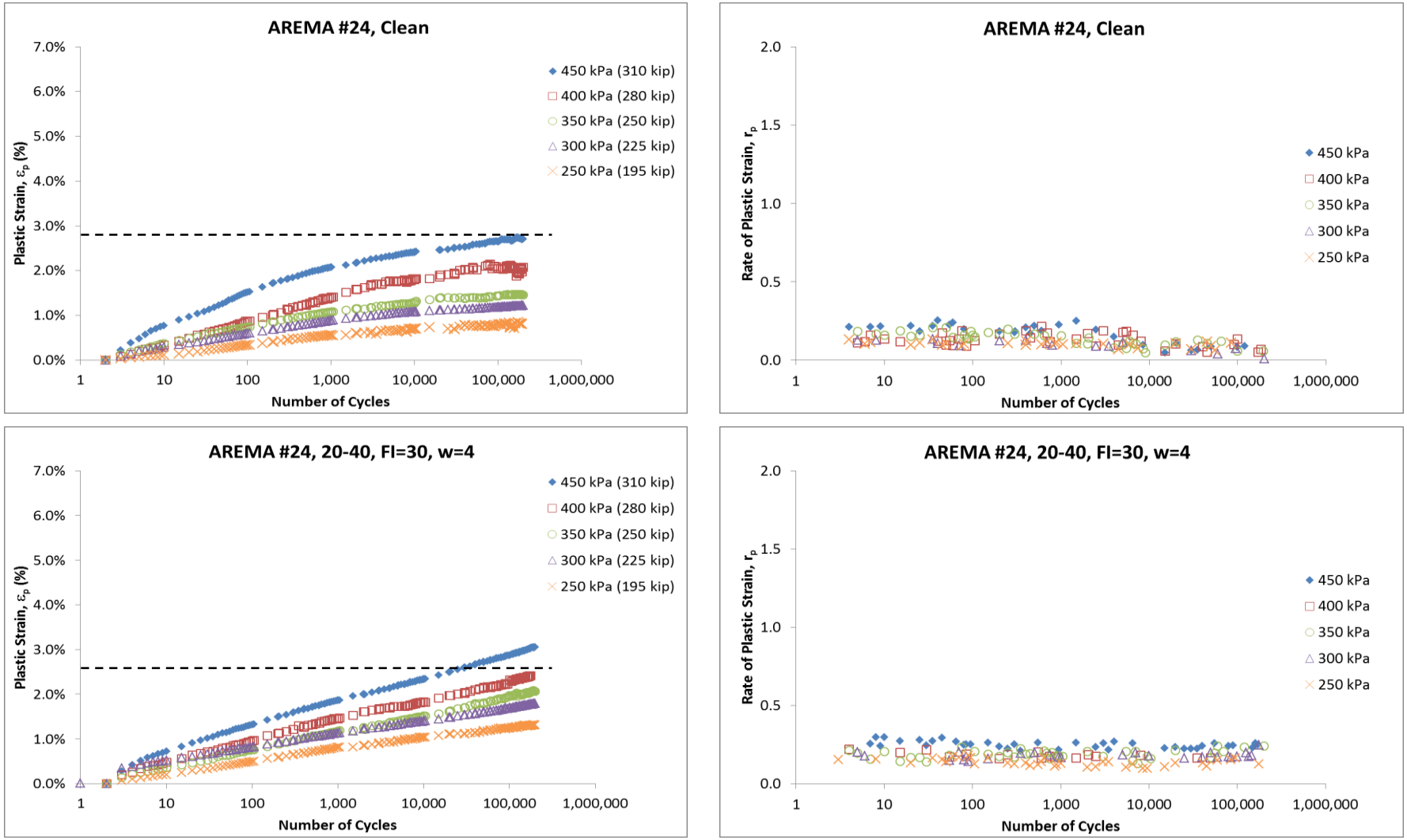

Figure 5.1.10 Comparison of HAL for AREMA #24 ballast, FI = 0, 30, and w = 0, 4.

5.1.6. Fresh s. Recycled Ballast Tests; FI = 0; w = 0; (σ_d = 300 kPa & 450 kPa)

For this study, ballast was recycled because of the limited supply of fresh ballast material for the number of tests. For the AREMA #24 and AREMA #5 ballast, the initial supply was around 350 kg to 400 kg each, which allowed for roughly five tests, therefore these ballast were recycled 2 to 3 times during this study. The AREMA #4A ballast initial supply was 900 kg to 1000 kg, which allowed for roughly 15 tests and therefore was not recycled during this study. The frac sand used in this study also needed to be sieved for the 20/40 and 40/70 gradations due to limited supply and fine content build up during the tests from ballast breakage. These initial quantity of these two gradations totaled roughly 200 kg each, resulting in enough material for 9 to 10 tests at FI = 30. The initial quantity of the 70/140 frac sand totaled roughly 400 kg which allowed for 19 to 20 tests at FI=30 and this material, therefore, was not recycled during this study. The process for recycling the ballast and frac sand was to sieve the ballast after each test to remove any fines that accumulated that were not contained in the initial gradations. When frac sand and water was introduced for a test, a large drying oven was used to dry all the material before sieving.

Fresh versus recycled ballast was a concern for this study due to limited supply and high number of tests. Figure 5.1.11 shows the comparison results for recycled versus fresh ballast under two different loading conditions. The two tests were run for recycled ballast at 450 kPa with large resulting differences in total plastic strain through 200,000 loading cycles. Tutumluer et al. (2006) stated that aggregate type and shape can directly affect the compaction of ballast, lateral stability, and long-term performance. This suggests that the recycled ballast shape, due to particle chipping or breakage, may

have a significant effect on the ballast performance and could explain the behavior seen here.

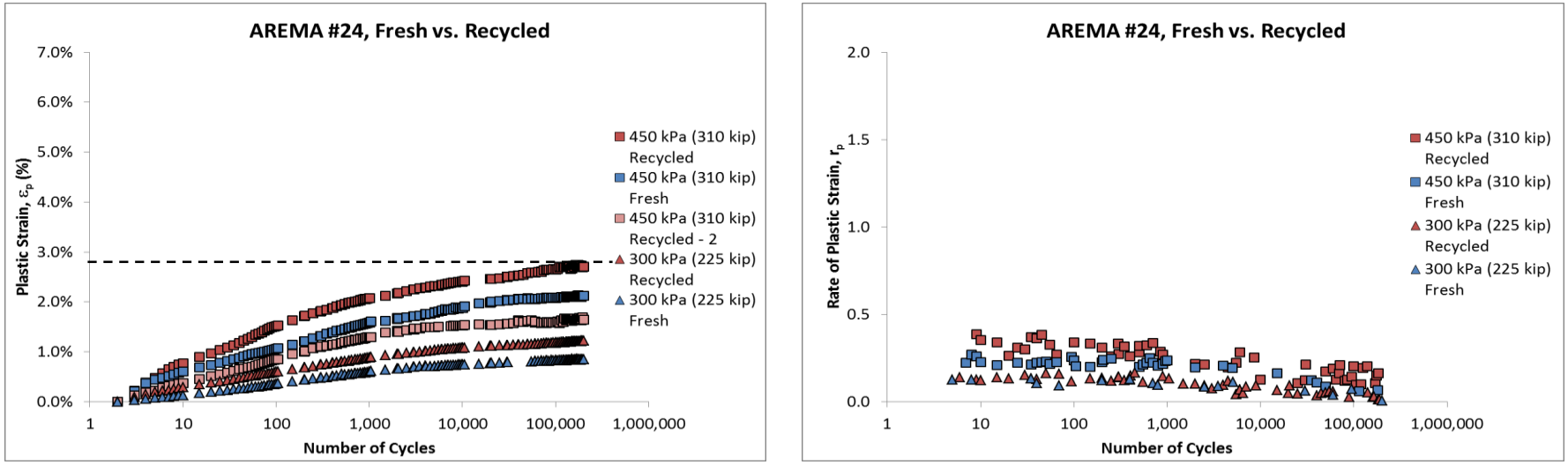

Figure 5.1.11 Comparison of fresh versus recycled for AREMA #24 ballast, FI = 0, w = 0, and σ_d = 300 kPa, 450 kPa

5.2. WiscRail™ Modeling and Maintenance Cycles

5.2.1. WiscRail™ Model Background and Development

Predicting maintenance cycles based on the results of the LSCT testing can be used to estimate the life cycle cost impacts of transporting heavy tonnages of frac sand. Previous work by Ebrahimi (2011) studied the effect of mineral, coal, and clay fouling on ballast deformation and he developed a deformation model that integrated moisture, fouling, and state of stress (Figure 5.1.12). The following equations (Eqn. 5-3 to Eqn. 5-8) integrate the rate of plastic strain, as determined from the LSCT testing at a specific load, fouling, and water content, for each traffic increment (N_i to N_{i+1}) in the model (Figure 5.13). The input parameters R_a and R_b (Eqn. 5-8) are determined from the LSCT results for each ballast and frac sand combination. The variation in behavior due to the water content and fouling content for each combination of ballast and frac sand, allows the model to accommodate increasing fouling accumulation and seasonal changes.

$$\delta\varepsilon_{pi} = \int_{N_i}^{N_{i+1}} \frac{d\varepsilon_p}{d(\ln N)} d(\ln N) \qquad \text{Eqn. 5-3.}$$

$$\varepsilon_P(N) = \sum_{i=1}^{N} \left(\int_{Ni}^{N_{i+1}} \left(\frac{d\varepsilon_p}{d(\ln N)} \right)_i d(\ln N) \right) \qquad \text{Eqn. 5-4.}$$

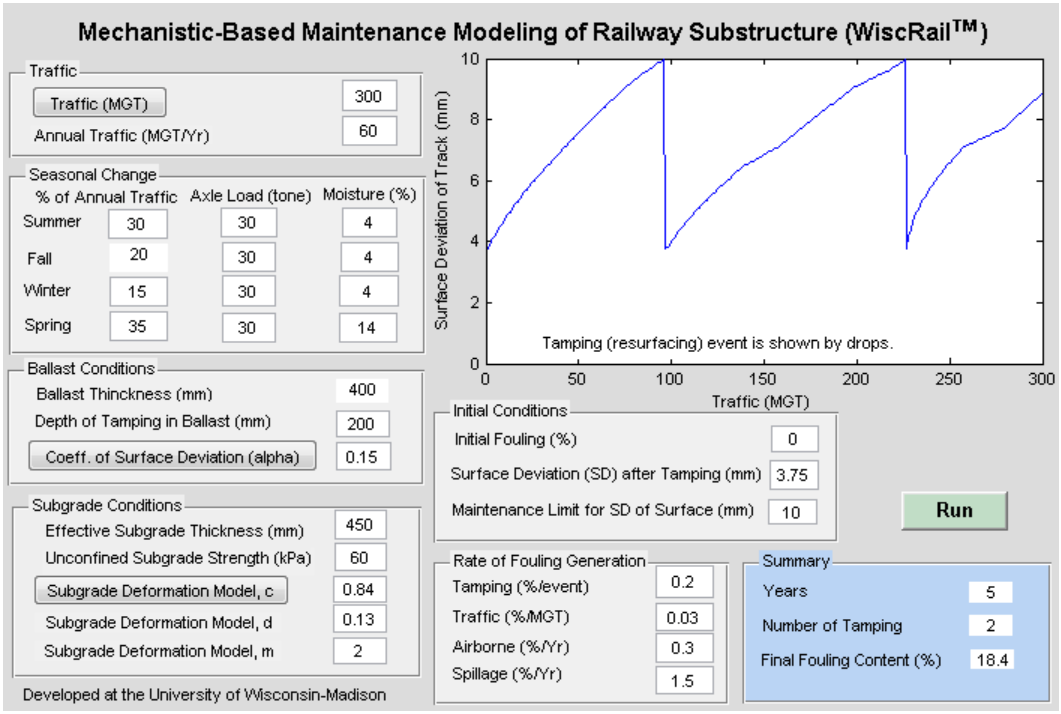

Figure 5.1.12 WiscRail™ program interface with sample data

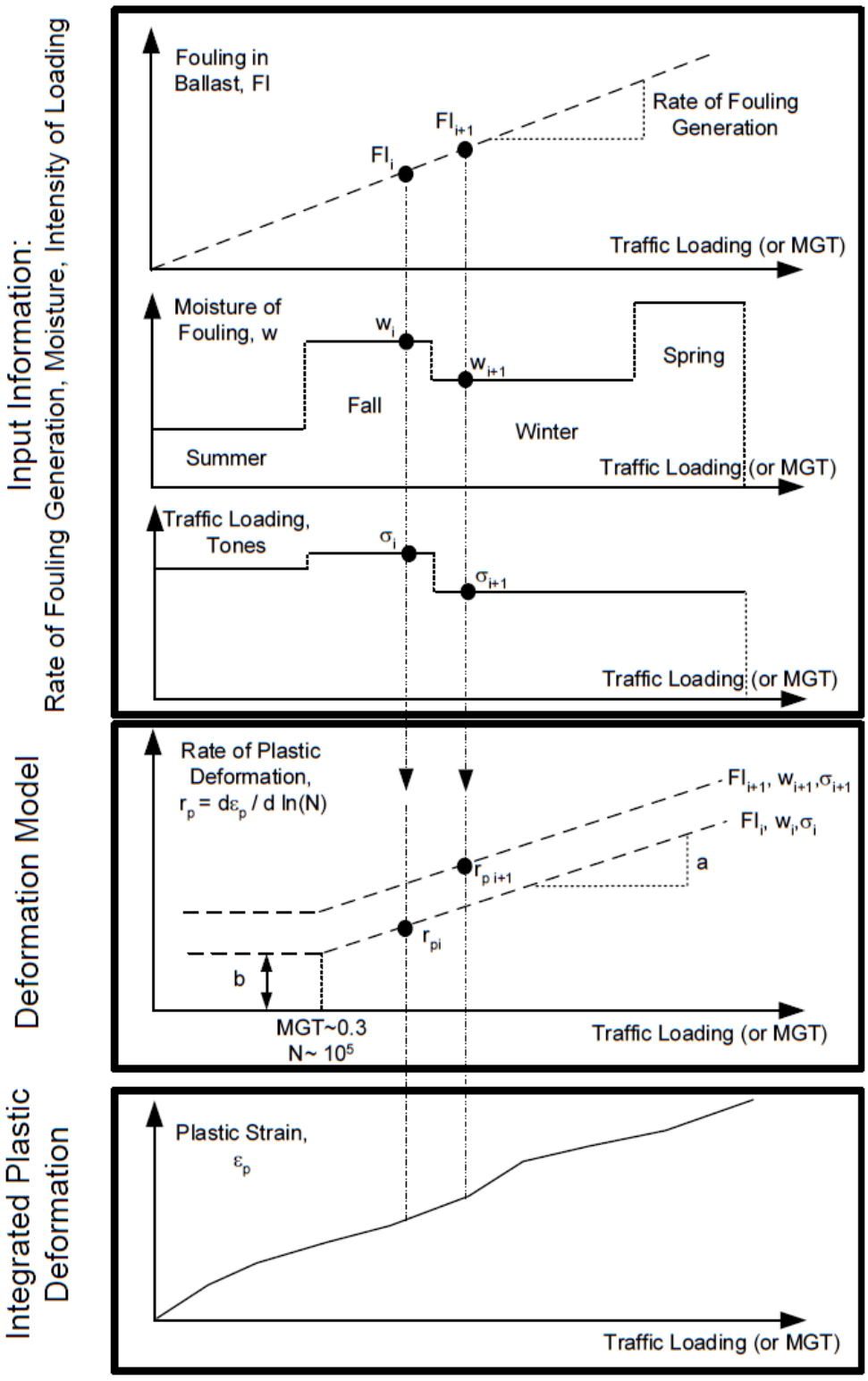

Figure 5.1.13 Maintenance planning model WiscRail™ using fouling, moisture, loading conditions, and seasonal variations (Ebrahimi 2011)

5.2.1.1. Fouling Content and Moisture - Model Considerations

The WiscRail™ takes into account the fouling and moisture content with options to specify the fouling from tamping, traffic, airborne, and spillage activities as well as specify the initial fouling content. Moisture content can be specified for each season throughout the year. Based on the results of the LSCT the key parameters that will be modified to show any changes in maintenance cycles are: Annual Traffic (MGT/Yr), Axle Load (tone), and Moisture (%).

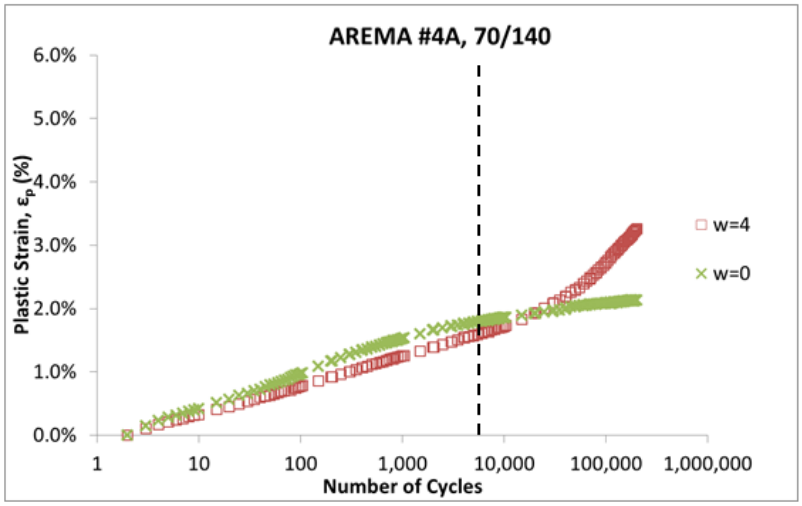

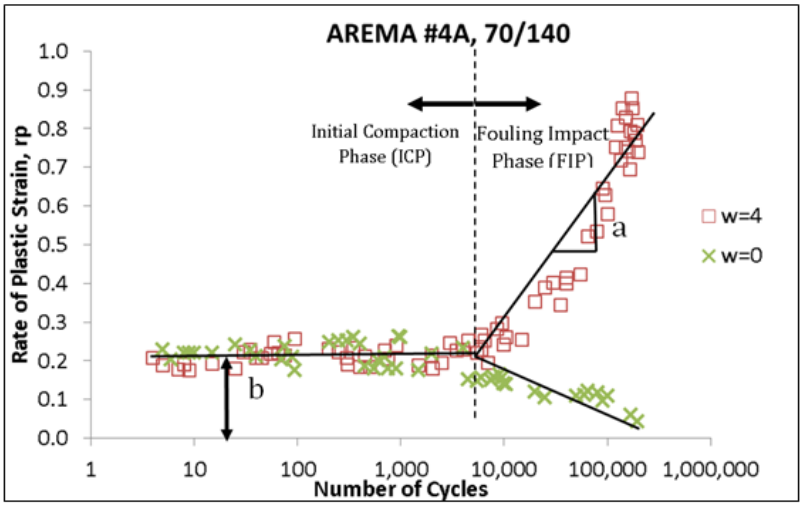

Figure 5.1.14 WiscRail model parameters 'a' and 'b' for sample data. These parameters will vary for changing ballast type, fouling type, fouling content, and moisture content.

The following equations show two parameters ('a' and 'b') that define the fouling rate of the ballast under varying loading, fouling, and moisture conditions (Figure 5.1.14) (Ebrahimi 2011).

$$r_p = \frac{d_{\varepsilon_p}}{d \ln N} = b \quad for \quad N < 10^4 \ (0.3\ MGT) \qquad \text{Eqn. 5-5.}$$

$$r_p = \frac{d_{\varepsilon_p}}{d \ln N} = b + a \log(N - 10^4) \quad for \quad N > 10^4 \qquad \text{Eqn. 5-6.}$$

These two parameters were obtained from every ballast and frac sand combination that had at least two different water contents and two different fouling indexes. The following two equations calculate the a_{ref} and b_{ref} parameters from the ratio of principle stresses and the 'a' and 'b' parameters obtained from each test condition (Ebrahimi 2011).

$$\frac{a}{a_{ref}} = 0.20 \left(\frac{\sigma_1}{\sigma_3}\right) \quad and \quad \frac{b}{b_{ref}} = 0.26 \left(\frac{\sigma_1}{\sigma_3}\right) - 0.26 \qquad \text{Eqn. 5-7.}$$

The following two equations calculate the R_a and R_b parameters that are in the WiscRail™ code and must be adjusted for every ballast and frac sand combination applied to the model (Ebrahimi 2011).

$$a_{ref} = R_a FI(w - 3) \quad and \quad b_{ref} = R_a FI(w - 3) + b_0 \qquad \text{Eqn. 5-8.}$$

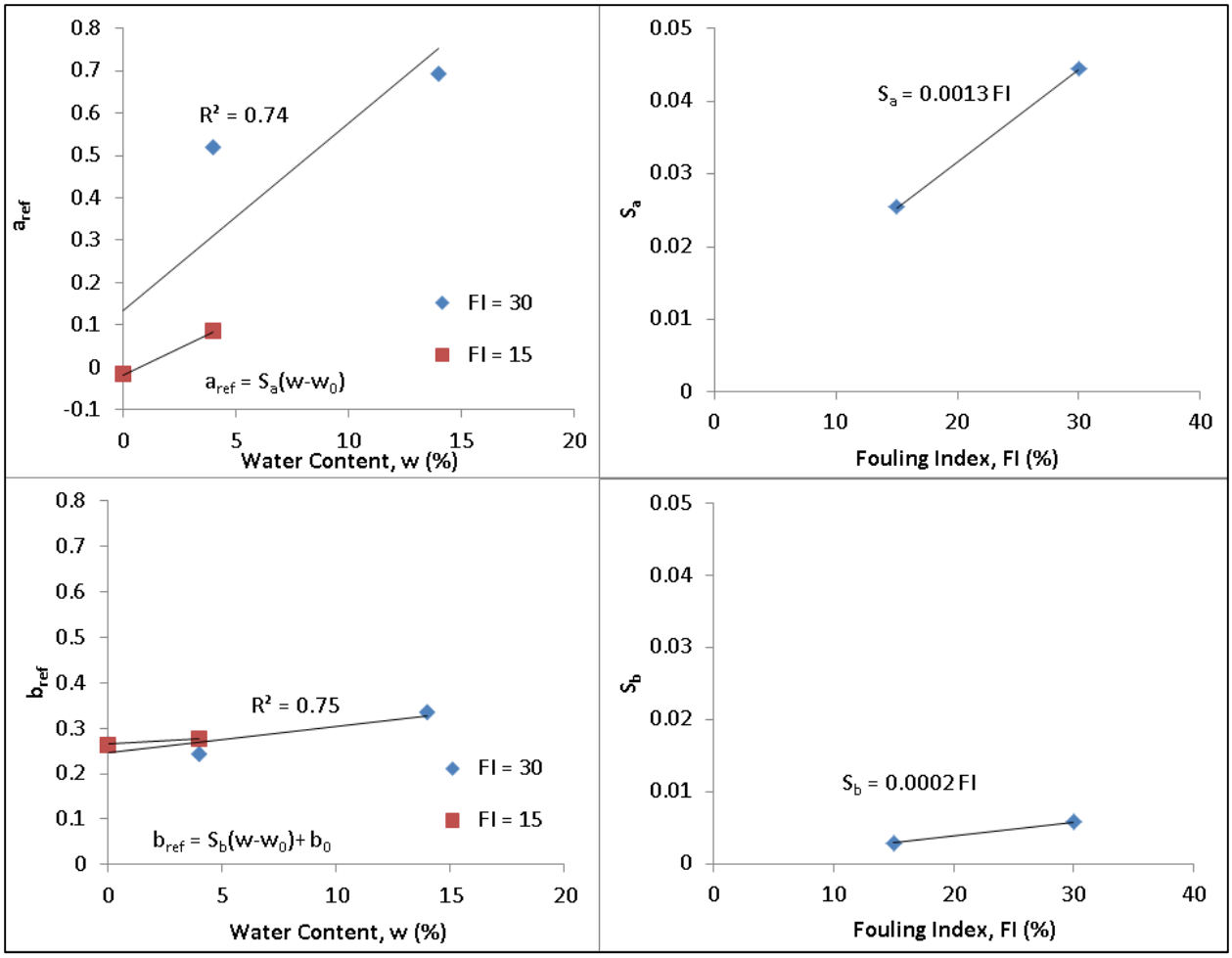

Figure 5.1.15 WiscRail™ parameters derived from 'a' and 'b' LSCT deformation parameters as a function of fouling index and water content.

5.2.1.2. State of Stress - Model Considerations

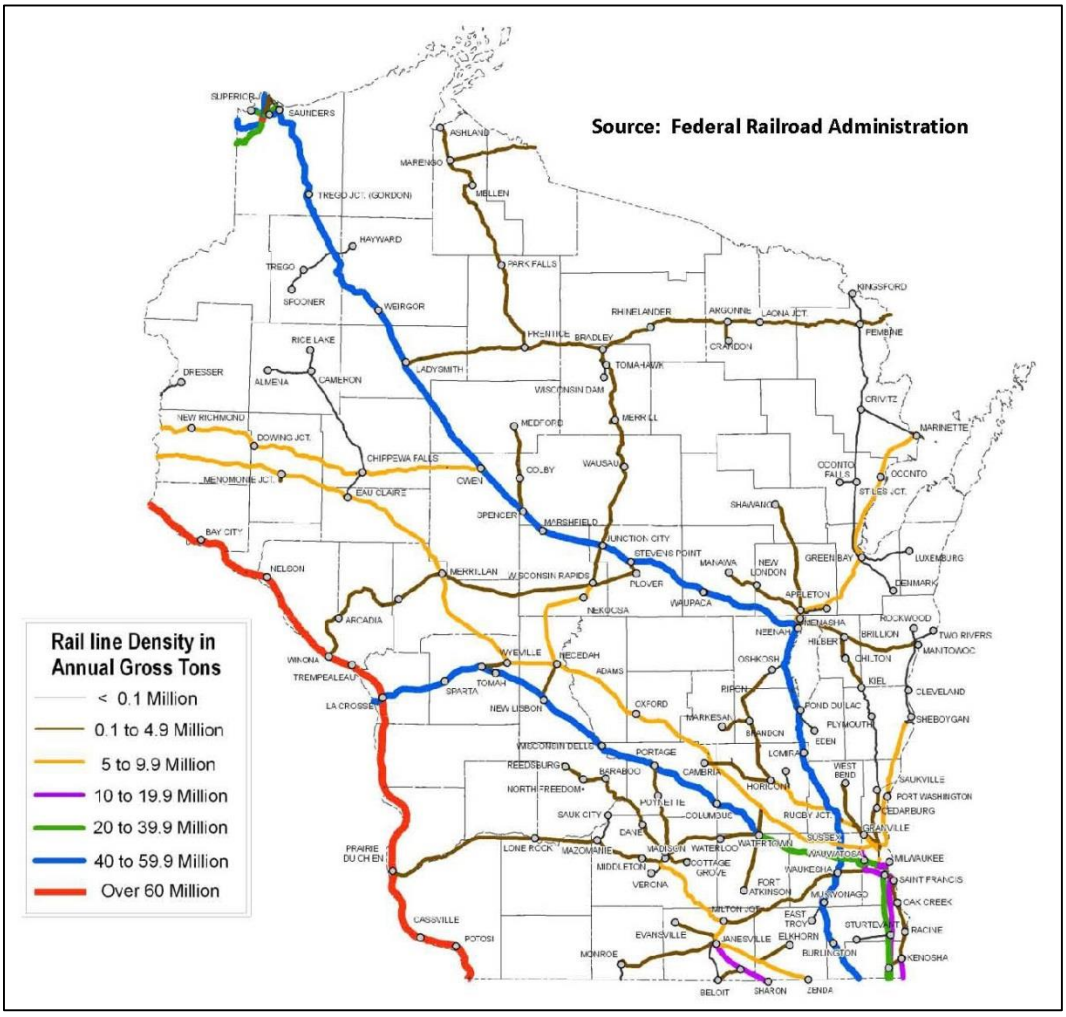

Figure 5.1.16 Wisconsin Rail Densities in MGT, 2007 study from the FRA (Wisconsin DOT 2010)

State of stress conditions can be specified in the model for each season of the year in axle load, as well as percentage of annual tonnage. For this study, a range of MGT was used to assess the variation in rail line densities per year (Figure 5.1.16). Varying axle loads were used in this model and were calculated in Section 2.1.2.1.

5.2.1.3. Ballast Conditions - Model Considerations

Ballast conditions for this model include thickness, depth of tamping, and coefficient of surface deviation. Ballast thickness is assumed to be 400 mm as ballast depth recommendations range from 300 mm to 450 mm (Uzarski 2009; Tutumluer et al. 2006). Reasonable depth of tamping is assumed to be at least 150 mm due to depth of tie in the ballast layer (Approx. 130 mm) and at most 300 mm (Tutumluer et al. 2006). The coefficient of surface deviation, α, is defined as the ratio of standard deviation track roughness divided by the average track settlement. The coefficient of surface deviation was calculated to be between 0.05 and 0.2 with an average of 0.15, which was used in this study (Chrismer 1994).

5.2.1.4. Subgrade Conditions - Model Considerations

Subgrade conditions for this model are derived from two previous works (Selig and Waters 1994) and (Li and Selig 1996). Subgrade deformation model parameters c, d, and m shown in Table 5.1.2 and used in the following equation to calculate the subgrade strain:

$$\varepsilon_p = c\left(\frac{\sigma_d}{\sigma_s}\right)^m N^d, \qquad \text{Eqn. 5-9}$$

where σ_d = deviator stress and σ_s = unconfined subgrade strength

Table 5.1.2 Subgrade Deformation Model Parameters (Li and Selig 1996).

Model Parameters	Subgrade Classification			
	ML	MH	CL	CH
d	0.1	0.13	0.16	0.18
c	0.64	0.84	1.1	1.2
m	1.7	2.0	2.0	2.4

5.2.2. WiscRail™ Results

The summary results are shown below in green highlight with the parameters that vary from model to model highlighted in blue (Table 5.1.3). Models 1-5 represent the HAL for AREMA #2, while models 6-13 represent standard stress conditions for various ballast and frac sand combinations at low and high moisture conditions.

Table 5.1.3 WiscRail™ model parameters used for this study to determine the effect of axel load, moisture, and fouling content on the maintenance cycles of track ballast.

	Model 1	Model 2	Model 3	Model 4	Model 5	Model 6	Model 7	Model 8	Model 9	Model 10	Model 11	Model 12	Model 13
Traffic	**#24, 20/40**	**#24, 20/40**	**#24, 20/40**	**#24, 20/40**	**#24, 20/40**	**#24, 20/40**	**#4A, 20/40**	**#4A, 70/140**	**#5, 20/40**	**#24, 20/40**	**#4A, 20/40**	**#4A, 70/140**	**#5, 20/40**
Traffic (MGT)	480	480	480	480	480	480	480	300	300	480	480	300	480
Annual Traffic (MGT/Yr)	60	60	60	60	60	60	60	60	60	60	60	60	60
Seasonal Change	**194 kip**	**223 kip**	**252 kip**	**280 kip**	**310 kip**	**223 kip**	**223 kip**	**223 kip**	**223 kip**	**223 kip**	**223 kip**	**223 kip**	**223 kip**
Summer (% Annual Traffic, Axel Load (tone), Moisture (%))	30, 25, 4	30, 28, 4	30, 32, 4	30, 35, 4	30, 39, 4	30, 28, 4	30, 28, 4	30, 28, 4	30, 28, 4	30, 28, 14	30, 28, 14	30, 28, 14	30, 28, 14
Fall (% Annual Traffic, Axel Load (tone), Moisture (%))	20, 25, 4	20, 28, 4	20, 32, 4	20, 35, 4	20, 39, 4	20, 28, 4	20, 28, 4	20, 28, 4	20, 28, 4	20, 28, 14	20, 28, 14	20, 28, 14	20, 28, 14
Winter (% Annual Traffic, Axel Load (tone), Moisture (%))	15, 25, 4	15, 28, 4	15, 32, 4	15, 35, 4	15, 39, 4	15, 28, 4	15, 28, 4	15, 28, 4	15, 28, 4	15, 28, 14	15, 28, 14	15, 28, 14	15, 28, 14
Spring (% Annual Traffic, Axel Load (tone), Moisture (%))	35, 25, 14	35, 28, 14	35, 32, 14	35, 35, 14	35, 39, 14	35, 28, 14	35, 28, 14	35, 28, 14	35, 28, 14	35, 28, 14	35, 28, 14	35, 28, 14	35, 28, 14
Ballast Conditions													
Ballast Thickness (mm)	400	400	400	400	400	400	400	400	400	400	400	400	400
Depth of Tamping in Ballast (mm)	200	200	200	200	200	200	200	200	200	200	200	200	200
Coeff. Of Surface Deviation (α)	0.15	0.15	0.15	0.15	0.15	0.15	0.15	0.15	0.15	0.15	0.15	0.15	0.15
Subgrade Conditions													
Effective Subgrade Thickness (mm)	450	450	450	450	450	450	450	450	450	450	450	450	450
Unconfined Subgrade Strength (kPa)	60	60	60	60	60	60	60	60	60	60	60	60	60
Subgrade Deformation Model (c, d, m)	0.84, 0.13, 2	0.84, 0.13, 2	0.84, 0.13, 2	0.84, 0.13, 2	0.84, 0.13, 2	0.84, 0.13, 2	0.84, 0.13, 2	0.84, 0.13, 2	0.84, 0.13, 2	0.84, 0.13, 2	0.84, 0.13, 2	0.84, 0.13, 2	0.84, 0.13, 2
Initial Conditions													
Initial Fouling (%)	0	0	0	0	0	0	0	0	0	0	0	0	0
Surface Deviation (SD) after Tamping (mm)	3.75	3.75	3.75	3.75	3.75	3.75	3.75	3.75	3.75	3.75	3.75	3.75	3.75
Maintenance Limit for SD of Surface (mm)	10	10	10	10	10	10	10	10	10	10	10	10	10
Rate of Fouling Generation													
Tamping (%/event)	0.2	0.2	0.2	0.2	0.2	0.2	0.2	0.2	0.2	0.2	0.2	0.2	0.2
Traffic (%/MGT)	0.03	0.03	0.03	0.03	0.03	0.03	0.03	0.03	0.03	0.03	0.03	0.03	0.03
Airborne (%/Yr)	0.3	0.3	0.3	0.3	0.3	0.3	0.3	0.3	0.3	0.3	0.3	0.3	0.3
Spillage (%/Yr)	1.5	1.5	1.5	1.5	1.5	1.5	1.5	1.5	1.5	1.5	1.5	1.5	1.5
Internal parameters that control fouling and moisture													
R_a	0.000007	0.000007	0.000007	0.000007	0.000007	0.000007	0.0009	0.0013	0.0018	0.000007	0.0009	0.0013	0.0018
R_b	0.0002	0.0002	0.0002	0.0002	0.0002	0.0002	0.0002	0.0002	0.0008	0.0002	0.0002	0.0002	0.0008
Summary Results													
Years	8	8	8	8	8	8	8	8	8	8	8	8	8
Number of Tampings	1	2	3	3	4	2	3	3	6	2	3	5	6
Final Fouling Content (%)	29	29.2	29.4	29.4	29.6	29.2	29.4	29.4	30	29.2	29.4	29.8	30

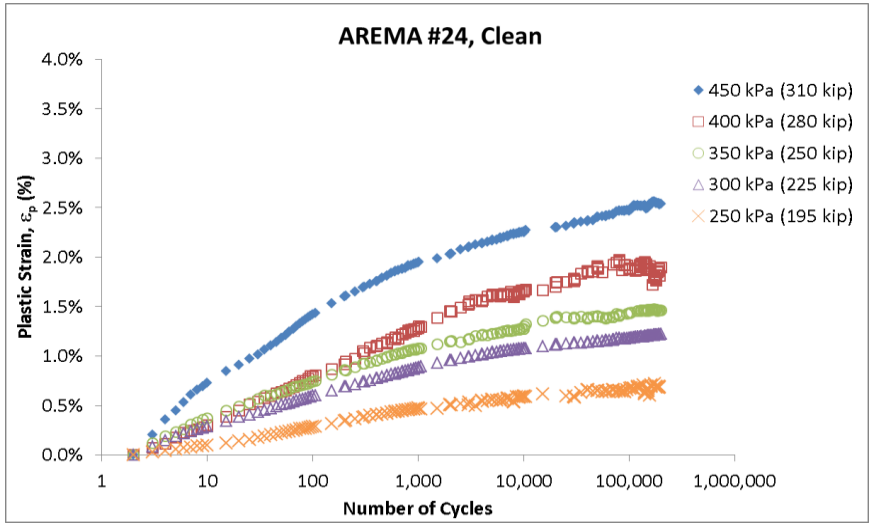
AREMA #24, Clean
Plastic Strain, ε_p (%)
4.0%
3.5%
3.0%
2.5%
2.0%
1.5%
1.0%
0.5%
0.0%
1
10
100
1,000
10,000
100,000
1,000,000
Number of Cycles
450 kPa (310 kip)
400 kPa (280 kip)
350 kPa (250 kip)
300 kPa (225 kip)
250 kPa (195 kip)

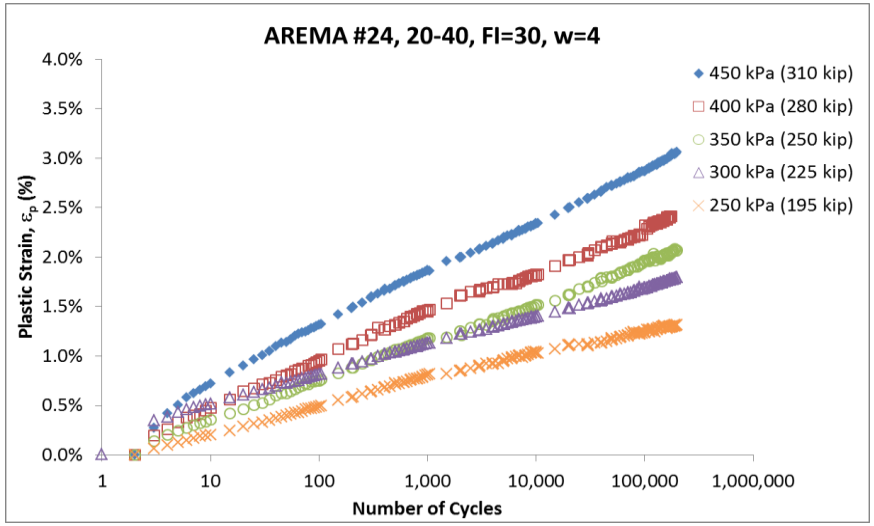
AREMA #24, 20-40, FI=30, w=4
Plastic Strain, ε_p (%)
4.0%
3.5%
3.0%
2.5%
2.0%
1.5%
1.0%
0.5%
0.0%
1
10
100
1,000
10,000
100,000
1,000,000
Number of Cycles
450 kPa (310 kip)
400 kPa (280 kip)
350 kPa (250 kip)
300 kPa (225 kip)
250 kPa (195 kip)

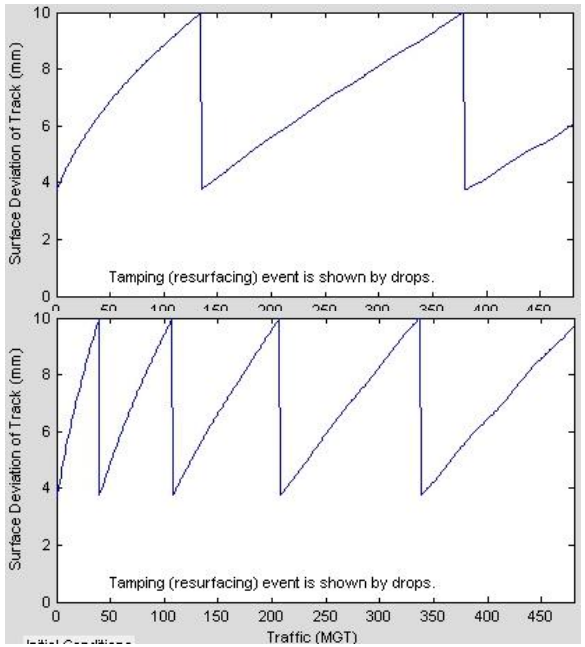

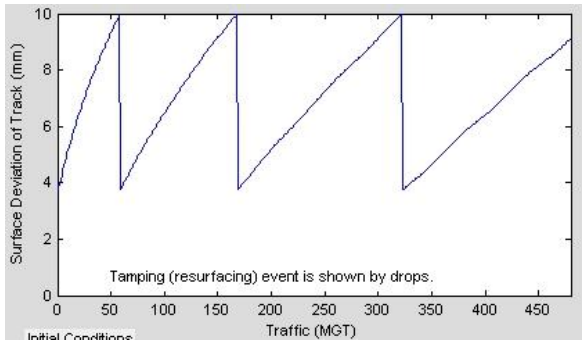

Figure 5.1.17 WiscRail™ model results for HAL with 225, 280, and 310 kip graphs represented.

The HAL model results in combination with the LSCT results show that for the same fouling and moisture conditions maintenance cycles are significantly affected (Figure 5.1.17). At the end of the 8 year period the ballast will need to be replaced for all models as the fouling index approaches the limit of 30%.

The following four figures show the results of the standard load (σ_d = 300 kPa, σ_c = 90 kPa) LSCT tests and the associated model results. Figure 5.1.19 shows the model results for AREMA #24, 20/40 for dry conditions (w = 4, 4, 4, and 14) and wet conditions (w = 14, 14, 14, and 14) for summer, fall, winter, and spring, respectively. The model results show no difference in maintenance cycles when changing the moisture content over the course of the 8 year ballast life cycle. Figure 5.1.19 shows the model results for AREMA #4A, 20/40 for dry and wet conditions. The model results show no difference in maintenance cycles when changing the moisture content, though the maintenance cycles for the wet condition are closer together than the dry condition. Figure 5.1.20 shows the model results for AREMA #4A, 70/140 for dry and wet conditions. The model results show a significant difference in maintenance cycles (3 vs. 5) when changing the moisture content. Figure 5.1.21 shows the model results for AREMA #5, 20/40 for dry and wet conditions. The model results no significant difference in maintenance cycles when changing the moisture content.

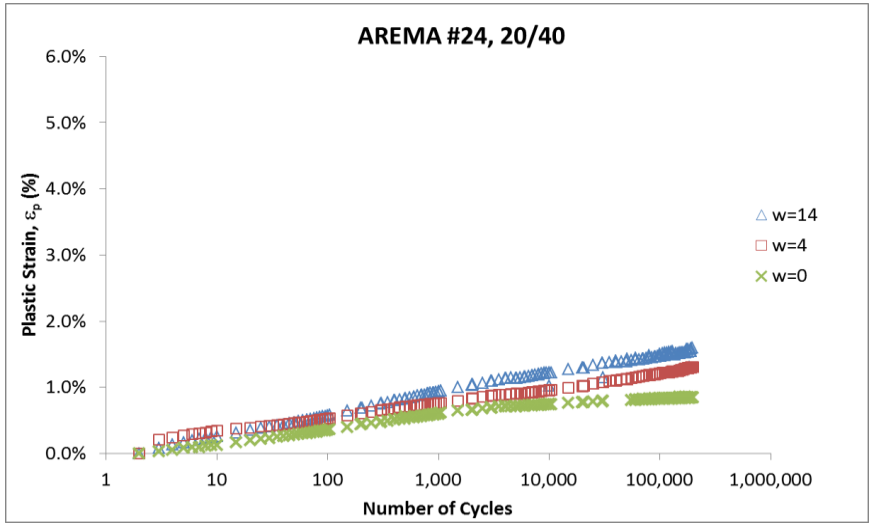
AREMA #24, 20/40
6.0%
5.0%
4.0%
3.0%
2.0%
1.0%
0.0%
Plastic Strain, ε_p (%)
1
10
100
1,000
10,000
100,000
1,000,000
Number of Cycles
w=14
w=4
w=0

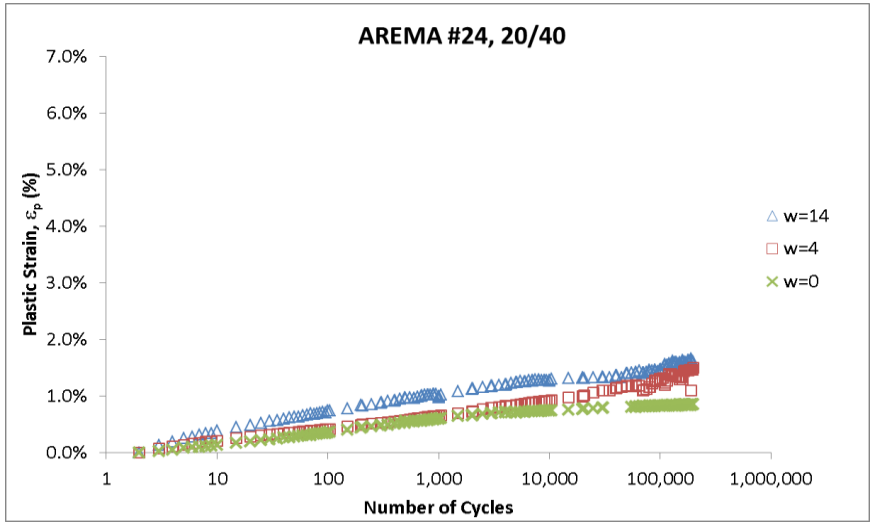
AREMA #24, 20/40
7.0%
6.0%
5.0%
4.0%
3.0%
2.0%
1.0%
0.0%
Plastic Strain, ε_p (%)
1
10
100
1,000
10,000
100,000
1,000,000
Number of Cycles
w=14
w=4
w=0

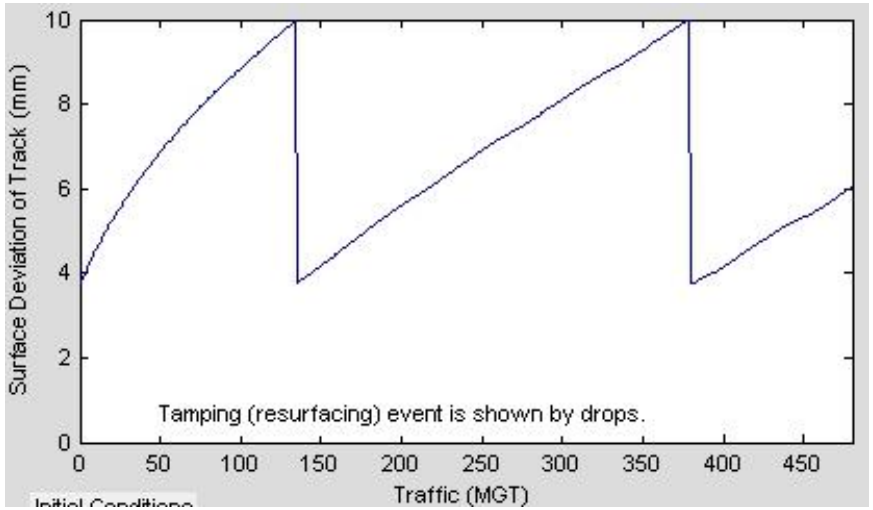

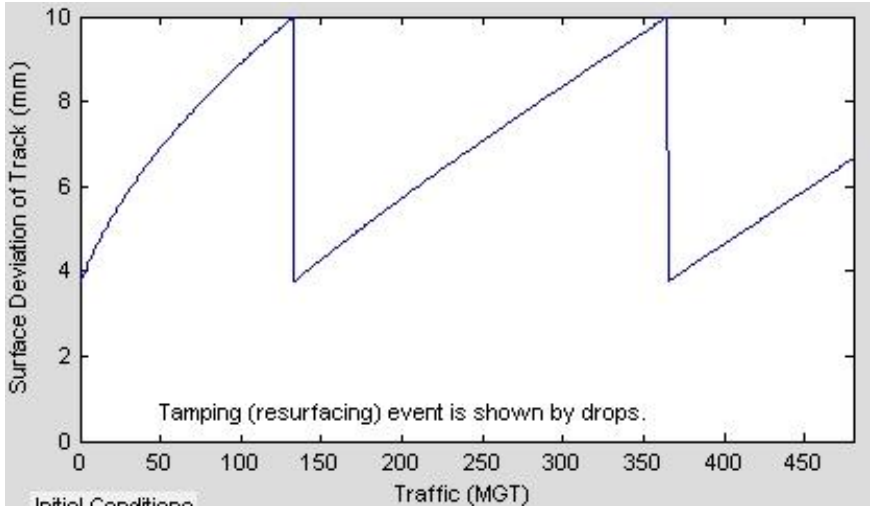

Figure 5.1.18 WiscRail™ model results for AREMA #24 with 20/40 frac sand varying the water conditions.

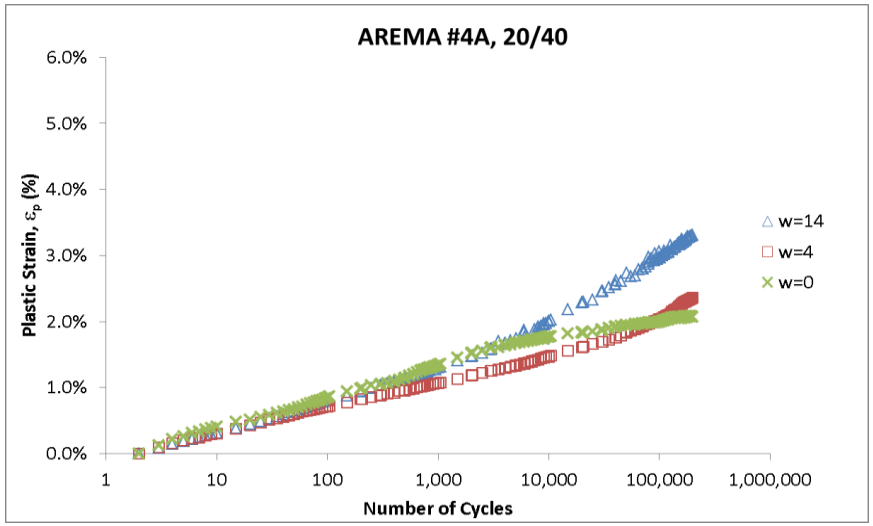

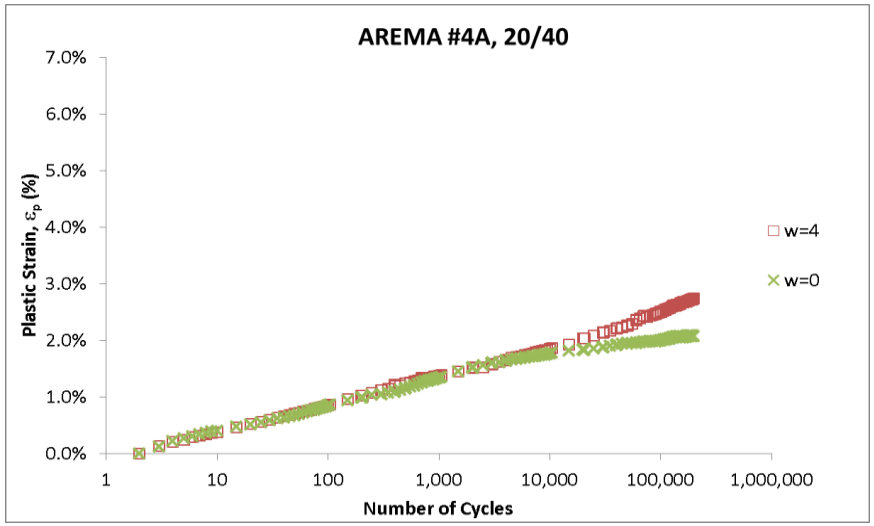

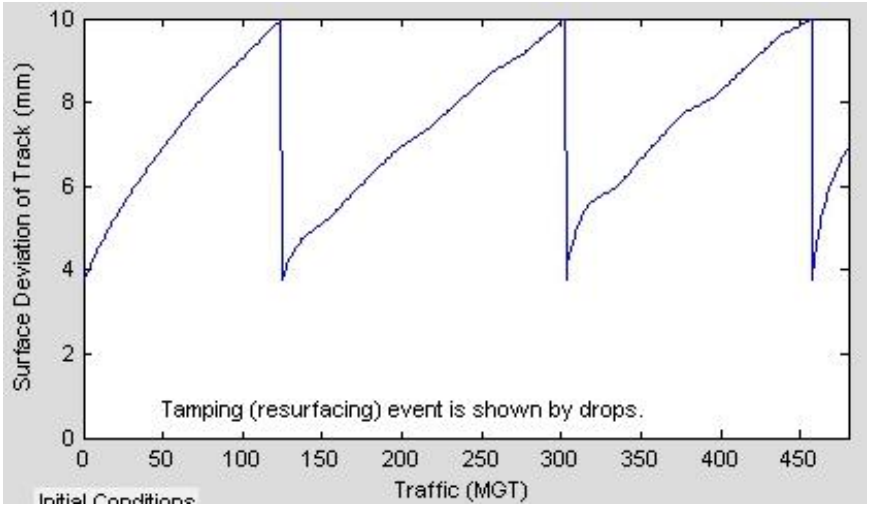

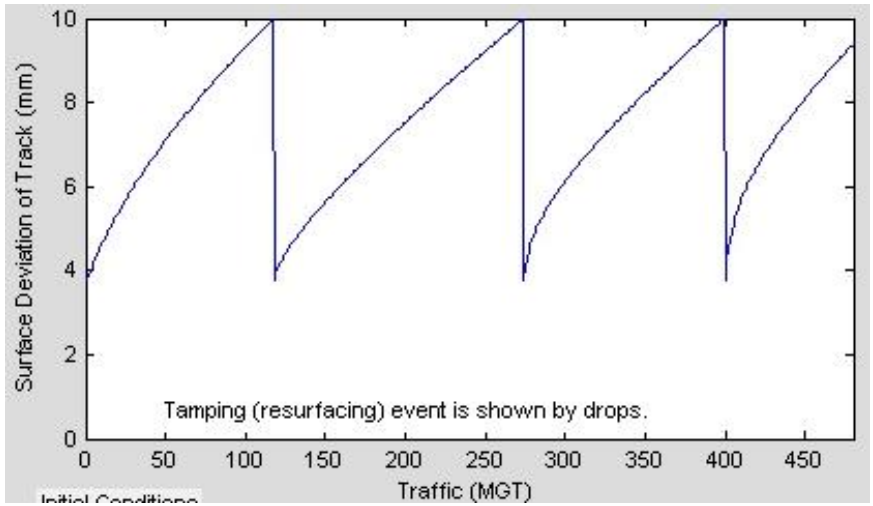

Figure 5.1.19 WiscRail™ model results for AREMA #4A with 20/40 frac sand varying the water conditions.

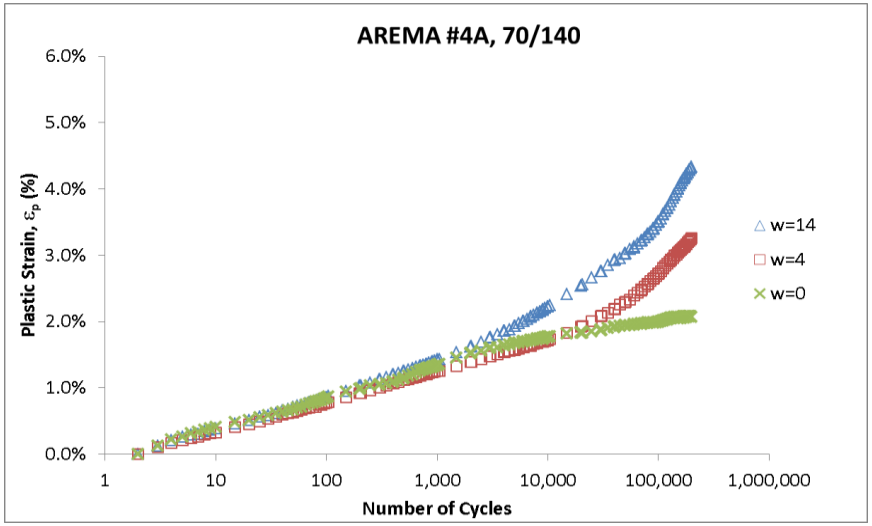

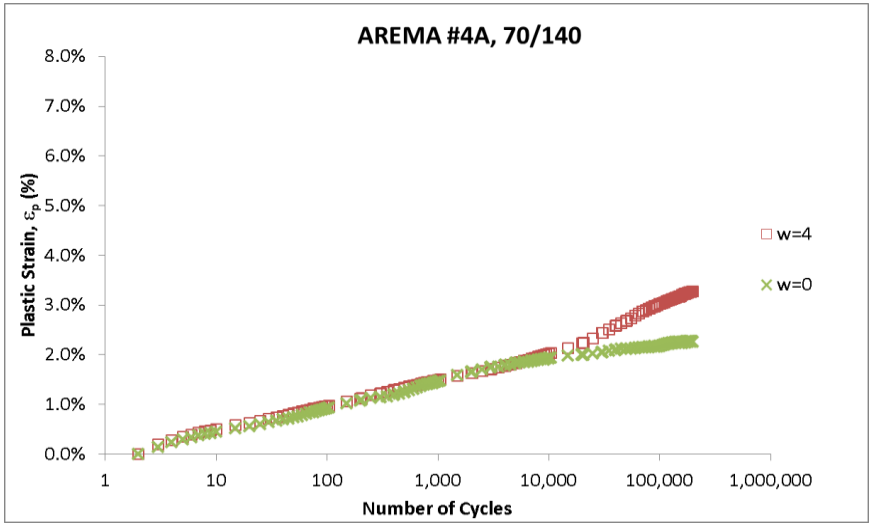

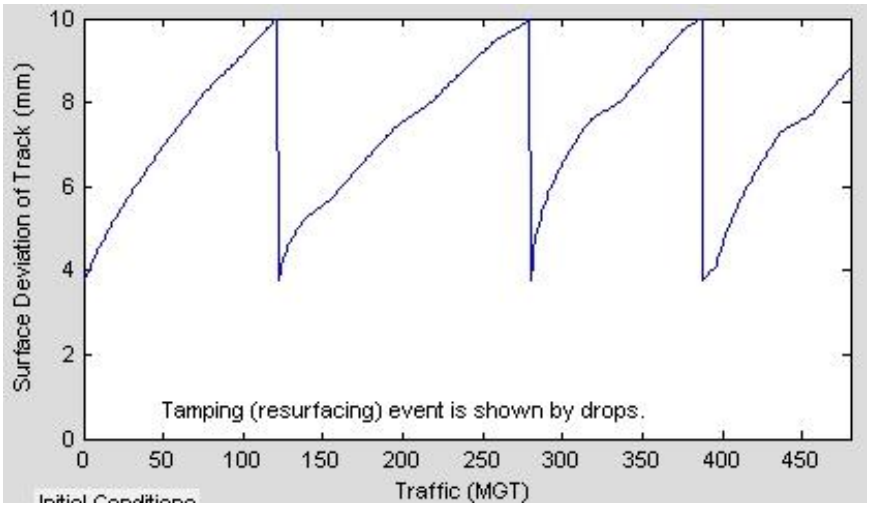

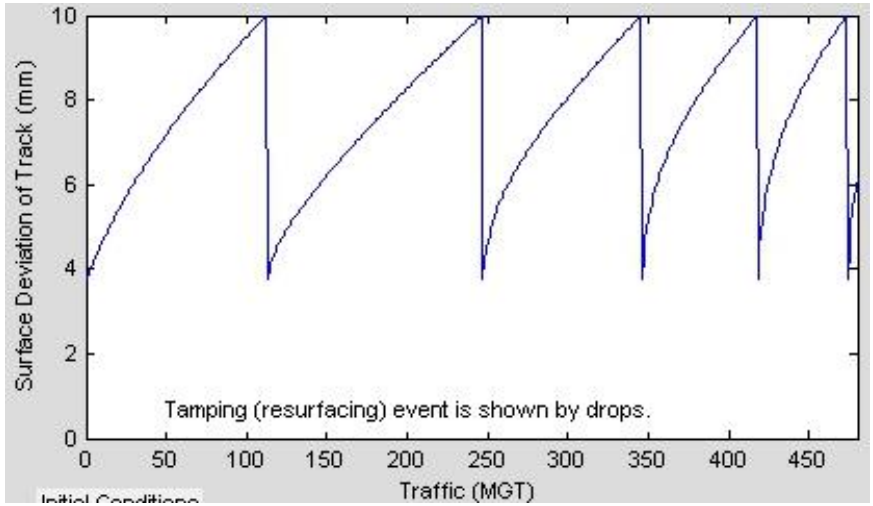

Figure 5.1.20 WiscRail™ model results for AREMA #4A with 70/140 frac sand varying the water conditions.

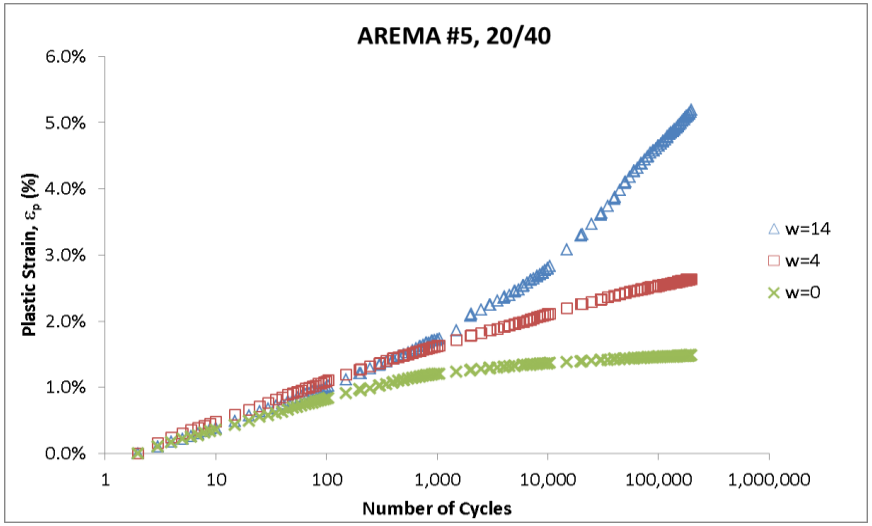

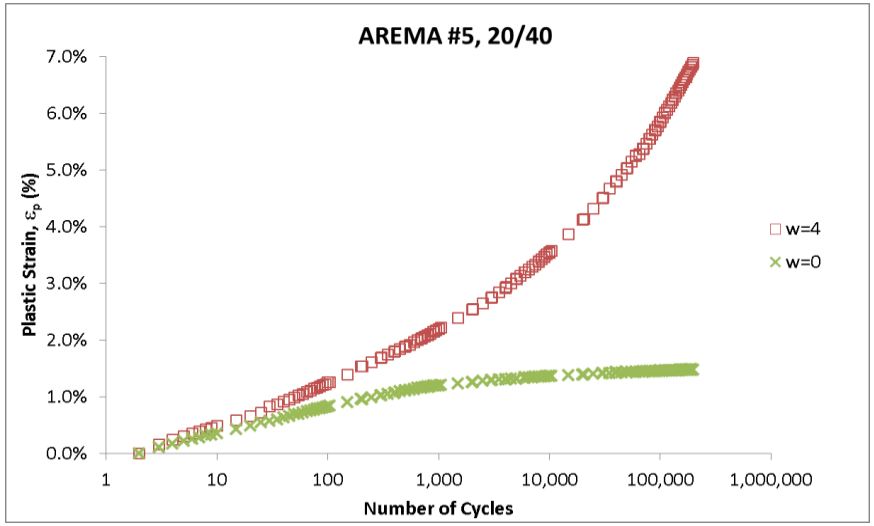

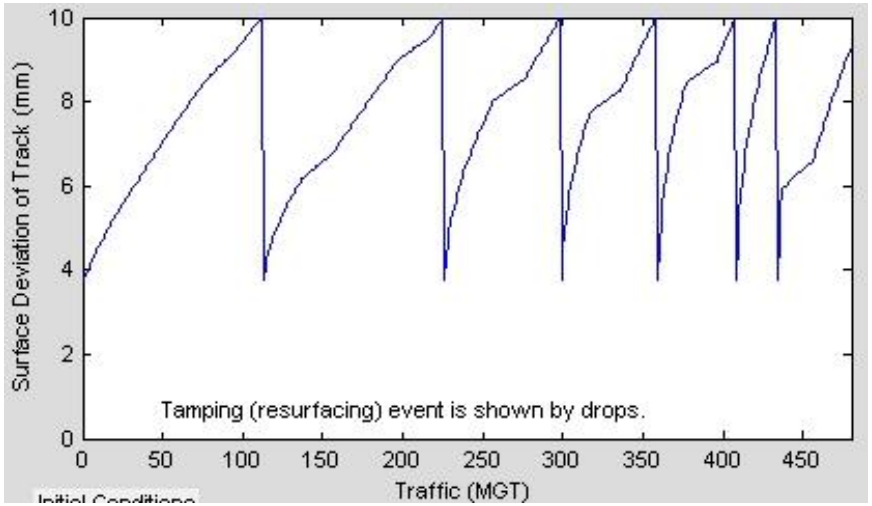

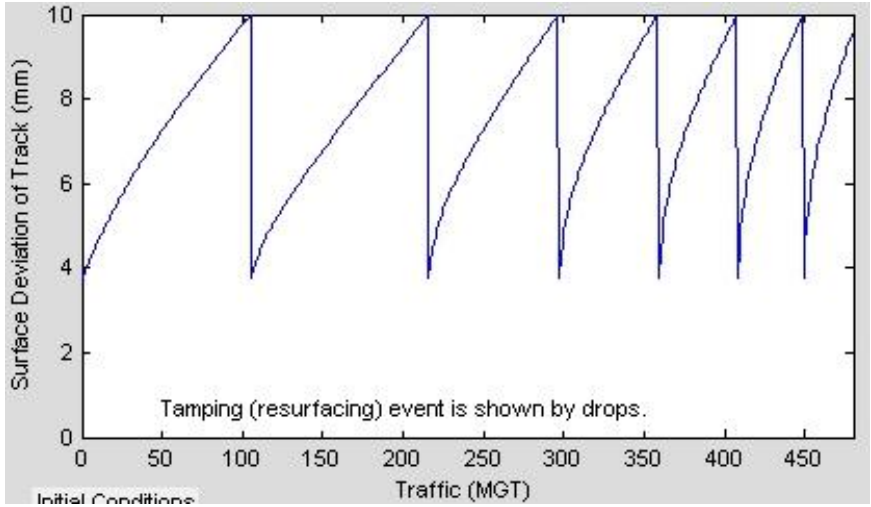

Figure 5.1.21 WiscRail™ model results for AREMA #5 with 20/40 frac sand varying the water conditions

5.3. Maintenance Cost Estimates

Due to limited public information on maintenance based expenditures for railroads, the life cycle cost analysis is limited in scope and reliability. The two most likely conditions for concern in the long-term development of this industry are, AREMA #24 surface spillage and HAL. The AREMA #24 gradation is similar to much of the ballast used in mainline track. The models show no significant increase in required maintenance activity for standard loading, while the HAL models indicate that costs to tamp and add ballast will increase as loads increase. However, at this time, specific costs for tamping events and periodic ballast addition are unknown as publicly available knowledge of this level of detail is limited. Percentage based estimates of cost increases can be stated. For HAL, the cost of tamping and ballast addition could increase anywhere from 50% to 100% of current spending. If ballast of significantly lower quality (AREMA #4A and AREMA #5) is used for mainline track, at standard axle loads, cost increases from tamping and adding ballast could be anywhere from 20% to 70% based on tests from this study.

Chapter 6: Summary and Conclusions

In this paper, the effect of HAL, fouling content (surface spillage of frac sand) and moisture retention on the deformational behavior of fresh and recycled ballast was studied. The deformational behavior of the ballast was quantified using the LSCT testing apparatus with fouling contents of 15% and 30% by weight and gravimetric water contents of 0, 4, and 14.

The two phases in the trend of plastic strain accumulations (ICP and FIP), as outlined in Ebrahimi (2011), were also detailed in this study in Section 5.1 and shown in Figure 5.1.14. The mechanisms for the differences in rate of plastic strain during these two phases can be accounted for by several factors: variation in initial compaction densities, variation in water content, differences in mineralogy and particle strength, and contamination of the contact points with water and frac sand.

The results of this study indicate that water content has less of an effect on the AREMA #24 ballast than on the AREMA #4A or AREMA #5 ballast. This differs from previous studies on ballast fouling where water content plays a key role in ballast behavior for all ballast types.

For this study two different ballast types at three gradations were used to assess the effect of ballast mineralogy and gradation on ballast behavior. The results indicate that the mineralogy is likely a key factor for ballast deformation. Gradation differences between the AREMA #4A and AREMA #5 ballast, (similar mineralogy) showed similar

trends in the ICP and FIP for many of the tests, which suggests less of an effect on ballast deformation from differences in gradation.

Sand gradations used in this study were similar in hydraulic, shape, and mineralogical properties though the difference in ballast behavior was statistically significant. Fouling index results showed significant differences for AREMA #5 ballast and less for AREMA #24 and AREMA #4A ballast, though limited tests were run to determine this difference. Previous studies have indicated significant increases in ballast deformation with increases in fouling index. More testing will be need to assess the fouling index effect across all ballast, sand, and water contents.

AREMA #24 was chosen for the assessment of HAL in this study due to is mineralogy matching the most common industry used ballast types (granites and trap rock). The results of the HAL tests showed significant increases in deformation from increases in loading. This means that, for the rail industry, the bigger challenge for the transportation of frac sand may be the heavy axle conditions, even if high-quality ballast is chosen.

More tests will need to be run at additional frac sand and moisture contents to improve the modeling parameters from Section 5.2.1.1. Future work could expand the testing matrix and use those results to improve the WiscRail™ input parameters and provide better cost analysis estimations.

References

AAR. 2011. “Total Annual Spending 2011 Data”. Association of American Railroads.

AAR. 2013. “Freight Railroads in United States.”

Alsabhan, A. 2013. “Warning System and Inspection for Maintenance of Freight Railways”. University of Wisconsin-Madison.

AREMA. 2010. “AREMA Manual For Railway Engineering - Ballast Gradations.”

ASTM C127. 2012. “Standard Test Method for Density, Relative Density (Specific Gravity), and Absorption of Coarse Aggregate”. West Conshohocken, PA: ASTM International.

ASTM C29/C29M. 2013. “Standard Test Method for Bulk Density (‘Unit Weight’) and Voids in Aggregate”. West Conshohocken, PA: ASTM International.

ASTM D2434. 2006. “Standard Test Method for Permeability of Granular Soils (Constant Head)”. Vol. 68. West Conshohocken, PA: ASTM International.

ASTM D4253. 2006. “Standard Test Methods for Maximum Index Density and Unit Weight of Soils Using a Vibratory Table”. Vol. 00. West Conshohocken, PA: ASTM International.

ASTM D4254. 2006. “Standard Test Methods for Minimum Index Density and Unit Weight of Soils and Calculation of Relative Density”. Vol. 00. West Conshohocken, PA: ASTM International.

ASTM D6836. 2008. “Standard Test Methods for Determination of the Soil Water Characteristic Curve for Desorption Using Hanging Column, Pressure Extractor, Chilled Mirror Hygrometer, or Centrifuge”. West Conshohocken, PA: ASTM International.

ASTM D6913. 2009. “Standard Test Methods for Particle-Size Distribution (Gradation) of Soils Using Sieve Analysis”. Vol. 04. West Conshohocken, PA: ASTM International.

BNSF. 2012. “BNSF Railway Company Annual Report”. Fort Worth, TX.

BNSF. 2013. “Track Substructure Workshop”. Pueblo, CO.

Brown, S F, and A F L Hyde. 1975. “Significance of Cyclic Confining Stress in Repeated-Load Triaxial Testiing of Granular Material.” *Transportation Research Record* 537: 49–58.

Casagrande, A, and R E Fadum. 1940. “Notes on Soil Testing for Engineering Purposes.”

Cho, Gye-Chun, Jake Dodds, and J. Carlos Santamarina. 2006. “Particle Shape Effects on Packing Density, Stiffness, and Strength: Natural and Crushed Sands.” *J. Geotech. Geoenviron.* 132 (5) (May): 591–602.

Chrismer, Steven Mark. 1994. “Mechanics-Based Model to Predict Ballast-Related Maintenance Timing and Costs”. Amherst: University of massachusetts Amherst.

Christie, D., B. Indraratna, and J. Lackenby. 2005. “Effect of Confining Pressure on the Degradation of Ballast Under Cyclic Loading.” *Géotechnique* 55 (4) (January 5): 325–328.

Christie, D., J. Lackenby, B. Indraratna, and G. McDowell. 2007. “Effect of Confining Pressure on Ballast Degradation and Deformation Under Cyclic Triaxial Loading.” *Géotechnique* 57 (6) (January 8): 527–536.

Daview, Phil. 2012. “Frac Sand Mining Spurs Rural Rail.” *Fedgazette*, July 19.

Dawson, A R, N H Thom, and J L Paute. 1996. “Mechanical Characteristics of Unbound Granular Materials as a Fucntion of Condition.” *Flexible Pavements*: 35–44.

Dean, R. B., and W. J. Dixon. 1951. “Simplified Statistics for Small Numbers of Observations.” *Analytical Chemistry* 23 (4) (April): 636–638.

Ebrahimi, Ali. 2011. “Deformational Behavior of Fouled Railway Ballast”. University of Wisconsin - Madison.

Ebrahimi, Ali, James M Tinjum, and Tuncer B Edil. 2010. “Large-Scale, Cyclic Triaxial Testing of Rail Ballast.” In *AREMA 2010 Annual Conference & Exposition*, 1–24. Orlando, FL: AREMA.

EERC. 2010. “Stimulation Technologies.” *Bakken Decision Support System*.

FRA. 2011. “FRA Track Safety Standards (49 CFR Ch. II Part 213).”

Ghionna, Vito Nicola, and Daniela Porcino. 2006. “Liquefaction Resistance of Undisturbed and Reconstituted Samples of a Natural Coarse Sand from Undrained Cyclic Triaxial Tests” (February): 194–202.

Indraratna, B, D Ionescu, and H D Christie. 1998. “Shear Behavior of Railway Ballast Based on Large-Scale Triaxial Tests.” *J. Geotech. Geoenviron.* (May): 439–449.

Indraratna, Buddhima, F Asce, Pramod Kumar Thakur, and Jayan S Vinod. 2010. “Experimental and Numerical Study of Railway Ballast Behavior Under Cyclic Loading.” *International Journal of Geomechanics* (August): 136–145.

Indraratna, Buddhima, S. Nimbalkar, and D. Christe. 2009. “The Performance of Rail Track Incorporating the Effects of Ballast Breakage , Confining Pressure and Geosynthetic Reinforcement.” In *8th International Conference on the Bearing Capacity of Roads, Railways, and Airfields*, 5–24. London: Taylor & Francis Group.

Indraratna, Buddhima, Wadud Salim, and Cholachat Rujikiatkamjorn. 2011. *Advanced Rail Geotechnology - Ballasted Track*. Leiden, Netherlands: CRC Press.

Indraratna, Buddhima, Li-jun Su, and Cholachat Rujikiatkamjorn. 2011. “A New Parameter for Classification and Evaluation of Railway Ballast Fouling.” *Can. Geotech. J.* 48 (2) (February): 322–326.
Keene, Andrew Kenneth. 2012. “Mitigating Ballast Fouling Impact and Enhancing Rail Freight Capacity”. University of Wisconsin-Madison.
Knutson, Reid Merray. 1976. “Factors Influencing the Repeated Load Behaviour of Railway Ballast”. University of Illinois at Urbana-Champaign.
Kolbuszewski, J, and M R Frederick. 1963. “The Significance of Particle Shape and Size on the Mechanical Behavior of Granular Materials.” In *Proceedings of the European Conference on the Soil Mechanics and Foundation Engineering*, 253–263.
Kuerbis, Ralph H, and Yoginder P Vaid. 1990. “Corrections for Membrane Strength in the Triaxial Test.” *Geotechnical Testing Journal* 13 (4): 361–369.
Lekarp, Fredrick, Ulf Isacsson, and Andrew Dawson. 2000. “State of the Art I: Resilient Response of Unbound Aggregates.” *Journal of Transportation Engineering* Jan-Feb: 66–75.
Li, By Dingqing, and Ernest T Selig. 1996. “Cumulative Plastic Deformation for Fine-Grained Subgrade Soils.” *Journal of Geotechnical Engineering* (1): 1006–1013.
Lim, Wee Loon. 2004. “Mechanics of Railway Ballast Behaviour”. The Unversity of Nottingham.
Mohamad, By Ramli, and Ricardo Dobry. 1987. “Undrained Monotonic and Cyclic Triaxial Strength of Sand.” *Journal of Geotechnical Engineering* 112: 941–958.
Morgan, J R. 1966. “The Response of Granular Materials Under Repeated Loading.” In *Proceeding of the Australian Road Research Board*, 1178–1192.
Pickard, Brent. 2013. “Fracture Sand and Transportation”. Eau Claire, WI: Wisconsin DOT.
Ravichandran, Nadarajah, Brian Machmer, Hadakopan Krishnapillai, and Kimiro Meguro. 2010. “Micro-Scale Modeling of Saturated Sandy Soil Behavior Subjected to Cyclic Loading.” *Soil Dynamics and Earthquake Engineering* 30 (11) (November): 1212–1225.
Raymond, Gerald P., and Vishnu A. Diyaljee. 1979. “Railroad Ballast Load Ranking Classification.” *Journal of the Geotechnicla Engineering Division* 105 (GT10): 1132–1153.
Santamarina, J C, and G C Cho. 2004. “Soil Behaviour : The Role of Particle Shape.” In *Skempton Conference*, 1–14.
Selig, E.T., and J.M. Waters. 1994. *Track Geotechnology and Substructure Management*. New York, NY: Thomas Telford.
Shenton, M J. 1975. “Deformation of Railway Ballast Under Repeated Loading Conditions.” In *Railroad Track Mechanics and Technology*, 1–26. Princeton University.
Stewart, H E, and E.T. Selig. 1982. “Predicted and Measured Resilient Response of Track.” *Journal of Geotechnical Engineering* 108 (GT 11): 1423–1442.
Suiker, Akke S J, Ernest T Selig, and Raymond Frenkel. 2005. “Static and Cyclic Triaxial Testing of Ballast and Subballast.” *J. Geotech. Geoenviron.* (June): 771–783.
Talbot, A N. 1980. *Stresses in Railroad Track - The Talbot Reports*. American Railway Engineering Associations.
Thom, N H, and S F Brown. 1988. “The Effect of Grading and Density on the Mechanical Properties of a Crushed Dolomitic Limestone.” In *Proceeding of the Australian Road Research Board*, 94–100.
Tutumluer, Erol, William Dombrow, and Hai Huang. 2008. “Laboratory Characterization of Coal Dust Fouled Ballast Behavior.” In *AREMA 2008 Annual Conference & Exposition*, edited by University of Illinois at Urbana Champaign, 1–31. Salt Lake City, UT: AREMA.
Tutumluer, Erol, Hai Huang, Youssef Hashash, and Jamshid Ghaboussi. 2006. “Aggregate Shape Effects on Ballast Tamping and Railroad Track Lateral Stability.” In *AREMA 2006 Annual Conference*, 1–23. Louisville, KY.
Uzarski, Don. 2009. “Introduction to Railroad Track Structural Design.” In *Railroad Track Design Including Asphalt Trackbeds Pre-Conference Workshop*, 1–42.
Webb, Geoff, David A Webb, Allan M Zarembski, James C Gauntt, and Deborah L Corallo. 2012. “Tie Guide”. Fayetteville, GA.
Wisconsin DNR. 2011. “Report to the Natural Resources Board : Silica Study”. Madison, WI.
Wisconsin DNR. 2012. “Silica Sand Mining in Wisconsin”. Madison, WI.
Wisconsin DOT. 2010. “Wisconsin Rail Plan 2030 - Draft Plan.”
Zarembski, A M. 1993. *Tracking Research and Development*. 1st ed. Omaha, NE: Simmons-Boardman Books, Inc.
Zarembski, A M. 2000a. “The Implications of Heavy Axle Load Operations for Track Maintenance on Short Lines”. Cherry Hill, NJ.
Zarembski, A M. 2000b. “Small Roads and Heavy Loads.” *Railway Age*, April.
Zarembski A M. 2001. “Challenge & Response.” *Railway Age*, December.
Zhang, X, and B A Baudet. 2013. “Particle Breakage in Gap-Graded Soil.” *Geotechnique* 3 (2): 72–77.

CFIRE

University of Wisconsin-Madison
Department of Civil and Environmental Engineering
1410 Engineering Drive, Room 270
Madison, WI 53706
Phone: 608-263-3175
Fax: 608-263-2512
cfire.wistrans.org